Search for Proton Decay via $p \to e^+\pi^0$ in a Large Water Cherenkov Detector

Masato Shiozawa

November 26, 1999

Doctor Thesis, University of Tokyo

Abstract

A search for proton decay via $p \to e^+\pi^0$ was carried out with the data taken by the Super–Kamiokande detector. The data used in this search corresponds to 535 days of data taking, or an exposure of 32.9 kton·year. No candidate event is found with an 0.1 expected background from atmospheric neutrino induced events. From this data, lower limit on the partial lifetime of the proton, $\tau/B_{p\to e^+\pi^0}$, is set to be 2.0×10^{33} years at a 90% confidence level.

Acknowledgment

I would like to express my great appreciation to my adviser, Professor Kenzo Nakamura for introducing me to Super–Kamiokande experiment. I acquired a great interest in the proton decays by his guidance. I would also thank him for supporting and guiding me throughout my graduate career.

Super–Kamiokande benefits from the excellent leadership of its spokesmen Yoji Totsuka, Yoichiro Suzuki, Henry Sobel, and James Stone. They gave me advice and encouraged me in many cases.

I wish to express my special gratitude to Takaaki Kajita who is a leader of the atmospheric neutrino and proton decay analysis group in Super–Kamiokande. His education, guidance, and comments made this thesis completed.

The analysis presented in this thesis depends on the hard works of many people in the analysis group, K. Kaneyuki, Y. Itow, M. Miura, T. Hayakawa, Y. Hayato, S. Kasuga, K. Fujita, K. Ishihara, K. Okumura, Y. Kanaya, K. Young, L. Wai, J. George, M. Etoh, J. Kameda, F. Tsushima and M. Messier. I recall hard but exciting days with them in the early period of Super–Kamiokande. I specially thank to B. Viren for his close work with me. Y. Watanabe, K. Nishikawa, C. K. Jung, E. Kearns, C. McGrew, K. Scholberg, C. W. Walter, and A. Habig were very helpful in many cases, especially in writing this thesis and the published paper.

Since I was graduate student, M. Nakahata has guided and helped me in many occasions. I learned many things related to physics and experiments from him. I would like to extend my gratitude to those that I have worked most closely at Kamioka Observatory, Y. Fukuda, K. Inoue, Y. Takeuchi, Y. Koshio, S. Moriyama, and K. Martens.

I never forget those who worked with me on the construction of the Super–Kamiokande data acquisition system, O. Sasaki, M. Nomachi, T. Tanimori, M. Mori, and T. Kumita. They taught me a lot of things about electronics, on-line system, and physics.

Finally I wish to express my deep gratitude to my parents and Hiroko Okazawa for their continuous support.

Contents

List of Figures

List of Tables

1 Introduction

In the standard model of elementary particles and their interactions, protons have finite but unobservably long lifetime [1]. This is a consequence of the baryon number (B) conservation law which is just empirically introduced into the standard model. However, it is interesting and suggestive that there is no known fundamental gauge symmetry which generates the baryon number conservation such like the case of the electrical charge conservation which is a consequence of $U(1)$ local gauge symmetry of Lagrangian. Therefore, the validity of baryon number conservation must be considered as an experimental question.

The expectation of the baryon number violation is partially supported by Sakharov's suggestion that the baryon number violation, C and CP violation, and thermal nonequilibrium state could produce matter-antimatter asymmetry in our universe [2]. Baryon number violated interactions could have generated the net baryon number in the first instant after the big bang.

In the standard model, three fundamental forces for electromagnetic, weak, and strong interactions are generated by corresponding local gauge symmetries. This model is represented by a product of the separated symmetry groups as $SU(3) \otimes SU(2) \otimes U(1)$. Since 1970's, Grand Unified Theories (GUTs), which unify the three fundamental interactions and describe them from larger gauge symmetries like $SU(5)$, have been extensively developed. Because leptons and quarks are often placed in same multiplets, most of GUTs allow baryon number violated interactions. Therefore, the decay of the proton is one of the most dramatic predictions of various GUT models [3, 4, 5, 6]. Because lifetime of proton largely depends on the mass scale of the super heavy particles mediating the proton decay, predicted proton lifetime has large uncertainty ranging from 10^{30} to over 10^{35} years.

In past two decades, several large mass underground experiments have looked for proton decays [7, 8, 9, 10, 11, 12]. Typical detector mass scale was 1 kton corresponding to $\sim 3\times10^{32}$ protons and they covered the minimal $SU(5)$ GUT prediction of $\sim 10^{30}$ years proton lifetime. However, no clear evidence has been reported and only lower limit of proton lifetime was obtained. For the decay mode of $p \to e^+\pi^0$, stringent limit has been set as 8.5×10^{32} years at 90% confidence level (CL) [7]. Currently, proton decays as a consequence of the minimal $SU(5)$ GUT model is considered to be ruled out. However, there are many GUT models which predict longer proton lifetime compatible with these experimental results.

Super–Kamiokande experiment, which utilizes large fiducial volume mass of 22.5 kton corresponding to 7.5×10^{33} protons, has started its operation on April first of 1996. Thanks to the huge volume, this detector has a capability to investigate proton decays with long lifetime above the current experimental limits. Moreover, the large photo coverage area enables us to perform the precise measurement of physical quantities of events. In general, GUTs predict many modes of proton decay. In many models, the $p \to e^+\pi^0$ mode is dominant and there are several GUTs which predict a decay rate within the observable range of Super–Kamiokande (see, for example [13, 14, 15]). This decay mode has a characteristic event signature, in which the electromagnetic shower caused by the positron is balanced against the two showers caused by the gamma rays from the decay of the π^0. This signature enables us to discriminate the signal events clearly from atmospheric neutrino background.

In this thesis, I describe the results of proton decay search using $p \to e^+\pi^0$ decay mode in 535 live-days, or 32.9 kton·year exposure of Super–Kamiokande data taken from May 1996 to April 1998. Beginning with physics backgrounds in section 2, the Super–Kamiokande detector and simulation of proton decay, background neutrino interactions, and the detector response are described in section 3 and 4. Event reduction and reconstruction algorithms are explained in section 5 and 6. Energy calibration of the detector is studied in section 7. Final sample after applying reduction programs is shown in section 8 and proton decay search is described in section 9. Finally, this thesis concludes in section 10.

2 Physics Background

In this section, physics background for the proton decay search is described. Beginning with the standard model which has been successfully supported by many experimental results, some of GUT models which unify elementary particles and their fundamental interactions are summarized. Interesting and dramatic prediction of the proton decay and its predicted lifetime are presented.

2.1 Standard Model

The base of the standard model is quantum field theory incorporated with local gauge symmetries. In the model, strong interactions are explained by quantum chromo dynamics (QCD) with $SU(3)_C$ gauge symmetry, and electromagnetic and weak interactions are unified by electro-weak theory described by $SU(2)_L \otimes U(1)_Y$ gauge symmetry. This model locates elementary particles in multiplets as following.

$$\begin{array}{lllll}
\text{leptons :} & \begin{pmatrix}\nu_e \\ e^-\end{pmatrix}_L & \begin{pmatrix}\nu_\mu \\ \mu^-\end{pmatrix}_L & \begin{pmatrix}\nu_\tau \\ \tau^-\end{pmatrix}_L & (1,\ \ 2,\ \ -1) \\
 & e^-_R & \mu^-_R & \tau^-_R & (1,\ \ 1,\ \ -2) \\
 & & & & \\
\text{quarks :} & \begin{pmatrix}u_i \\ d'_i\end{pmatrix}_L & \begin{pmatrix}c_i \\ s'_i\end{pmatrix}_L & \begin{pmatrix}t_i \\ b'_i\end{pmatrix}_L & (3,\ \ 2,\ \ \frac{1}{3}) \\
 & u_{iR} & c_{iR} & t_{iR} & (3,\ \ 1,\ \ \frac{4}{3}) \\
 & d_{iR} & s_{iR} & b_{iR} & (3,\ \ 1,\ \ -\frac{2}{3})
\end{array} \tag{2-1}$$

Here, $(d'_i, s'_i, b'_i)^T = V(d_i, s_i, b_i)^T$ where V is Cabibbo-Kobayashi-Maskawa mixing matrix. L and R denote left-handed and right-handed chirality, respectively. The entry $(N_{SU(3)}, N_{SU(2)}, Y)$ shows the representations under $SU(3)$ and $SU(2)$ symmetries and weak hypercharge. The suffix i denotes colour indices ($i = r, g, b$) of $SU(3)_C$ symmetry and all quarks compose colour triplets under the $SU(3)_C$. Left-handed fermions compose $SU(2)_L$ doublets and they have weak-isospin T_3 of $(1/2, -1/2)^{\mathrm{T}}$. All right-handed fermions are singlets under $SU(2)_L$. Each fermion has weak-hypercharge Y relating to $U(1)_Y$ gauge symmetry and the hypercharge is assigned as $Y = 2Q - 2T_3$ where Q is electrical charge of the fermion. As is shown in Equation (2-1), right-handed neutrinos are missed in the standard model and neutrino masses are assumed to be zero. Because leptons and quarks are located in separated multiplets in Equation (2-1), transitions between leptons and quarks are essentially not allowed.

By requiring gauge symmetries, gauge bosons which mediate interactions are generated. There are eight gauge bosons (gluons) which are generated by $SU(3)_C$ gauge symmetry. By $SU(2)_L$ and $U(1)_Y$, generated are three gauge bosons (W^1, W^2, W^3) and one boson (B), respectively. W^1 and W^2 are combined to form W^+ and W^- which mediate charged current weak interactions. W^3 and B are also combined by Weinberg angle θ_W and form Z^0 boson and photon A.

$$\begin{aligned}
Z^0 &= W^3 \cos\theta_W - B \sin\theta_W \\
A &= W^3 \sin\theta_W + B \cos\theta_W
\end{aligned} \tag{2-2}$$

Therefore, this model predicts neutral current weak interactions $\nu + X \rightarrow \nu + X'$ via Z^0 boson exchange. This interaction was experimentally confirmed by [16]. Photon A mediates electromagnetic interactions. θ_W is a free parameter in the standard model and there are relations:

$$e = g \sin\theta_W = g' \cos\theta_W \tag{2-3}$$

where g and g' are coupling constants relating to $SU(2)_L$ and $U(1)_Y$ gauge symmetries, respectively, and e is the electron charge.

Higgs field is introduced in the standard model so that $W^{\pm}$ and Z^0 bosons obtain nonzero masses by spontaneous symmetry breaking of $SU(2)_L \otimes U(1)_Y$. These boson masses are predicted as:

$$M_W = \frac{1}{2} v g \tag{2-4}$$

$$M_Z = \frac{1}{2} v \sqrt{g^2 + g'^2} \tag{2-5}$$

where v is the vacuum expectation of the Higgs field. Because there is relations of $1/2v^2 = g^2/8M_W^2 = G_F/\sqrt{2}$ where G_F is Fermi coupling constant ($G_F = 1.17 \times 10^{-5}$ GeV^{-2}), v is calculated as $v = 246$ GeV. Using $\sin^2\theta_W$ which can be obtained by measuring neutral current processes, this model numerically predicts the M_W and M_Z. The $W^{\pm}$ and Z^0 gauge bosons were discovered in 1983 [17] with consistent masses. Moreover, by the discovery of the top quark in 1994 [18], the confirmation of all fermions and gauge bosons in the standard model are completed. The Higgs boson is a remaining particle to be found.

In spite of the great success of the standard model, it is unlikely that the model is ultimate theory of elementary particle physics. One reason is that there are many free parameters which values cannot be predicted by the model itself. Another arbitrariness is there in the complicated assignment of the weak hypercharge Y to each fermion. There is no theoretical reason for assigning the hypercharge values shown in Equation (2-1). Because of the relation $Y = 2Q - 2T_3$, the assignment of the electrical charge is also arbitrary. Therefore, this model cannot explain the electrical charge quantization that the quark and lepton charges are related by factor of three. Moreover, there are three independent coupling constants relating to $SU(3)_C$, $SU(2)_L$, and $U(1)_Y$ and all of them are free parameters. This means that each kind of interactions relating to these symmetries are largely independent from each other. Also gravity is not included in the standard model.

2.2 Grand Unified Theories

The idea of GUT is that the strong, weak, and electromagnetic interactions are embedded in a larger underlying gauge theory with a single gauge coupling constant g [5]. The separated gauge symmetries and coupling constants in the standard model are considered to be the results of spontaneous symmetry breaking of GUT symmetry at M_X, the energy scale of GUT. In the high energy scale $Q^2 \gg M_X^2$, all fermions would be very much alike and all interactions are basically look similar. Fortunately, it is possible to estimate the M_X scale by known Q^2 dependence of three coupling constants in the standard model. They seem to meet at very high Q^2 and then one finds very large GUT scale of $M_X \gtrsim 10^{14}$ GeV. This very large energy scale is also needed to suppress proton decay rate so that predicted decay rate is consistent with experimental proton decay search results of $\tau_p > 10^{30}$ years.

2.2.1 $SU(5)$ GUT

In 1974, Georgei and Glashow proposed a simple GUT model based on SU(5) gauge symmetry [4]. SU(5) group is minimum simple group which have subgroups of SU(3), SU(2), and U(1). There are 24 generators in $SU(5)$ group and they are Hermitian and traceless. Fermions in each family are located in $\bar{5}$ and 10 representations of $SU(5)$.

$$\psi_{\bar{5}L} = \begin{pmatrix} d_1^c \\ d_2^c \\ d_3^c \\ e^- \\ -\nu_e \end{pmatrix}_L \tag{2-6}$$

$$\psi_{10L} = \frac{1}{\sqrt{2}} \begin{pmatrix} 0 & u_3^c & -u_2^c & -u^1 & -d^1 \\ -u_3^c & 0 & u_1^c & -u^2 & -d^2 \\ u_2^c & -u_1^c & 0 & -u^3 & -d^3 \\ u^1 & u^2 & u^3 & 0 & -e^+ \\ d^1 & d^2 & d^3 & e^+ & 0 \end{pmatrix}_L \tag{2-7}$$

And the gauge boson field which transforms under $SU(5)$ symmetry is:

$$V_\mu = \begin{pmatrix} G_1^1 - \frac{2B}{\sqrt{30}} & G_2^1 & G_3^1 & \overline{X^1} & \overline{Y^1} \\ G_1^2 & G_2^2 - \frac{2B}{\sqrt{30}} & G_3^2 & \overline{X^2} & \overline{Y^2} \\ G_1^3 & G_2^3 & G_3^3 - \frac{2B}{\sqrt{30}} & \overline{X^3} & \overline{Y^3} \\ X_1 & X_2 & X_3 & \frac{W^3}{\sqrt{2}} + \frac{3B}{\sqrt{30}} & W^+ \\ Y_1 & Y_2 & Y_3 & W^- & -\frac{W^3}{\sqrt{2}} + \frac{3B}{\sqrt{30}} \end{pmatrix} \tag{2-8}$$

The G_j^i is related to eight gluons and suffixes are $SU(3)_C$ coulor. $W^\pm$, W^3, and B are gauge bosons already appeared in the standard electroweak model (section 2.1). There are 12 new gauge bosons X and Y which don't appear in the standard model. They have electrical charge of 4/3 (X) and 1/3 (Y). These bosons have both colour and flavor and they mediate the transition between quarks and leptons.

In this model, electrical charge is quantized. This is because the electrical charge operator is a $SU(5)$ generator and hence $\mathrm{Tr}\hat{Q} = 0$ and the sum of electrical charges in each multiplet is 0. In the case of $\bar{5}$ representation, $Q_{d^c} + Q_{d^c} + Q_{d^c} + Q_{e^-} = 0$. Therefore, there is the relation between quark and lepton charges: $Q_{e^-} = -3Q_{d^c}$. The factor three is the number of colours.

The three coupling constants in the standard model are no longer independent from each other because $SU(3)_C \otimes SU(2)_L \otimes U(1)_Y$ gauge group is unified to single group $SU(5)$. For example, $SU(5)$ GUT predicts Weinberg angle θ_W from a direct asymptotic calculation as

$\sin^2\theta_W = 3/8$ at the unification point. For a comparison with experiments, this value must be converted to laboratory energies. However, this value is not so far from experimentally measured value and this rough agreement is encouraging.

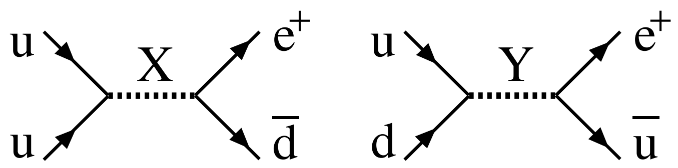

Figure 2–1: Examples for interactions via X and Y bosons exchange. B and L numbers are violated but $(B-L)$ is conserved.

Baryon (B) and lepton (L) number violated interactions are possible via X and Y bosons exchange. However, $(B-L)$ is conserved in the processes. Examples for interactions via X and Y bosons exchange are shown in Figure 2–1. Because proton decays are also mediated by the X and Y bosons, the decay rate is proportional to $1/M_X^4$. In the minimal $SU(5)$ model, the GUT mass scale is calculated to $M_X = 2.0^{+2.1}_{-1.0}\times 10^{14}$ GeV using the QCD scale parameter of $\Lambda_{\overline{\mathrm{MS}}} = 150^{+150}_{-75}$ MeV. Favored decay mode is $p\to e^+\pi^0$ and calculated partial lifetime is:

$$\tau_p/B_{p\to e^+\pi^0} = 3.7\times 10^{29\pm0.7} \text{ years [19].} \tag{2-9}$$

However, this prediction is inconsistent with experimental search results of $\tau_p/B_{p\to e^+\pi^0} > 8.5\times 10^{32}$ years [7] and $> 2.6\times 10^{32}$ years [10]. Therefore, proton decays as a consequence of the minimal $SU(5)$ GUT model is considered to be ruled out.

There is another difficulty in the minimal $SU(5)$ GUT. Precise measurements of $\sin^2\theta_W$ by LEP and other accelerator experiments obtained the value of $\sin^2\hat{\theta}_W(M_Z) = 0.2315\pm 0.0004$ [20] while predicted value is $\sin^2\hat{\theta}_W(M_Z) = 0.2102^{+0.0037}_{-0.0031}$ [21]. Moreover, LEP precise measurement showed that three coupling constants don't get together at high energy region [21, 22] as is shown in Figure 2–2–(a).

In spite of several attractive features of the minimal $SU(5)$ GUT, it need extensions to solve these inconsistency.

2.2.2 Extensions of $SU(5)$ GUT

SO(10) GUT

One possible way to extend the $SU(5)$ GUT model is to use larger symmetries. The $SO(10)$ symmetry is one of famous candidates. There are several advantages of GUT models based on $SO(10)$ symmetry.

The $SO(10)$ GUT model which directly breaks to $SU(3)_C\otimes SU(2)_L\otimes U(1)_Y$ predicts relatively short lifetime of protons and the prediction is not consistent with experimental

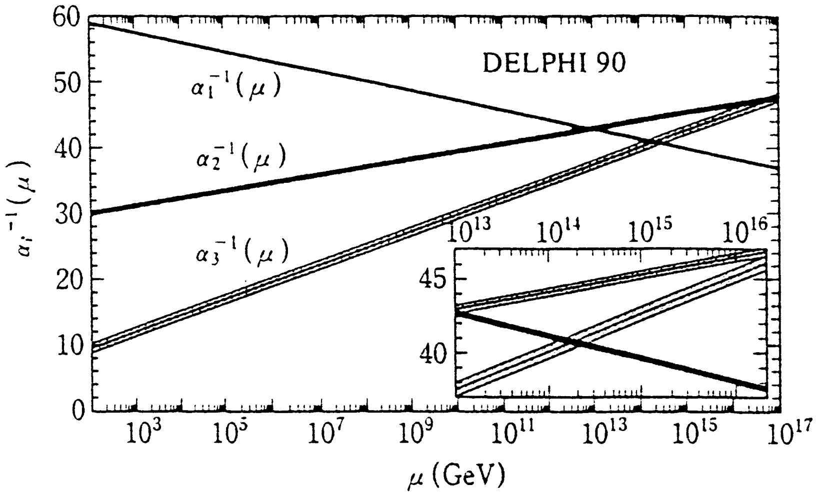

(a)

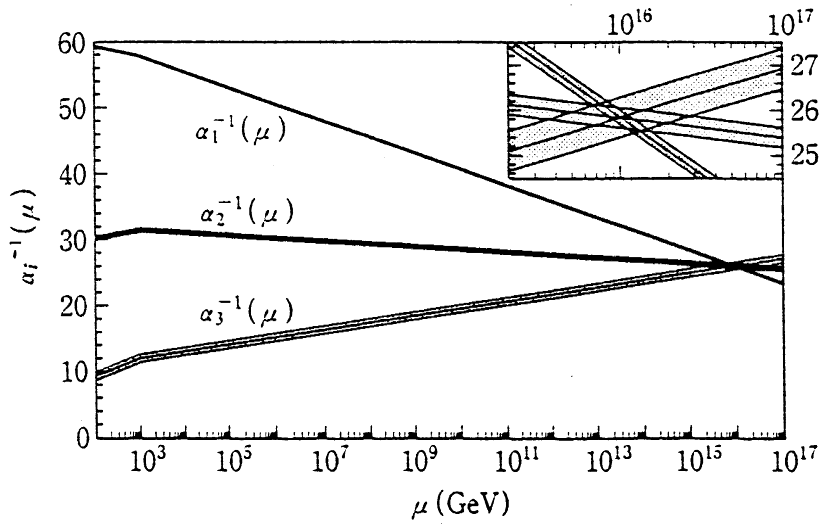

(b)

Figure 2–2: Running coupling constants based on (a) minimal standard model and (b) minimal SUSY model [22]. In the case of (a), grand unification doesn't happen at high energy scale. For the minimal SUSY model, three coupling constants meet together at high energy scale. The SUSY energy scale is fitted by requiring crossing of these coupling constants at a single point.

results [23]. On the other hand, there are several ways for $SO(10)$ symmetry to beak down to $SU(3)_C \otimes SU(2)_L \otimes U(1)_Y$ by two steps [24].

$$SO(10) \longrightarrow \left\{ \begin{array}{l} SU(5) \otimes U(1), \\ SU(4) \otimes SU(2)_L \otimes SU(2)_R, \\ SU(3) \otimes SU(2)_L \otimes SU(2)_R \otimes U(1), \\ SU(3) \otimes SU(2)_L \otimes U(1) \otimes U(1) \end{array} \right\} \longrightarrow SU(3)_C \otimes SU(2)_L \otimes U(1)_Y \tag{2-10}$$

One of advantages of $SO(10)$ GUT models is that it can contain the left-right symmetry which is missed in the standard electroweak model. Second advantage is that $SO(10)$ model has representations of 16 in which there is a room for right handed neutrinos missed in the $SU(5)$ model. $SO(10)$ model that implements the seesaw mechanism [25] may explain the neutrino masses and mixing. Moreover, the fermion unification into a single representation of 16 is a attractive feature of the model.

$SO(10)$ models predict $\sin^2\theta_W$ consistent with experimental results and the running coupling constants can meet at a single unification point [14, 15]. Among several intermediate symmetries, $SU(4) \otimes SU(2)_L \otimes SU(2)_R$ is very interesting because it contains the left-right symmetry and predicts the observable partial lifetime of protons:

$$\tau_p / B_{p \to e^+\pi^0} = 1.44 \times 10^{32.1 \pm 0.7 \pm 1.0 \pm 1.9} \text{ years [15, 26].} \tag{2-11}$$

However, other intermediate symmetries are also allowed and predicted partial lifetime of protons has large uncertainties ranging from $\sim 10^{32}$ to $\sim 10^{39}$ years [14, 15].

Supersymmetric GUT

Particles		Spin	SUSY Partners		Spin
q_L	quark	1/2	$\tilde{q}_L$	squark	0
q_R	quark	1/2	$\tilde{q}_R$	squark	0
l_L	lepton	1/2	$\tilde{l}_L$	slepton	0
l_R	lepton	1/2	$\tilde{l}_R$	slepton	0
H_1, H_2	higgs	0	$\tilde{H}_1, \tilde{H}_2$	higgsinos	1/2
g	gluon	1	$\tilde{g}$	gluino	1/2
γ	photon	1	$\tilde{\gamma}$	photino	1/2
Z^0	Z boson	1	$\tilde{Z}^0$	zino	1/2
$W^\pm$	W boson	1	$\tilde{W}^\pm$	wino	1/2

Table 2–1: The particles and SUSY partners.

Implementing Supersymmetry (SUSY) [27] is another approach to make models consistent with experimental measurements. SUSY is a symmetry between fermions and bosons and this requires that each fermion should have a boson partner with same mass and vise versa. The particles and SUSY partners are listed in Table 2–1. Because there is no observation of SUSY particles, SUSY should be broken at low energy. The breaking energy scale is expected to be ~ 1 TeV.

For the minimal SUSY $SU(5)$ GUT, it was shown that three coupling constants meet together at high energy scale as is shown in Figure 2–2-(b). The unification scale is around 2×10^{16} GeV which is higher than the prediction of non-SUSY $SU(5)$ (section 2.2.1). The predicted Weinberg angle is $\sin^2 \hat{\theta}_W(M_Z) = 0.2334^{+0.0031}_{-0.0027}$ which is consistent with experimental data [21]. Due to the higher unification scale, predicted partial lifetime of protons via $p \to e^+\pi^0$ mode becomes long as $\sim 10^{34-38}$ years [28, 29, 30] and theoretical lower limit is calculated as:

$$\tau_p/B_{p\to e^+\pi^0} > 4.1 \times 10^{33} \text{ years [28].} \tag{2-12}$$

This lifetime prediction cannot be reached by this thesis. However, there are other SUSY $SU(5)$ models which predict observable partial lifetime of $p \to e^+\pi^0$ mode (see, for example [13]). On the other hand, minimal SUSY GUT favors the decay mode of $p \to \bar{\nu}K^+$. The predicted partial lifetime has a large uncertainty and varies from the order of 10^{29} to 10^{33} years within the observable range of Super–Kamiokande. Therefore, minimal SUSY $SU(5)$ model can be tested by searching for the proton decay via $p \to \bar{\nu}K^+$ [31].

3 Detector

3.1 Cherenkov light

In the Super–Kamiokande experiment, events are observed by detecting Cherenkov photons which are emitted by charged particles traversing in the detector water. The Cherenkov light, originally discovered by Cherenkov in 1934, was explained theoretically and quantitatively by Tamm and Frank [32]. The Cherenkov light is electromagnetic wave which is emitted along a charged particle traversing in a medium with a velocity faster than the light velocity in the medium as:

$$v \geq \frac{c}{n} \tag{3-1}$$

where v is a velocity of the charged particle, n is a refractive index of the medium and c is the light velocity in vacuum. The light is emitted in the forward direction of the traveling particle with an opening angle θ as:

$$\cos\theta = \frac{1}{n\beta} \tag{3-2}$$

where β is v/c. The light trajectories form cone plane as shown in Figure 3–1. The light spectrum are known to have wavelength dependence and the number of the emitted photons dN in unit wavelength $d\lambda$ and in unit track dx is:

$$\frac{d^2N}{dxd\lambda} = 2\pi\alpha(1 - \frac{1}{(n\beta)^2})\frac{1}{\lambda^2} \tag{3-3}$$

where α is the fine structure constant. For example, if a charged particle is traveling in water ($n \simeq 1.34$) with the light velocity ($\beta \simeq 1$), Cherenkov photons are emitted along the particle with opening angle $\theta \simeq 42°$ and the number of the photons is roughly 340 cm^{-1} for the wavelength of 300 nm to 600 nm. The light cone makes circular projective pattern on a surface plane in the detector. An example of a simulated event pattern which should be detected in Super–Kamiokande is shown in Figure 3–2. The ring image produced by 500 MeV/c muon is clearly seen in the figure.

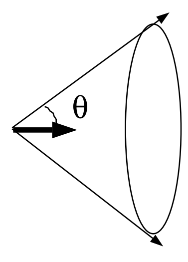

Figure 3–1: Cherenkov photons (thin arrows) are emitted along the charged particle (thick arrow) with an opening angle of $\theta = \cos^{-1}(1/n\beta)$ in water.

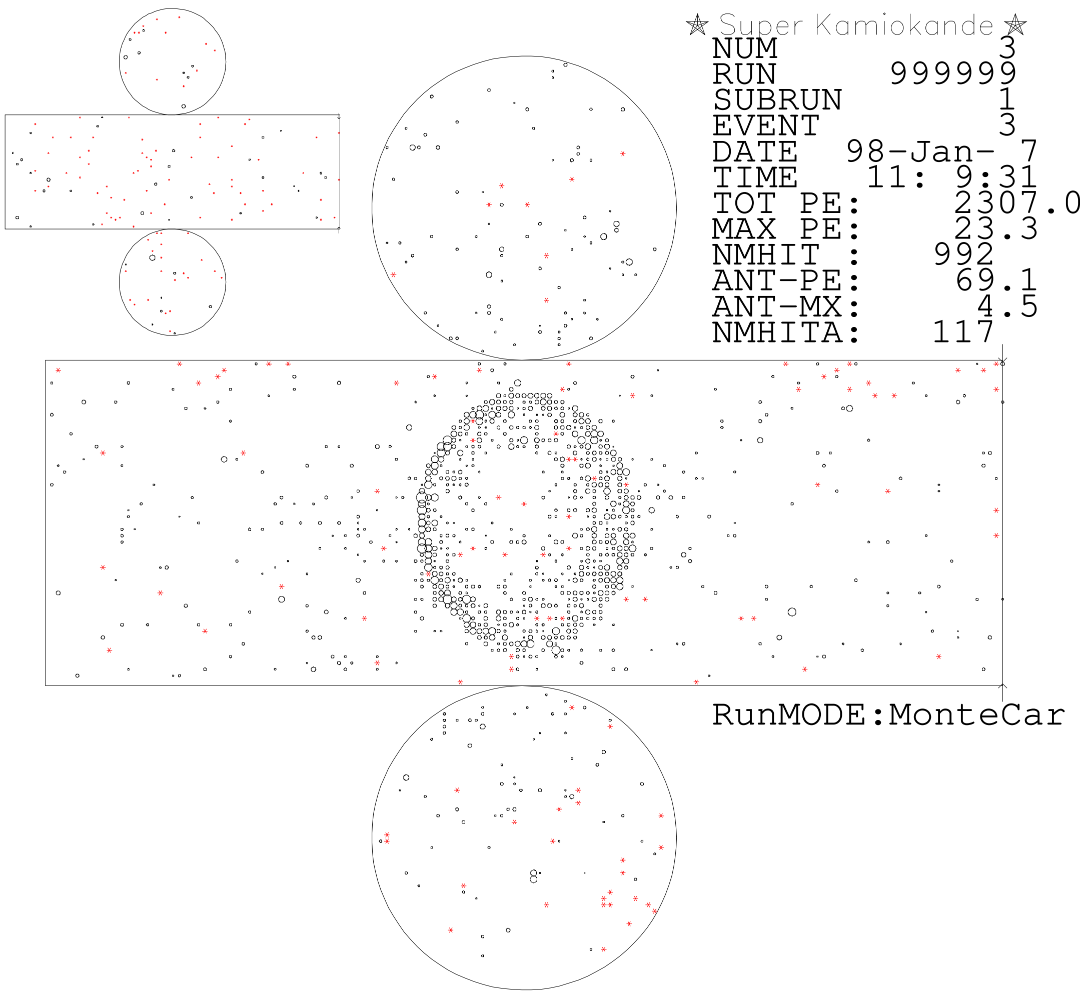

Figure 3–2: event display of a simulated 500 MeV/c muon. Small circles show each photomultiplier which detect photon(s). The projective ring image is seen on photomultiplier plane.

3.2 Super–Kamiokande detector

Super–Kamiokande is a large underground water Cherenkov detector which is located in the Mozumi zinc mine at 2700 meters-water-equivalent below the peak of Mt. Ikenoyama in Kamioka, Gifu prefecture, Japan. The experiment site is accessible by a 2 km drive from Atotsu entrance. Schematic view of the experiment site and the detector is shown in Figure 3–3. The detector holds 50 ktons of ultra-pure water contained in a cylindrical stainless steel tank measuring 41.4 m in height and 39.3 m in diameter. The water is optically separated into three concentric cylindrical regions.

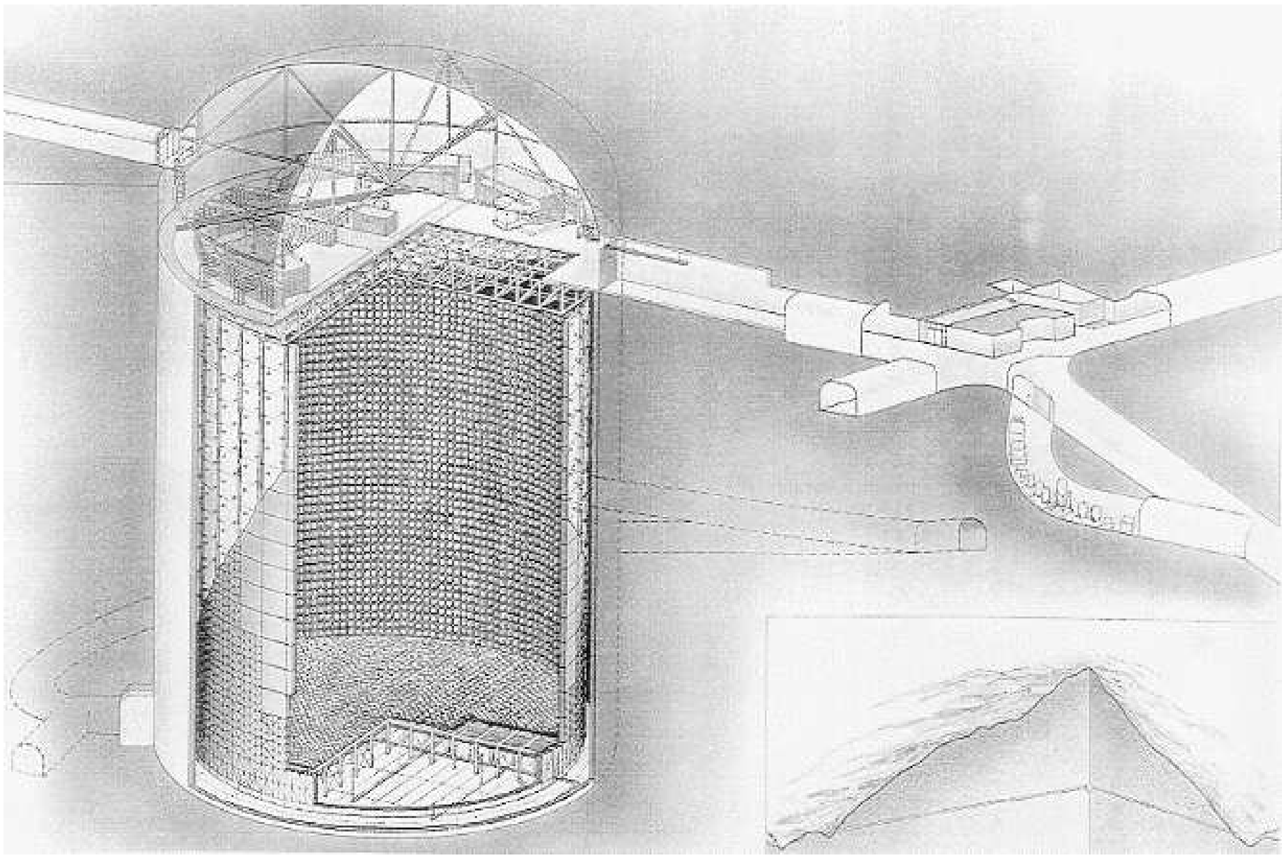

Figure 3–3: Super-Kamiokande detector and experiment site.

The inner region is 36.2 m in height and 33.8 m in diameter and is viewed by 11146, inward facing, 50 cm diameter photomultiplier tubes (PMTs). These PMTs uniformly surround the region giving a photocathode coverage of 40%. They were specially developed to have good single photoelectron (p.e.) response and a time resolution of 2.8 ns RMS for 1 p.e. equivalent signals [33]. The PMT signals are digitized asynchronously by a custom built data acquisition system [34, 35] which can process two successive signals, enabling us to detect the electron from the decay of a muon.

The outer region completely surrounds the inner detector. It is 1.95 $\sim$ 2.2 m thick, and is viewed by 1885 outward pointing 20 cm diameter PMTs with 60 cm square wavelength shifter plates [36]. The walls of the outer detector are lined with DuPont Tyvek, a white reflective material to increase the number of Cherenkov photons detected. The primary function of the outer detector is to veto cosmic ray muons and to help identify contained events.

The middle region (dead space) is an uninstrumented, 0.55 m thick cylindrical shell between the inner and outer detectors. It is occupied by the stainless steel support structure as well as water. The border with the inner detector is lined with opaque black plastic and the border with the outer detector, by opaque black low density polyethylene bonded to the reflective Tyvec. Along with the outer detector the dead space acts as a shield against radioactivity from the surrounding rock.

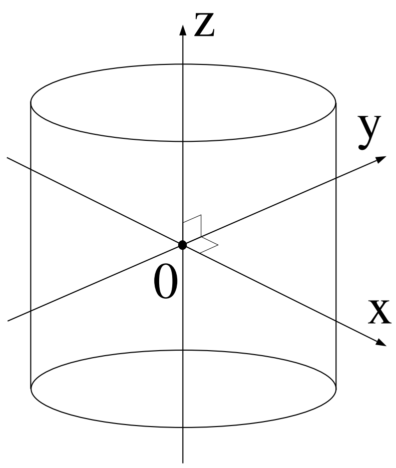

Figure 3–4: The detector coordinate.

The detector coordinate is defined as Figure 3–4. A vertical axis is a z-axis and horizontal axes are x- and y-axes. At center position of the detector, $(x, y, z) = (0, 0, 0)$.

3.2.1 Photomultiplier

We use 50 cm (20 inch) diameter PMTs which was originally developed by HAMAMATSU Photonics Company and Kamiokande collaborators for Kamiokande experiment. The large photocathode area is essential to have large photocoverage area in reasonable cost. A schematic view of the PMT is shown in Figure 3–5 and its characteristics are summarized in Table 3–1.

The photocathode area is coated by Bialkali material. The quantum efficiency as a function of the light wavelength is shown in Figure 3–6. The efficiency has a peak around 400 nm which matches the wavelength dependence of the light attenuation length in water

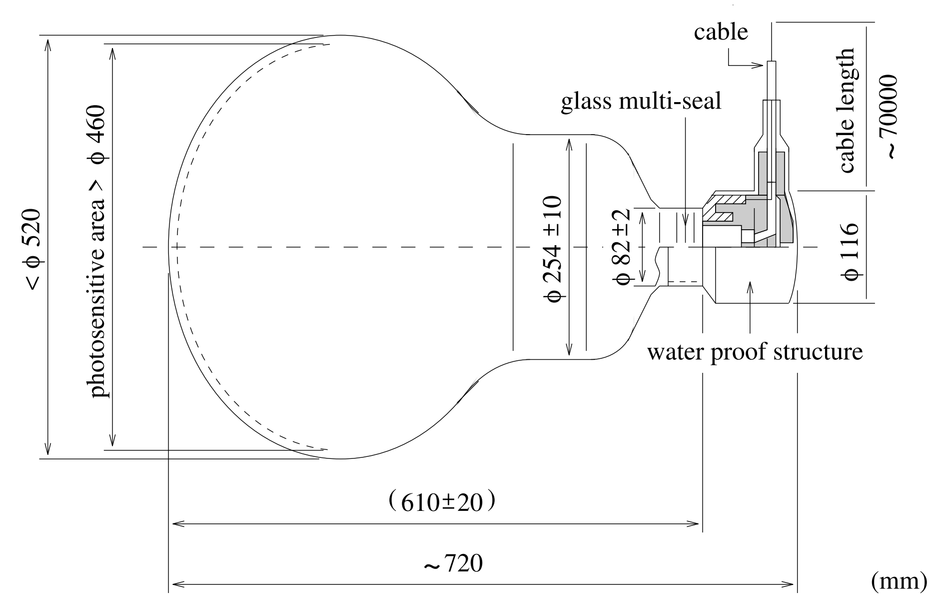

Figure 3–5: A schematic view of the 20 inch PMT.

Photocathode area	50 cm (20 inch) in diameter
Shape	Hemispherical
Window material	Pyrex glass ($4 \sim 5mm$)
Photocathode material	Bialkali
Dinodes	Venetian blind type, 11 stages
Pressure tolerance	6 kg/cm^2 water proof
Quantum efficiency	20% at $\lambda = 400$ nm
Gain	10^7 at $\sim$ 2000 Volt
Dark current	200 nA at gain= 10^7
Dark pulse rate	$\sim$ 3 kHz at gain= 10^7
Cathode non-uniformity	$< 10\%$
Anode non-uniformity	$< 40\%$
Transit time	90 nsec typical at gain= 10^7
Transit time spread	2.8 nsec RMS at 1 p.e. equivalent signals

Table 3–1: The characteristics of the 20 inch PMT.

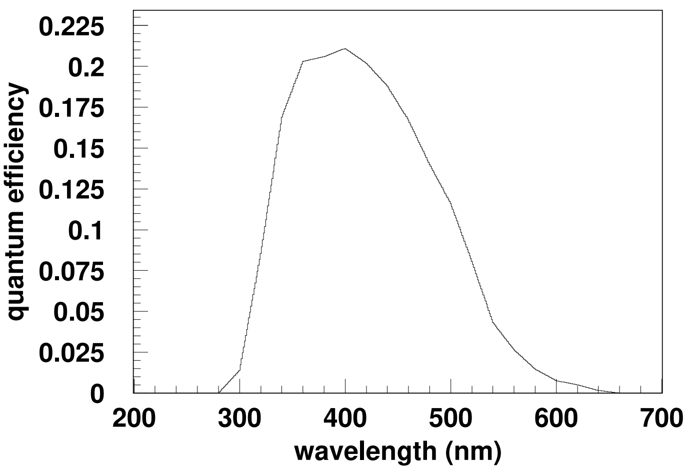

Figure 3–6: The quantum efficiency of the 20 inch PMT as a function of wavelength.

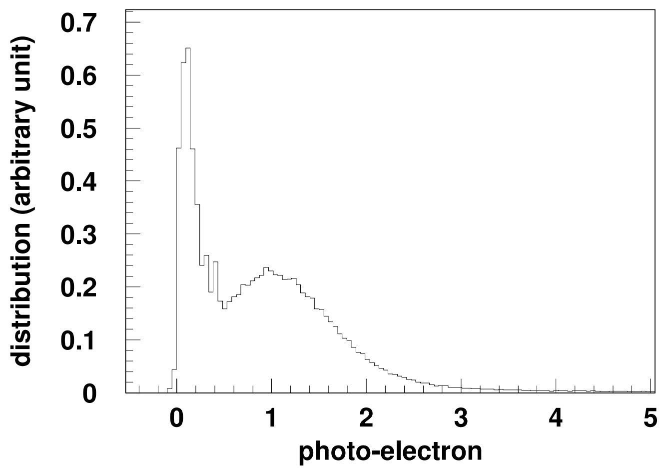

Figure 3–7: The one photo-electron distribution of the 20 inch PMT.

(see Figure 4–23). Due to the large photocathode area, the dinode is of Venetian blind type. For Super–Kamiokande experiment, optimization of the dinode structure were performed. The number of dinode planes, 11 stages for which the ratio of applied voltage is 8 : 3: 1: ... : 1, is selected to obtain the good timing response and collection efficiency. Figure 3–7 shows the measured 1 p.e. distribution. A clear peak of 1 p.e. is seen in the figure. The lower tail is due to the photoelectrons which don't hit and pass through the first dinode plane. The water proof structure is also improved from the old Kamiokande type. We need to keep the geo-magnetic field less than 100 mG to obtain the uniform response of the PMT. Compensation coils are used in the Super–Kamiokande detector and the residual is kept less than 100 mG in every position of the detector.

3.2.2 Water Purification System

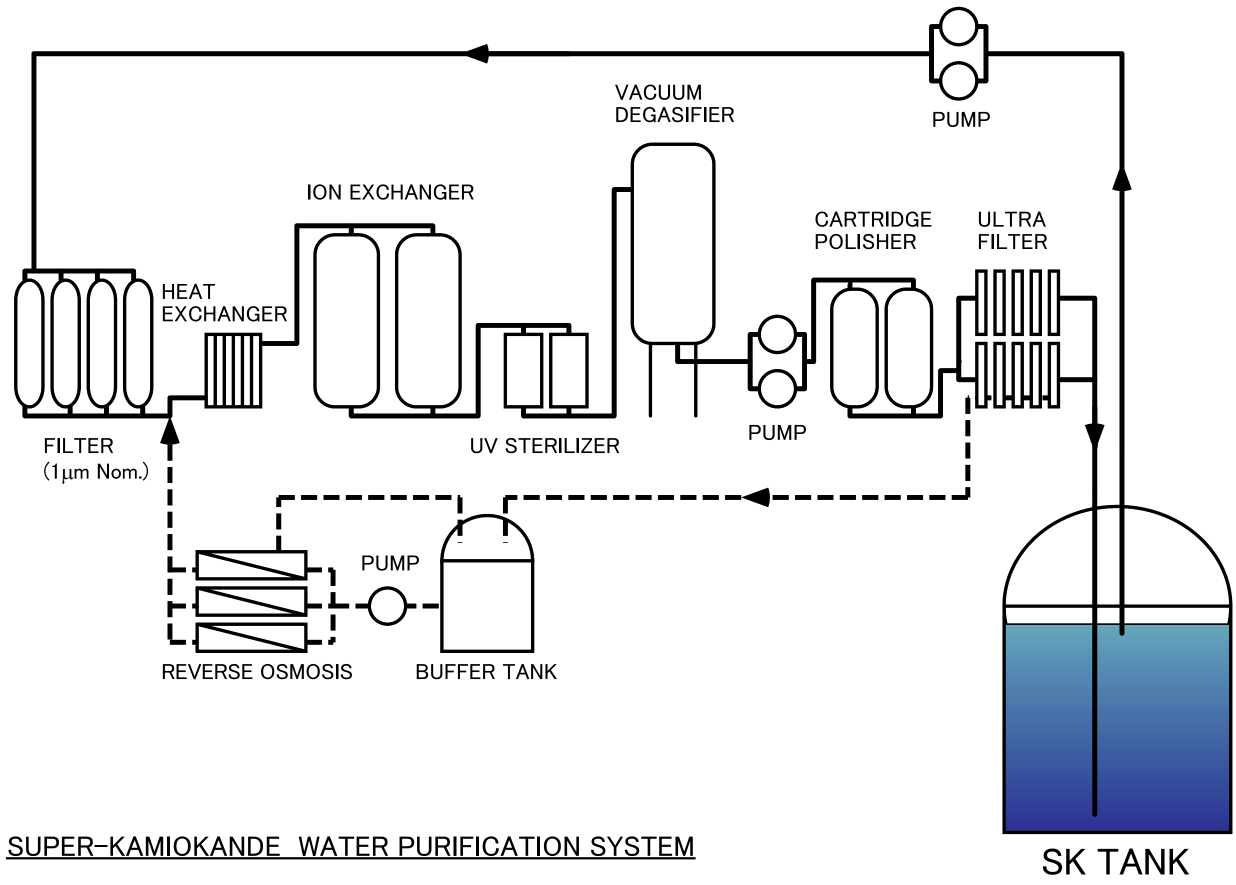

Figure 3–8: The water purification system for the Super–Kamiokande detector.

The source of the water filled in the Super–Kamiokande detector is the clean spring water flowing in the mine. The detector is implemented the water purification system and the water system makes ultra-pure water from the source water. Usually, the water system supplies the ultra-pure water from the bottom of the tank and takes it from the top of the tank. The system comprises several components as is shown in Figure 3–8.

- 1 μm filter — rejects small particles.
- Heat exchanger — heat exchanger is used to keep the water temperature which is heated by PMTs and pumps. The water temperature is kept at around 14°C.
- Ion exchanger — removes metal ions.
- Ultra-Violet sterilizer — kills bacteria in the water.
- Vacuum degasifier — removes gases such as the oxygen and radon gases.
- cartridge polisher — high performance ion exchanger.
- Ultra filter — removes small dust even of the order of 10 nm.
- Reverse osmosis — The unfiltered water by the ultra filter is fed to the reverse osmosis with the buffer tank. The reverse osmosis is the high performance membrane which removes even organisms of the order of 100 molecular weight. The output water is put back to the main stream (Figure 3–8).

The ultra-pure water is usually circulated via the detector and water system at the flow rate of 50 $\sim$ 60 ton/hour.

3.2.3 Data Acquisition System

Inner Detector

The PMT signals are processed by TKO [37] ADC/TDC modules called Analog-Timing-Module (ATM) [34]. The ATM has the functionality of ADC/TDC and records an amount of charge and timing of each PMT signal. Figure 3–9 shows the schematic view of the analog input block of the ATM. The PMT signal fed to the current splitter is divided into four signals. One of them is fed to the discriminator and the threshold level for each channel is set to be -1 mV which corresponds to 1/4 p.e.. When PMT signal is over the threshold level, HITSUM signal with 200 ns width and 15 mV/channel height is asserted on the ATM front panel to be used to generate the global trigger signal. At the same time, one of the splitted signal A and B is hold by the QAC (Charge to Analog Converter) [35] and TAC (Timing to Analog Converter) [35] starts to integrate constant current. If global trigger is issued, the information in TAC/QAC is digitized and stored in internal memories. Since the integration of TAC is started by the PMT signal of each channel, the amount of the charge integrated by the TAC is relevant to the hit timing of the signal. There are two TAC's and QAC's for

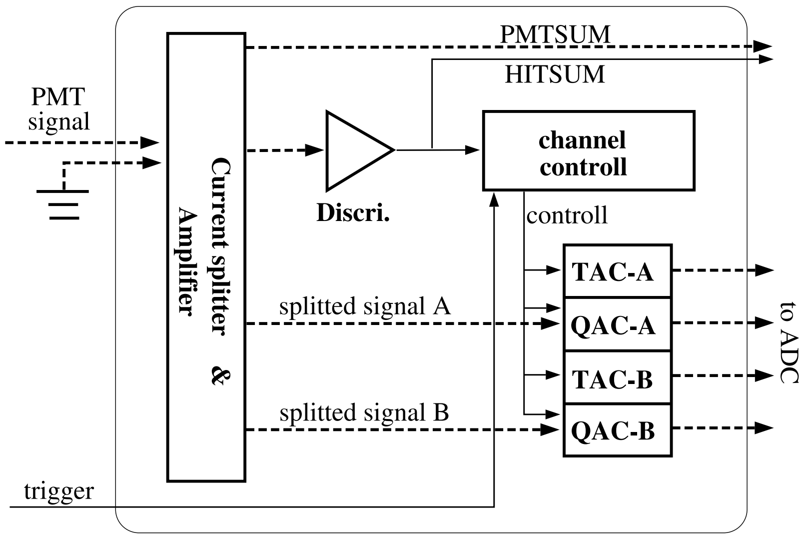

Figure 3–9: A schematic view of the analog input block of the ATM. Only one channel is shown in the figure. Dashed arrows show the PMT signal, its splitted signals and accumulated TAC/QAC signals. Solid arrows show the logical signals which control the processing of the analog signals.

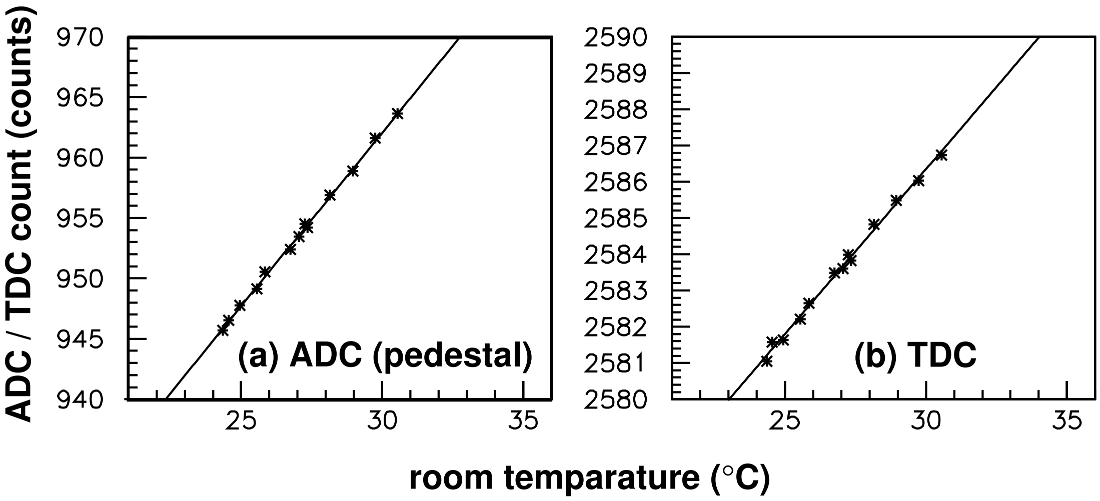

Figure 3–10: The room temperature dependence of the ADC and TDC pedestal. Both ADC and TDC have linear dependence on the room temperature. The pedestal data are regularly taken in Super–Kamiokande every 30 minutes and used in the ADC/TDC conversion.

each channel so that two successive event, like a muon and a following decay electron, can be processed.

The ADC/TDC data are of 12 bits (4096). The ATM has $\sim$ 450 pC dynamic range with a resolution of 0.2 pC and $\sim$ 1300 nsec dynamic range with a resolution of 0.4 ns. To keep good accuracies of the timing and charge information, we use conversion tables rather than the fitted linear functions to convert ADC and TDC counts to [pC] and [nsec], respectively. The inaccuracies in the conversion by the tables is negligible.

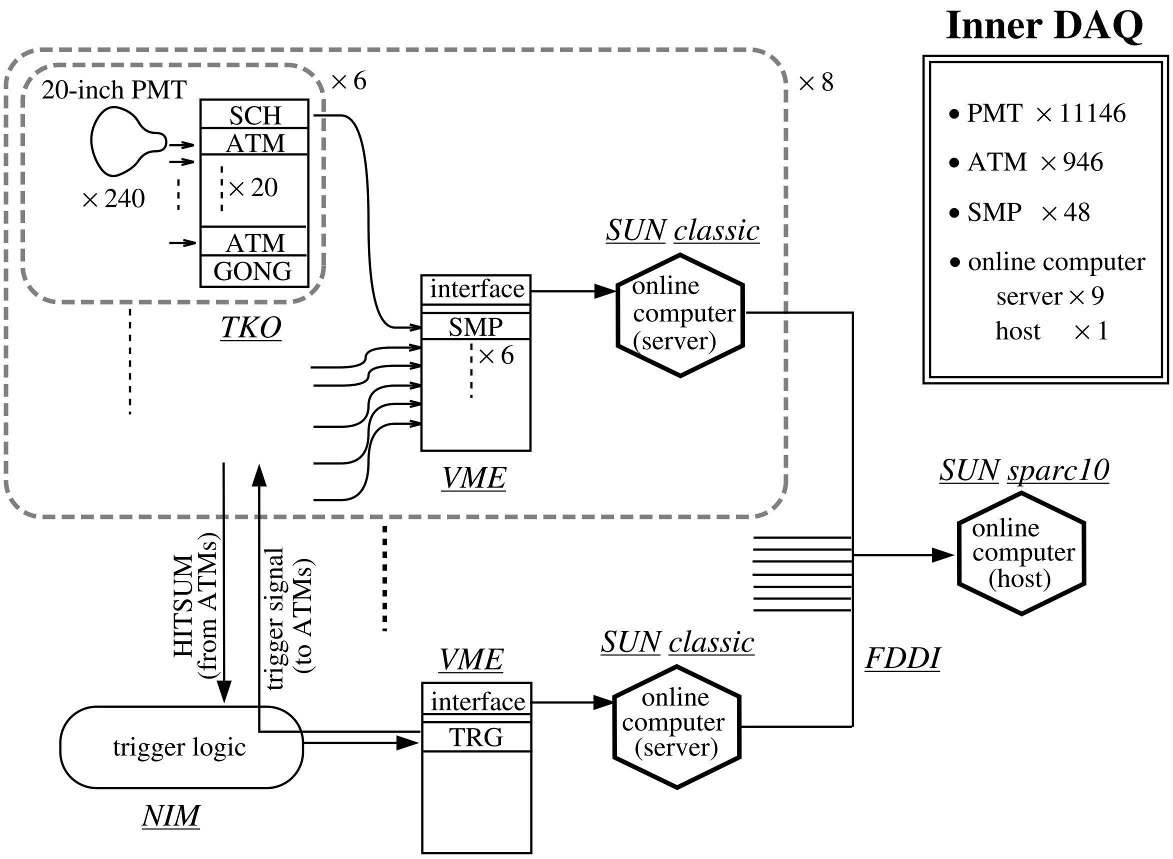

Figure 3–11: The data acquisition system for the inner detector. Arrows show the flow of the inner detector data.

The room temperature dependence of ADC and TDC is less than 3 count/°C (0.6 pC/°C) and 2 count/°C (0.8 ns/°C), respectively. Figure 3–10 shows an example of the room temperature dependence of the ATM. These pedestal values of ADC and TDC have a linear dependence on the room temperature. In order to correct for the temperature dependence of ADC and TDC, the pedestal data are regularly taken every 30 minutes in Super–Kamiokande and the measured pedestal values are used to convert ADC and TDC counts in each period. The room temperature is around 27 °C and is kept within ±0.5°C in the electronics huts. The estimated inaccuracies coming from the temperature dependence is less than 0.3 pC and 0.4 ns for the charge and timing information.

Figure 3–11 shows the inner data acquisition system. There are in total 946 ATMs, and ADC/TDC data are read separately by 8 on-line computers (SUN Classic) through 48 VME memory modules called Super-Memory-Partner (SMP). The trigger data, which consist of the event number, trigger timing, and trigger type and are recorded in the trigger module called TRG, are also read by another server computer. These data collected by the server computers are transferred to the on-line host computer (SUN sparc10) via the FDDI network and merged to make complete events.

Outer Detector

Outer detector data are processed by a different electronics system. The signal of 8 inch PMT is fed into QTC (Charge to Timing Converter) module which generates a rectangle signal. This output signal has a width proportional to an amount of charge of the PMT signal and is digitized by the LeCroy 1877 multi-hit TDC module. This TDC module records the timing of the leading and trailing edge from which we know the timing and charge information of the PMT signal. The dynamic range of the TDC is set to be 16 μsec with the resolution of 0.5 nsec. The TDC data are read via VME memory modules by a separate on-line server computer and then transfered to the on-line host computer.

Trigger

The rectangle HITSUM signals from ATMs are summed up to generate grand HITSUM signal. The HITSUM signals from QTCs are also summed up separately to make grand HITSUM of the outer detector. These two grand HITSUM signals are used to generate trigger signals for the Super–Kamiokande detector. There are two kinds of trigger signal made by the inner detector. One is low energy trigger (LE trigger) which is generated by requiring -320 mV grand HITSUM signals and another is high energy trigger (HE trigger) which threshold level is -340 mV. The LE trigger corresponds to 29 hits of inner PMTs which is equivalent to Cherenkov photons generated by 5.7 MeV electron. The trigger efficiency for $p \to e^+\pi^0$ signal is 100 %. There is also outer detector trigger (OD trigger) generated by the outer detector HITSUM signal. The threshold for the OD trigger corresponds to 19 hits of outer PMTs.

These three types of trigger signal, LE trigger, HE trigger, and OD trigger, are fed into TRG module as is shown in Figure 3–11. Once at least one of the trigger signals is asserted, this TRG module records the trigger types (LE/HE/OD), the trigger timing with 20 nsec accuracy, and the event number. Moreover, TRG generates the global trigger signal and 16 bits event number on its front panel which are distributed to whole electronics to trigger the current event. The trigger data stored in the TRG module are read by a separate on-line computer and sent to the on-line host computer to be merged with PMT data.

3.3 Detector Calibration

The methods of several detector calibration such as the PMT timing calibration, PMT gain calibration, and water transparency measurements are described in this section.

3.3.1 Timing Calibration

By the timing calibration of each channel, we need to measure following quantities for each channel:

- time offset   coming from the transit time of the PMT itself and its cable ($\sim$ 70 m).
- time walk   The timing information depends on the signal height or detected p.e.s.

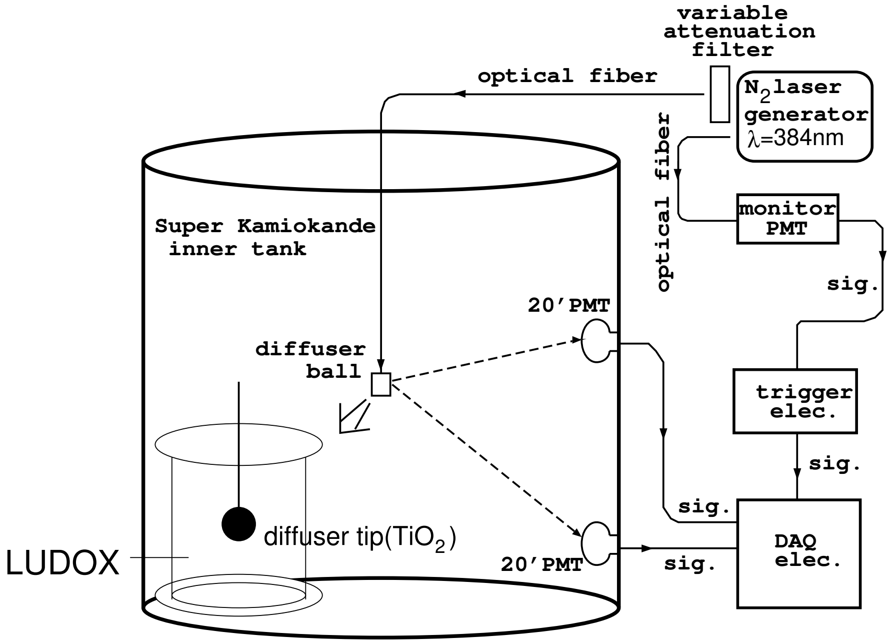

Figure 3–12: The timing calibration system.

For the timing calibration, we put a light source of the diffuser ball into the water tank and make the source flash. Figure 3–12 shows the schematic view of the timing calibration system. We use a nitrogen laser and variable attenuation filter. The light is guided by an optical fiber to the diffuser ball in the detector. The width of the laser light is small ($\sim$ 3 nsec) and the time jitter is small enough ($\sim \pm 0.5$ nsec). By the attenuation filter, we can take timing data at various light intensities. The diffuser ball contains a TiO_2 tip and LUDOX which is silica gel with 20 nm glass fragments. The reflective tip is located at the center of the ball and reflected light is diffused by LUDOX. Figure 3–13 shows the distribution of the measured timing and detected p.e.s of one 20 inch PMT. Points are data. Blank circles show the averaged timing for each p.e. bin. The time walk is observed in the figure. This charge dependence of the timing is called TQ-map and we make the TQ-map for each channel. In physics analyses, the timing information of each channel is corrected by its TQ-map. Error bars in the figure show the timing resolution. Figure 3–14 shows

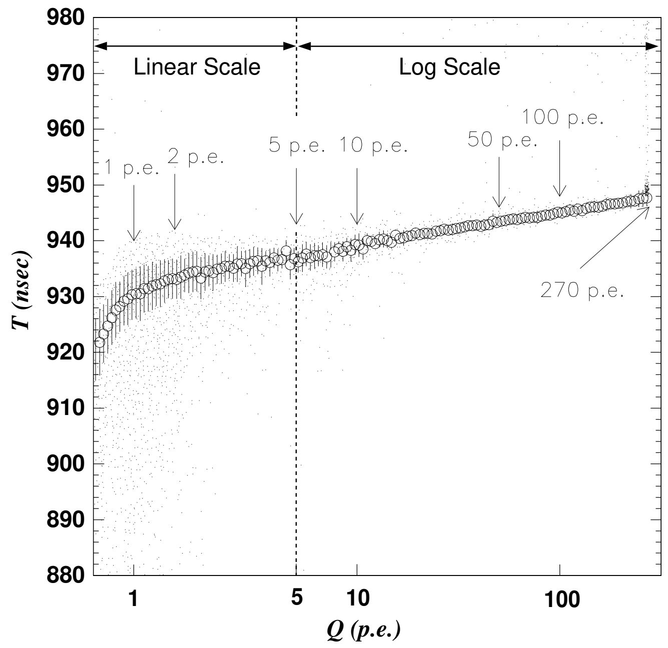

Figure 3–13: TQ-map, the timing distribution as a function of detected photo-electrons.

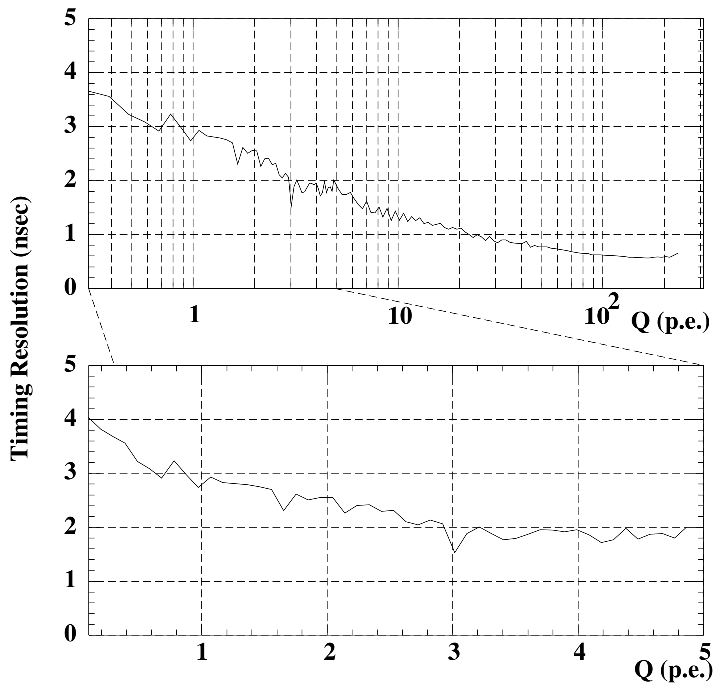

Figure 3–14: The timing resolution of the 20 inch PMT.

the measured timing resolution. The timing resolution is typically 2.8 nsec RMS for 1 p.e. equivalent signals.

3.3.2 Relative Gain Calibration

We need to adjust the PMT gain to obtain the uniform response of the detector. Before Super–Kamiokande started its operation, we performed the gain calibration with a light source in order to determine the applied high voltage value of each 20 inch PMT. The observed p.e.s in the PMTs are compared with those of neighboring PMTs and the applied high voltage values are adjusted. After the start of the experiment, we regularly took calibration data. Fine tuning of the PMT gain is performed in software analyses using the calibration data.

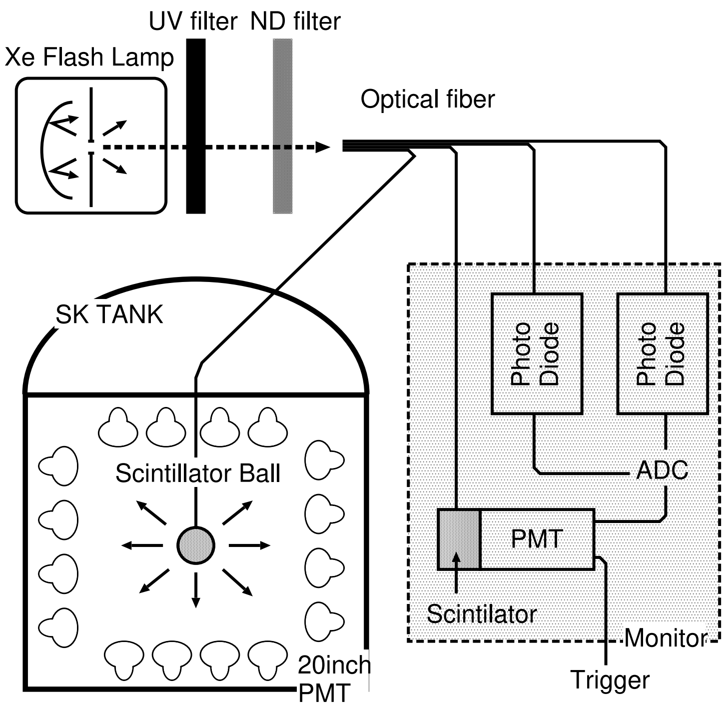

Figure 3–15: Xe calibration system.

Figure 3–15 shows the calibration system. We use a Xe lamp as a light source. The light from the lamp passes through a UV-pass filter to adjust the wavelength for which the scintillator ball can absorb. A ND filter is also used to adjust the light intensity. The output light is guided by the optical fiber to the scintillator ball in the detector. The scintillator ball is a spherical acrylic ball doped with a BBOT wavelength shifter and MgO diffuser. BBOT absorbs the Xe light and re-emits light around 450 nm wavelength, which spectrum is similar to that of Cherenkov light. The intensity of the Xe light is monitored by two photo diodes and one scintillator equipped with a PMT.

Before Super–Kamiokande started its operation, we took the 20 inch PMT data putting the scintillator ball in the tank without water. The observed number of p.e.s by the 20 inch PMTs are corrected for the distance, PMT acceptance, and Xe light intensity measured by the monitoring system. By comparing the corrected p.e.s in PMTs with those of neighboring PMTs, we determined the high voltage value for each PMT.

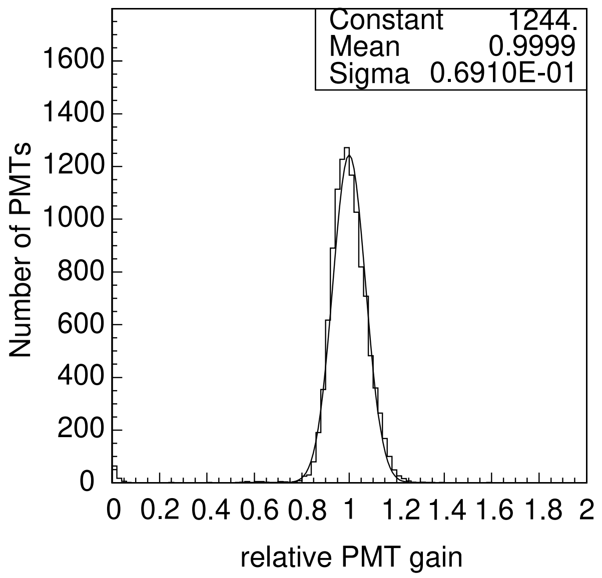

Figure 3–16: The relative gain difference observed in the Xe calibration. After the experiment started, we regularly took Xe data. Corrected number of p.e.s in each PMT, normalized to the mean value, is compared with each other. The PMT gain difference is 7%.

After the detector was filled up with water, we regularly take the Xe data. In Figure 3–16, the observed p.e.s in each PMT, normalized to the mean value, are compared with each other. Necessary corrections are performed in the comparison. From the figure, the PMT gain difference is 7%. One of the sources of the PMT gain difference in Figure 3–16 is the imperfect isotropy of the scintillator ball.

To investigate the PMT gain more precisely, we performed the Xe calibration by the scintillator ball located at several positions with different ball directions. Observed p.e.s in each PMT are corrected for the anisotropy of the scintillation light which is measured separately. We make the table of the relative gain difference and this table is used for correcting the observed p.e.s in physics analyses. The uniformity of the detector response in physics analyses is studied in section 7.3.

3.3.3 Absolute Gain Calibration

In order to calibrate the absolute PMT gain, we utilize the gamma emission from thermal neutron capture of Nickel. The energy of the gamma is so low ($6 \sim 9$ MeV) that the

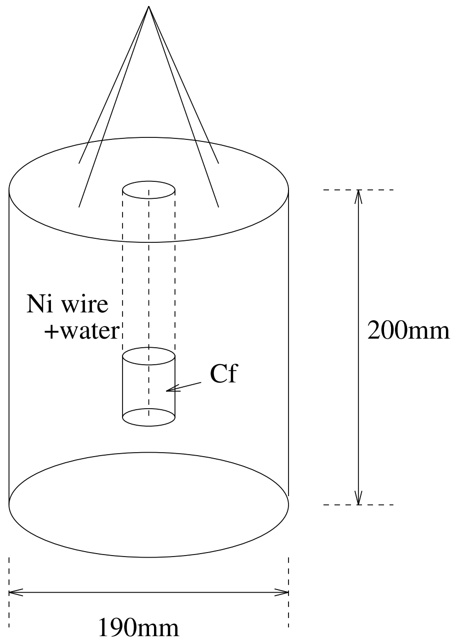

Figure 3–17: Schematic view of Ni+Cf gamma-ray source.

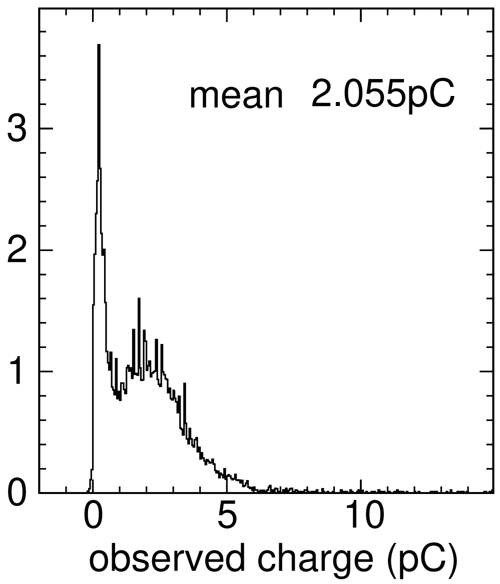

Figure 3–18: Observed charge (pC) for the Ni+Cf gamma-ray source.

expected number of hit photons for each fired PMT is one. Therefore, we can measure 1 p.e. distribution by this method.

Figure 3–17 shows the schematic view of the gamma ray source. We use ^{252}Cf as a neutron source. Emitted neutrons from the spontaneous fissions of ^{252}Cf are decelerated by water to be thermal neutrons. From the neutron capture of Ni, gamma-ray sources are produced.

Figure 3–18 shows the 1 p.e. distribution. Horizontal axis shows the observed charge in unit of pico-Coulomb (pC). From this calibration, we determine the relation between p.e. and pC as:

$$1 \text{ p.e.} = 2.055 \text{ pC} \tag{3-4}$$

3.3.4 Attenuation Length Measurement I

We measure the light attenuation length in the detector water by the system of a laser and a CCD camera. Figure 3–19 shows the measurement system. We use the nitrogen laser

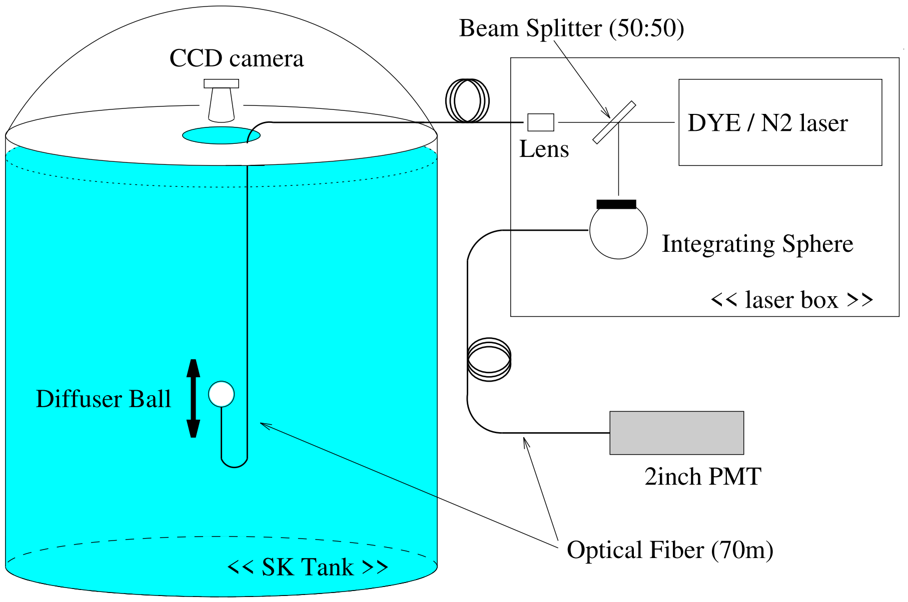

Figure 3–19: Schematic view of the attenuation length measurement system.

with dye which can produce monochromatic light with 337, 365, 400, 420, 460, 500, and 580 nm wavelength. We put the diffuser ball into the tank which is connected with the laser system by a optical fiber. Using the CCD camera on the top of the detector, we measure the light intensity of the ball image at several distances. The intensity of the laser light is also measured by the monitoring system.

Figure 3–20 shows the measured intensity by the CCD camera as a function of distance between the camera and diffuser ball. The light intensity is normalized by that measured by the monitoring system. The measured attenuation length from this figure is 97.9 m for 420

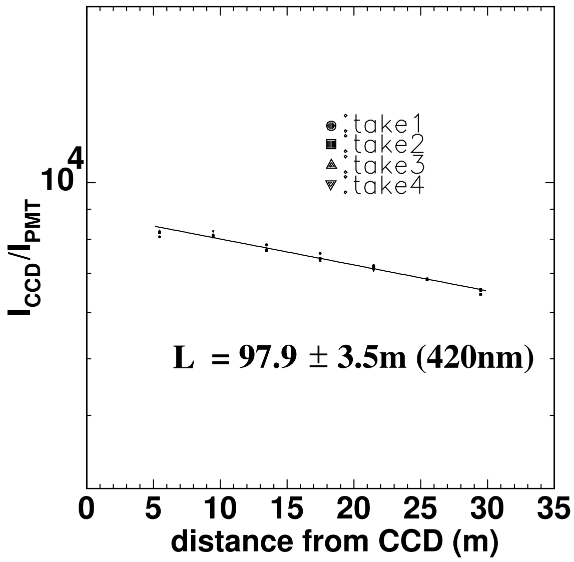

Figure 3–20: Measured light intensity as a function of distance. The light intensity is normalized by that measured by the monitoring system.

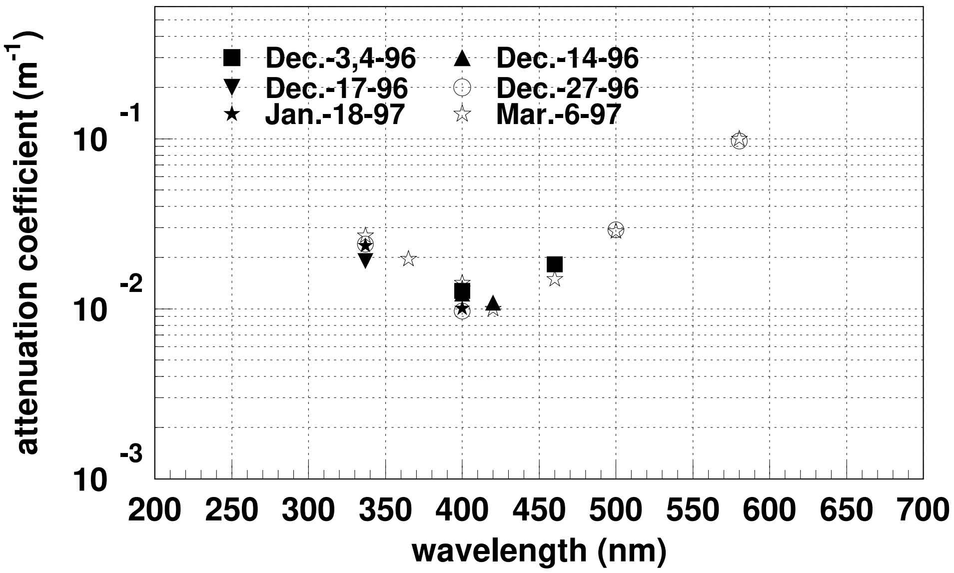

Figure 3–21: The wavelength dependences of photon attenuation coefficient measured by the laser system.

nm wavelength. Figure 3–21 summarizes the measured attenuation coefficients at each light wavelength.

3.3.5 Attenuation Length Measurement II

In Super–Kamiokande experiment, there are 2.7 Hz cosmic ray muon events. Using Cherenkov photons from muons, we measure the attenuation length in the detector water. Moreover, this analysis gives us the gain information of PMTs. The advantage of the muon analysis is that we regularly obtain the attenuation length and PMT gain every data taking period ($\sim$ 24 hours).

For this analysis, vertically through going muons are selected.

(a) $50000 <$ total number of p.e. < 125000

(b) entrance point $(x^{\rm in}, y^{\rm in}, z^{\rm in})$ is on the top wall and its $r^{\rm in} \equiv \sqrt{(x^{\rm in})^2 + (y^{\rm in})^2} <$ 15.9 m.

(c) exit point $(x^{\rm out}, y^{\rm out}, z^{\rm out})$ is on the bottom wall and its $r^{\rm out} \equiv \sqrt{(x^{\rm out})^2 + (y^{\rm out})^2} <$ 15.9 m.

(d) $\sqrt{(x^{\rm in} - x^{\rm out})^2 + (y^{\rm in} - y^{\rm out})^2} < 5$ m.

Criterion (a) roughly corresponds to the muon track length of 25 m to 63 m. The distance between the top and bottom wall is 39.2 m. This criterion also rejects energetic cosmic ray muons causing hadronic interactions in the detector. By criteria (b) and (c), the entrance and exit points are required on the top and bottom wall, respectively. Criterion (d) selects vertically going muons.

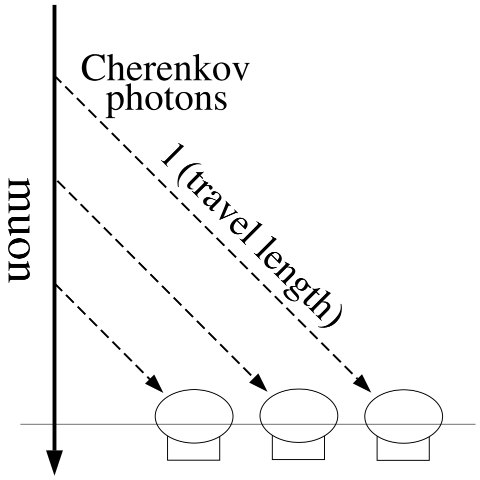

Figure 3–22: Schematic view of the attenuation length measurement by muons.

Figure 3–22 shows the schematic view of this analysis. By the muon data, we obtain the number of p.e.s detected by 20 inch PMTs located at each travel length l of Cherenkov photons. Therefore, we can check the travel length dependence of the number of Cherenkov photons. The detected p.e.s q are corrected for the travel length l and the PMT acceptance:

$$q_{\mathrm{corr}} = q \times l \times \frac{1}{f(\Theta)} \tag{3-5}$$

where $f(\Theta)$ is the PMT acceptance as a function of the incident angle and shown in Figure 6–9.

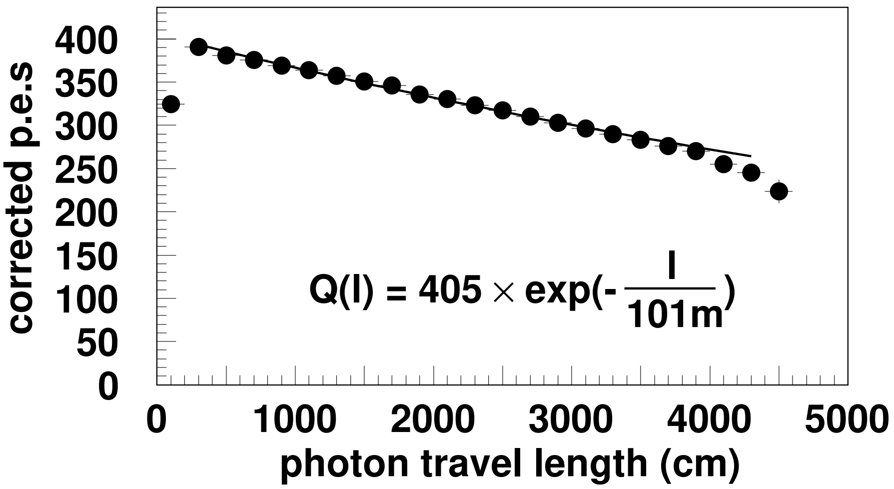

Figure 3–23: The travel length dependence of the corrected p.e.s. for muons. The line shows the fitting result by exponential function. The measured attenuation length (slope) is 101 m and PMT gain (intersection) is 405 p.e.s for this run.

Figure 3–23 shows the travel length dependence of the corrected p.e.s q_{corr}. This distribution is fitted by the exponential curve of

$$Q_{\mathrm{corr}}(l) = G \times \exp(-\frac{l}{L}). \tag{3-6}$$

where two fitting parameters of L and G are measured attenuation length and PMT gain, respectively. For Figure 3–23, the attenuation length is L = 101 m and the PMT gain is G = 405 p.e.s.

The stability of the attenuation length and PMT gain is discussed in section 7.2.

4 Simulation

We have developed a detailed Monte Carlo simulation program to estimate the detection efficiency of proton decays and the number of background events. Details of the simulation of the proton decay and the atmospheric neutrino interactions are described below.

4.1 Proton Decay Simulation

The source of protons for the proton decay search is water (H_2O) in the Super–Kamiokande detector. A H_2O molecule contains two free protons and eight bound protons. We assume that the proton decay should occur in equal probability for these protons.

In case of the decay of a free proton, kinematics of two body decay $p \to e^+\pi^0$ is uniquely calculated. The momentum of both the e^+ and π^0 is 459.43 MeV/c and one's direction is completely opposite to another's.

In case of a proton decay in oxygen, decay kinematics are different from the free proton due to Fermi motion of the proton, nuclear binding energy in oxygen, and nuclear effect for π^0. We use the Fermi momentum measured by electron scattering on ^{12}C [38]. The Fermi momentum for S-state and P-state are shown in Figure 4–1. The calculated kinematics

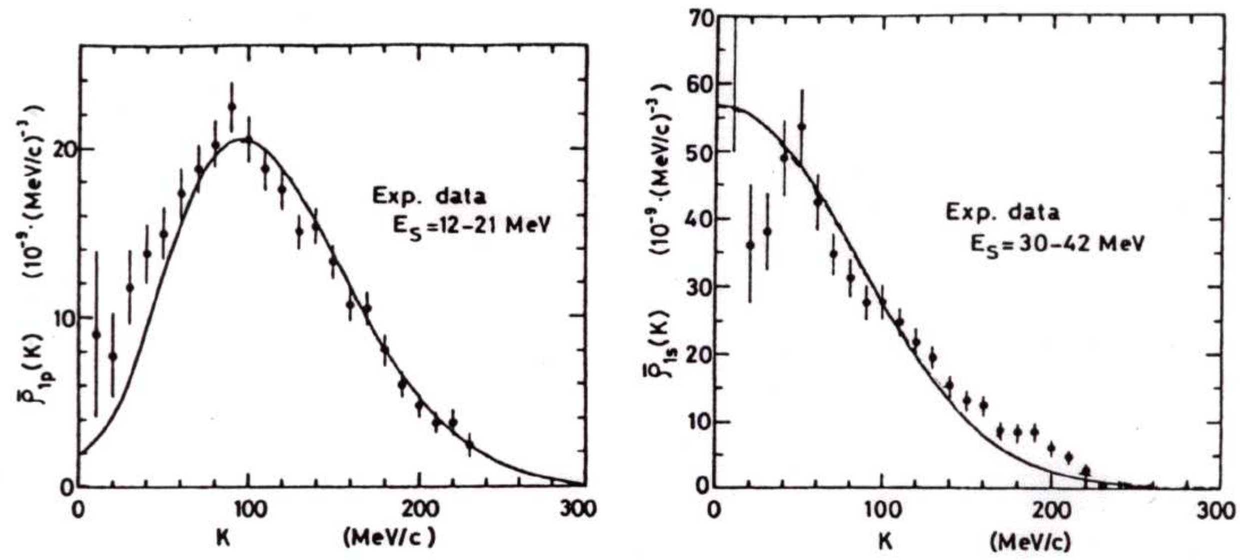

Figure 4–1: Fermi momentum distributions for P-state (left figure) and S-state (right figure). The points show experimental data measured by electron scattering on ^{12}C [38] and solid lines show theoretical calculation [38]. We use the calculated distributions in proton decay simulation.

of secondary particles in center of mass system are Lorentz boosted by the initial Fermi momentum. The nuclear binding energy is taken into account by modifying the proton mass as $M'_p = M_p - E_b$, where M'_p is the modified proton mass, M_p is the rest mass of a proton, and E_b is nuclear biding energy. The value of E_b is randomly selected for each simulated event from the probability density function of Gaussian $(\mu, \sigma) = (39.0\text{MeV}, 10.2\text{MeV})$ for S-state and $(\mu, \sigma) = (15.5\text{MeV}, 3.82\text{MeV})$ for P-state. Figure 4–2 shows the modified proton mass in oxygen.

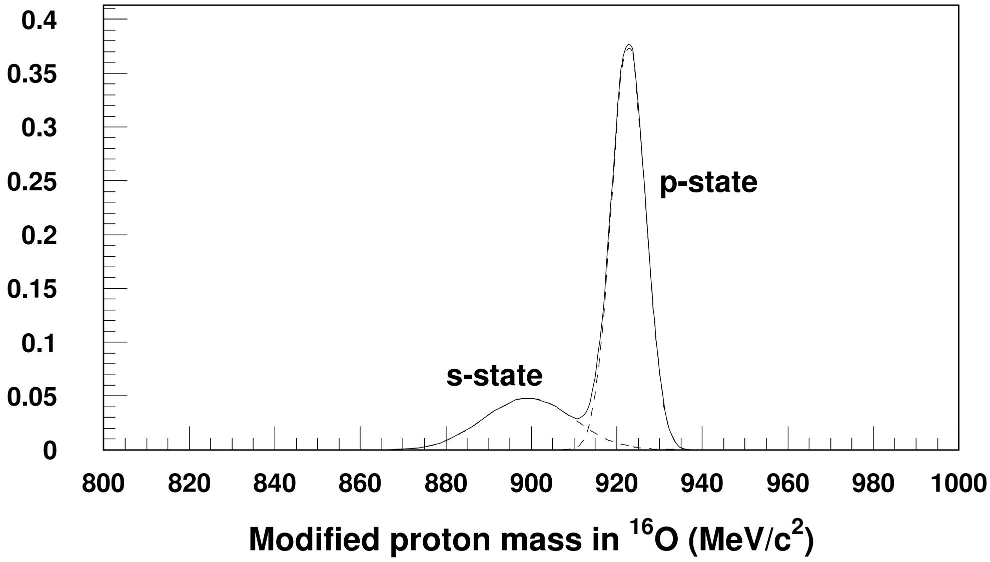

Figure 4–2: Modified proton mass in oxygen. The proton mass in oxygen is modified in order to take into account the nuclear binding energy.

The relative position of a decaying proton in oxygen is calculated according to the Wood-Saxon nuclear density

$$\rho_p(r) = \frac{Z}{A}\rho_0 \frac{1}{1 + \exp(\frac{r-c}{a})} \tag{4-1}$$

where r is the distance from the center of the oxygen. We chose $\rho_0 = 0.48 m_\pi^3$, $a = 0.41$ fm, and $c = 2.69$ fm for ^{16}O. This nuclear density distribution is shown in Figure 4–3.

The positron immediately escapes from ^{16}O nucleus into the detector water and in the water is traced in the detector simulator (section 4.5). However, the π^0 interacts in the ^{16}O nucleus strongly and we need to trace the π^0 in the nucleus. In the next section, the simulation of pion-nucleus scattering is described.

4.2 Nuclear Effect

Pions in ^{16}O nucleus often interact before leaving the nucleus and these interactions affect what we would observe for the $p \to e^+\pi^0$ signals as well as for atmospheric neutrino backgrounds. Therefore, pion interactions in nuclei are carefully simulated.

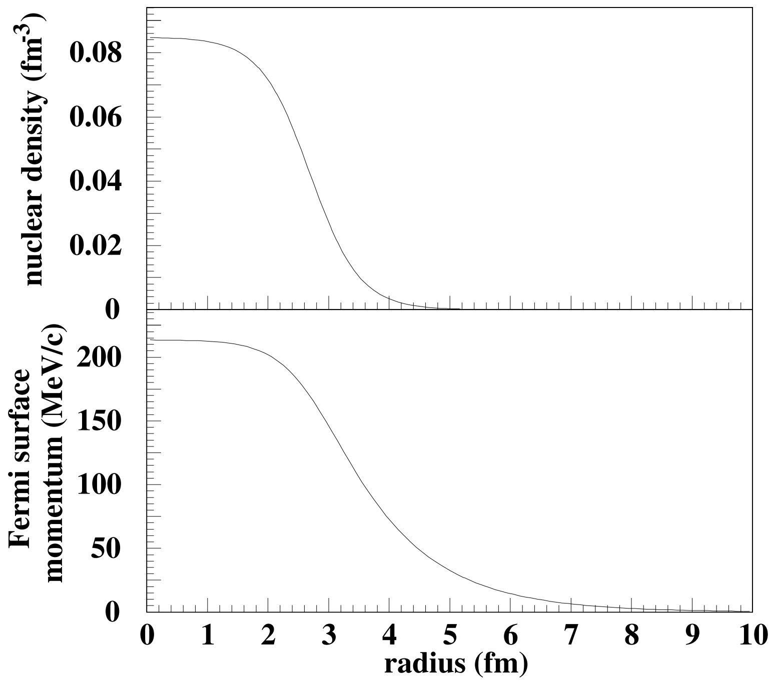

Figure 4–3: Wood-Saxon nuclear density and Fermi surface momentum.

In our simulation of the nuclear effect, inelastic scatterings, charge exchange, and absorption are considered. Elastic scattering is neglected because pion's angular distribution relative to positron's direction is predominantly determined by Fermi motion of initial proton. The cross section of each interaction is calculated by the model of Oset *et al.* [39]. In the cross section calculation, nuclear density in ^{16}O nucleus is assumed to be the Wood-Saxon form (Equation (4-1)). In order to decide the angular and momentum distribution of the scattered pions, we use the results of the phase shift analysis using the results of π–N scattering experiment [40]. Pauli exclusion principle are taken into account by requiring the momentum of final state nucleon to be over Fermi surface momentum of

$$p_F(r) = (\frac{3}{2}\pi^2\rho_p(r))^{\frac{1}{3}} \tag{4-2}$$

where $\rho_p(r)$ is nuclear density in ^{16}O nucleus. Fermi surface momentum distribution is shown in Figure 4–3.

For the consistency check, several simulation results are compared with experimental data. Figure 4–4 shows the differential cross sections of $^{16}\mathrm{O}(\pi^+, \pi^+)$ scattering for the simulation and experimental data.

With the π^+ beam and ^{16}O target, total cross sections of inelastic scatterings $^{16}\mathrm{O}(\pi^+, \pi^+)$, charge exchange $^{16}\mathrm{O}(\pi^+, \pi^-/\pi^0)$, and absorption as a function of pion momentum are shown in Figure 4–5. In the figure, calculation and data are compared. The calculated cross sections using our simulation agree with the experimental data.

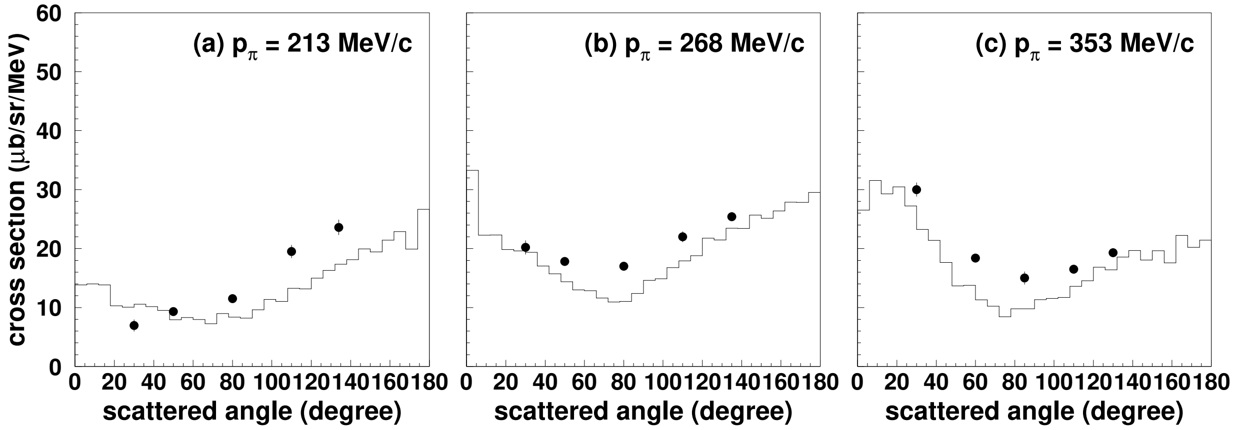

Figure 4–4: Differential cross sections of $^{16}O(\pi^+, \pi^+)$ for the simulation (histograms) and experimental data (points). The data points are taken from [41].

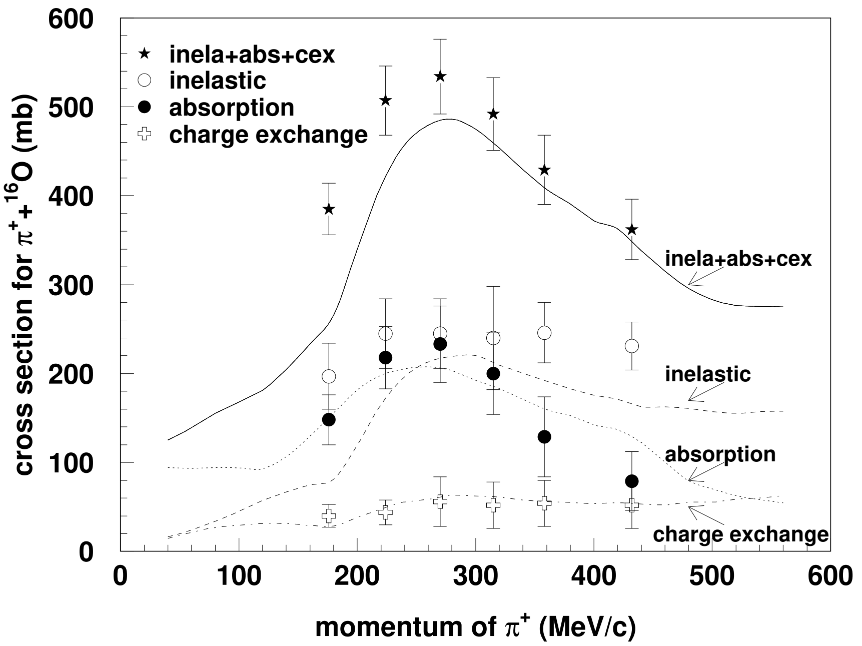

Figure 4–5: Cross sections of $\pi^+ + ^{16}O$ for inelastic scattering, charge exchange, and absorption. The calculated cross sections using our simulation (lines) are shown with experimental data (points) taken from [42].

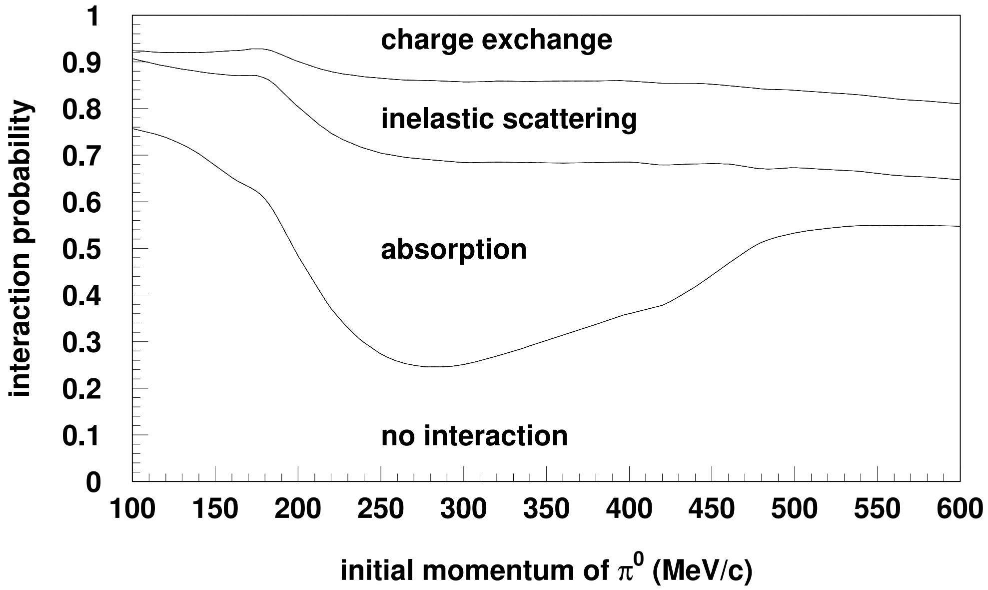

Figure 4–6: Probability of π^0 interactions in ^{16}O nucleus. Initial positions of π^0 are randomly selected according to the Wood-Saxon nuclear density.

The probability of π^0 interactions in ^{16}O nuclei is shown in Figure 4–6. In the figure, initial positions of π^0 are randomly selected according to the Wood-Saxon nuclear density. From the figure, 50–60% of π^0s from $p \rightarrow e^+\pi^0$ in oxygen interact before leaving the nucleus.

4.3 Atmospheric Neutrino

Atmospheric neutrinos are decay products of secondary particles which are produced in hadronic showers caused by primary cosmic rays high in the atmosphere. For the flux calculation, one needs to know the primary cosmic ray flux, hadron interaction, and atmospheric structure. Moreover, one needs to take into account the geomagnetic cutoff effect for primary cosmic rays. Since the cutoff energy depends on the geomagnetic field of the Earth, the atmospheric neutrino flux depends on magnetic latitude.

Among several author's calculations of the atmospheric neutrinos, we adopt the flux of Honda *et al.* [43] because they calculated the flux at Kamioka site and covered the range of 30 MeV to 3 TeV neutrino energy.

Figure 4–7 shows the primary cosmic ray fluxes. The chemical composition of the cosmic

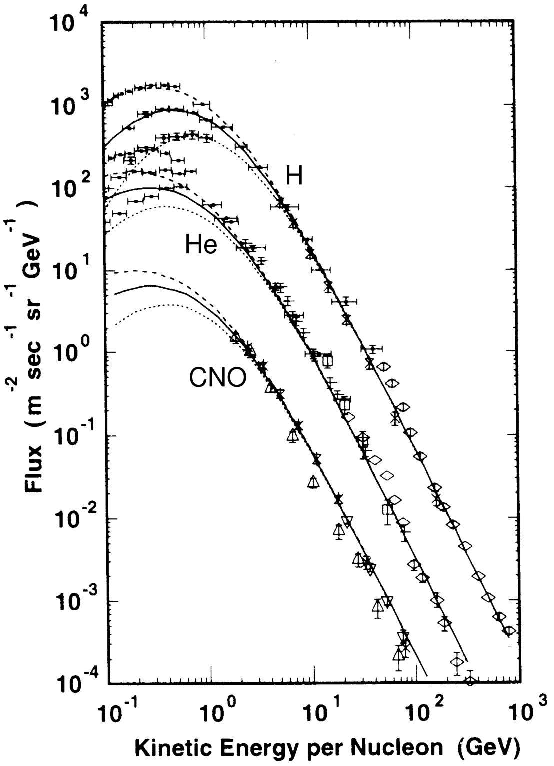

Figure 4–7: The chemical composition of the primary cosmic rays. Protons, helium nuclei, and CNO's are shown in the figure. Solid lines are fitting results for solar mid, dash lines for solar min, and dotted lines for solar max [43].

rays is $\sim$ 95% protons, $\sim$ 4.5% helium, and $\sim$ 0.3% CNO nuclei for the energy above 2 GeV/nucleus. As shown in the figure, low energy fluxes below a few GeV are affected by solar activity. Experimental uncertainty of the primary cosmic ray fluxes is $\sim$ 20% [44].

Various calculated neutrino fluxes at the Super–Kamiokande site are shown in Figure 4–8. The neutrinos with the energy around 1 GeV are relevant to the backgrounds of the $p \to e^+\pi^0$ search. The absolute flux uncertainty is estimated to be $\sim$ 25%.

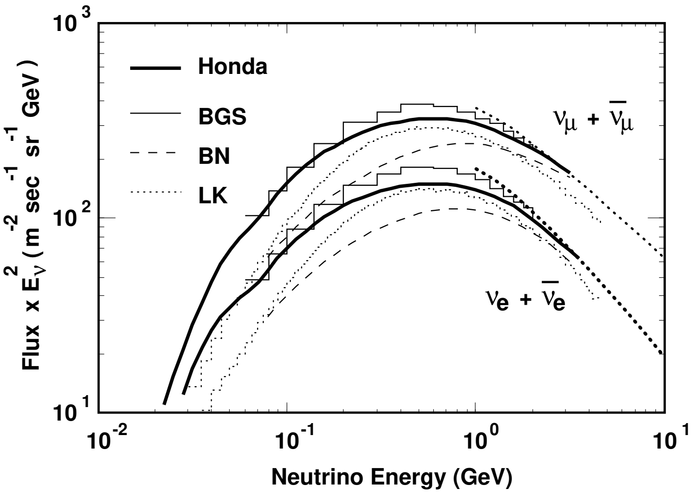

Figure 4–8: The calculated atmospheric neutrino fluxes. The fluxes of Honda *et al.* [43] are shown by solid lines (Honda). BGS are from [45], BN from [46], and LK from [47]. The dotted lines are the results from the Honda's calculation for high energy neutrinos without the rigidity cutoff.

4.4 Neutrino Interaction

Atmospheric neutrinos passing through the Super–Kamiokande detector interact with detector water. In our simulation, following charged current (CC) interactions and neutral current (NC) interactions are considered.

(a) CC quasi-elastic scattering $\nu + N \rightarrow l + N'$

(b) NC elastic scattering $\nu + N \rightarrow \nu + N$

(c) CC single-pion production $\nu + N \rightarrow l + N' + \pi \quad (W < 1.4\mathrm{GeV}/c^2)$

(d) NC single-pion production $\nu + N \rightarrow \nu + N' + \pi \quad (W < 1.4\mathrm{GeV}/c^2)$

(e) CC multi-pion production $\nu + N \rightarrow l + N' + m\pi \quad (m \geq 2 \text{ if } 1.3 < W < 1.4\mathrm{GeV}/c^2)$

$(m \geq 1 \text{ if } 1.4\mathrm{GeV}/c^2 < W)$

(f) NC multi-pion production $\nu + N \rightarrow \nu + N' + m\pi \quad (m \geq 2 \text{ if } 1.3 < W < 1.4\mathrm{GeV}/c^2)$

$(m \geq 1 \text{ if } 1.4\mathrm{GeV}/c^2 < W)$

(g) CC coherent pion production $\nu + {}^{16}\mathrm{O} \rightarrow l^{\pm} + \pi^{\mp} + {}^{16}\mathrm{O}$

(h) NC coherent pion production $\nu + {}^{16}\mathrm{O} \rightarrow \nu + \pi^0 + {}^{16}\mathrm{O}$

where ν is a neutrino or an anti-neutrino, N and N' are nucleons (protons or neutrons), l is a charged lepton, m is multiplicity of pions, and W is invariant mass of the hadronic system. Each interaction is described in the following sections. Neutrino–electron scattering is safely neglected due to small cross sections compared with those of neutrino–nucleon scattering. Moreover, strange particle production, whose cross section is also very small, is neglected in our simulation.

4.4.1 Quasi-Elastic Scatterings and Elastic Scatterings

For the neutrino–nucleon CC quasi-elastic scatterings, q^2 ($q_\nu \equiv p_\nu(\nu) - p_\nu(l)$, 4-momentum transfer) dependence of weak hadronic current is expressed using form factors of nucleons;

$$J_\nu^{hadron} = \cos\theta_c \bar{u}(N') \left(\gamma_\nu F_V^1(q^2) + \frac{i\sigma_{\nu\mu} q^\mu (\mu_p - \mu_n) F_V^2(q^2)}{2M_N} + \gamma_\nu\gamma_5 F_A(q^2) \right) u(N) \tag{4-3}$$

where $F_V^1(q^2)$ and $F_V^2(q^2)$ are vector form factors, $F_A(q^2)$ is axial vector form factor, θ_c is the Cabibbo angle, M_N is a nucleon mass, and μ_p and μ_n are the anomalous magnetic moments of the proton and neutron, respectively. The form factors of $F_V^1(q^2)$, $F_V^2(q^2)$, and $F_A(q^2)$ are expressed as following.

$$\begin{aligned} F_V^1(q^2) &= \left(1 - \frac{q^2}{4M^2}\right)^{-1} \left(G_E^V(q^2) - \frac{q^2}{4M^2} G_M^V(q^2) \right) \\ \xi F_V^2(q^2) &= \left(1 - \frac{q^2}{4M^2}\right)^{-1} \left(G_M^V(q^2) - G_E^V(q^2) \right) \end{aligned} \tag{4-4}$$

$$G_E^V(q^2) = \frac{1}{\left(1 - \frac{q^2}{M_V^2}\right)^2}, \quad G_M^V(q^2) = \frac{1+\xi}{\left(1 - \frac{q^2}{M_V^2}\right)^2}, \quad \xi = \mu_p - \mu_n = 3.71,$$

$$F_A(q^2) = \frac{-1.23}{\left(1 - \frac{q^2}{M_A^2}\right)^2}$$

Parameters in the form factors are determined from the experimental data [48]. Vector mass M_V and axial vector mass M_A are taken to be 0.84 GeV/c^2 and 1.01 GeV/c^2, respectively. Along with the weak lepton current, the cross sections for the quasi-elastic scattering are calculated from Equation (4-3). Figure 4–9 and 4–10 show the calculated total cross sections for $\nu_\mu + n \to \mu^- + p$ and $\bar{\nu}_\mu + p \to \mu^+ + n$, respectively, along with experimental data.

For the NC elastic scattering, we use the following relations according to [53].

$$\sigma(\nu p \to \nu p) = 0.153 \times \sigma(\nu n \to e^- p) \tag{4-5}$$
$$\sigma(\bar{\nu} p \to \bar{\nu} p) = 0.218 \times \sigma(\bar{\nu} p \to e^+ n) \tag{4-6}$$
$$\sigma(\nu n \to \nu n) = 1.5 \times \sigma(\nu p \to \nu p) \tag{4-7}$$
$$\sigma(\bar{\nu} n \to \bar{\nu} n) = 1.0 \times \sigma(\bar{\nu} p \to \bar{\nu} p) \tag{4-8}$$

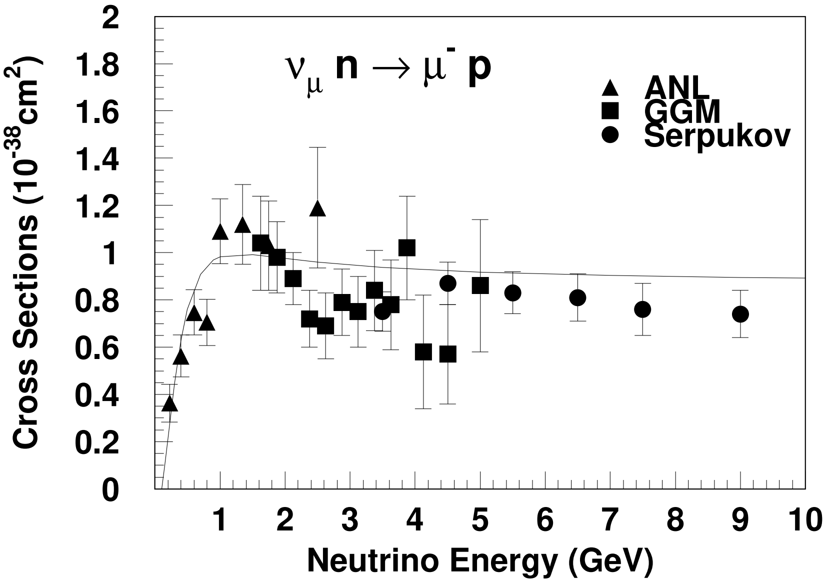

Figure 4–9: Calculated total cross sections for $\nu_\mu + n \rightarrow \mu^- + p$. Experimental data are also shown for ANL [49], GGM [50], and Serpukov [51].

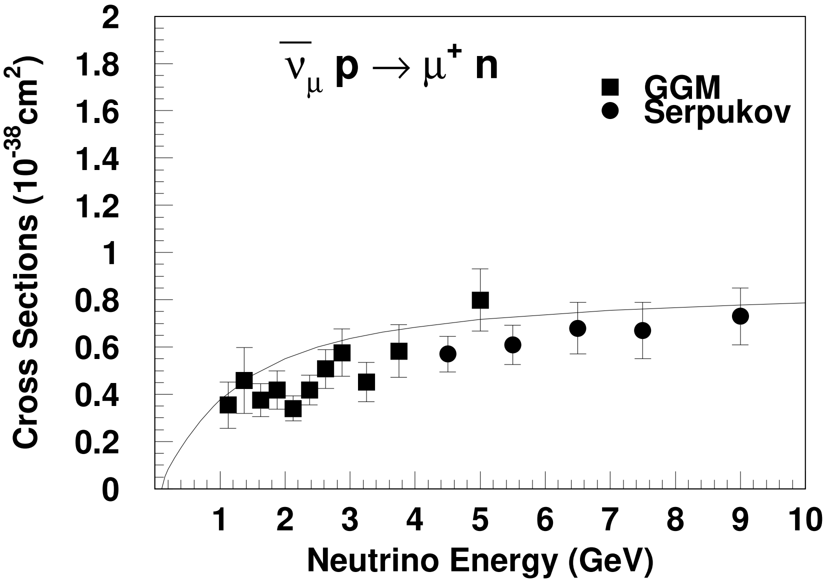

Figure 4–10: Calculated total cross sections for $\bar{\nu}_\mu + p \rightarrow \mu^+ + n$. Experimental data are also shown for GGM [52] and Serpukov [51].

In case of a bound nucleon target, we take into account Fermi motion of a target nucleon. Moreover, Pauli blocking effect is taken into account by requiring the final nucleon momentum to be over Fermi surface momentum (250 MeV/c). Figure 4–11 shows the calculated total cross sections of each (quasi-)elastic scattering both for free protons (solid lines) and bound nucleons (dashed lines).

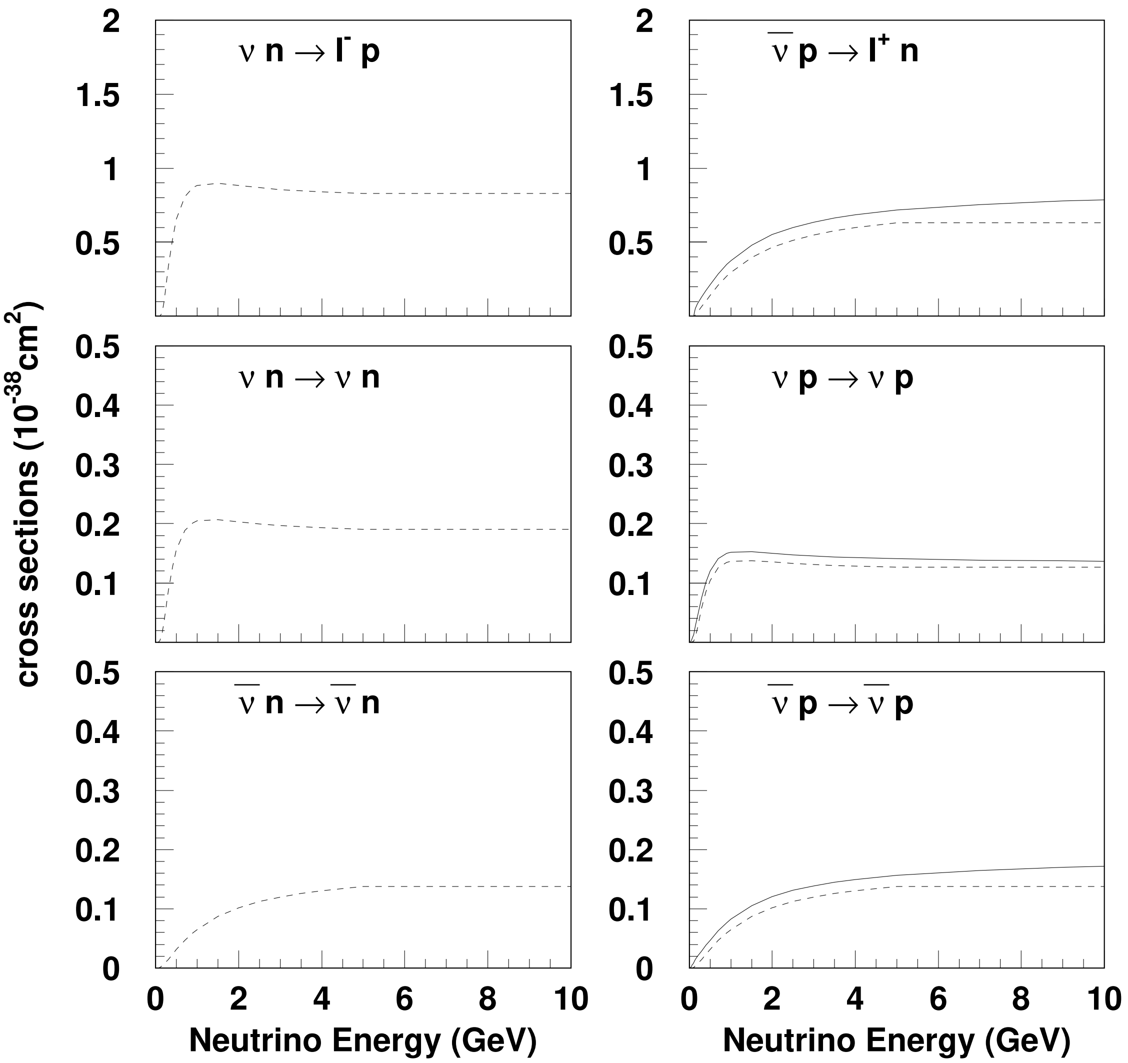

Figure 4–11: Calculated total cross sections for (quasi-)elastic scatterings. Solid lines show the free proton targets and dashed lines show the bound nucleon targets.

4.4.2 Single-Pion Productions

Single-pion production is simulated using the method by Rein and Sehgal [54]. In their method, the single-pion production is mediated by baryon resonances as:

$$\text{resonance production} \qquad \nu + N \rightarrow \nu/l + N^*$$

$$\text{resonance decay} \qquad N^* \rightarrow \pi + N'$$

where N^* is one of baryon resonances and N and N' are nucleons. 18 baryon resonances are considered in their method. Amplitude for each resonance production is calculated with the weight of the probability of the resonance decays to one pion and one nucleon. In our simulation, hadronic invariant mass W is restricted to be $W < 1.4$ GeV/c^2 in order to keep consistency with multi-pion productions (see section 4.4.3).

The cross section for each single-pion production mode is calculated from these amplitudes. Interference among these resonances is taken into account. The calculated cross sections of the CC single-pion productions are shown in Figure 4–12, 4–13, and 4–14 with experimental data. In the figures, the calculated cross sections agree well with the experimental data. Calculated cross sections of each CC and NC single-pion production channel are shown in Figure 4–15.

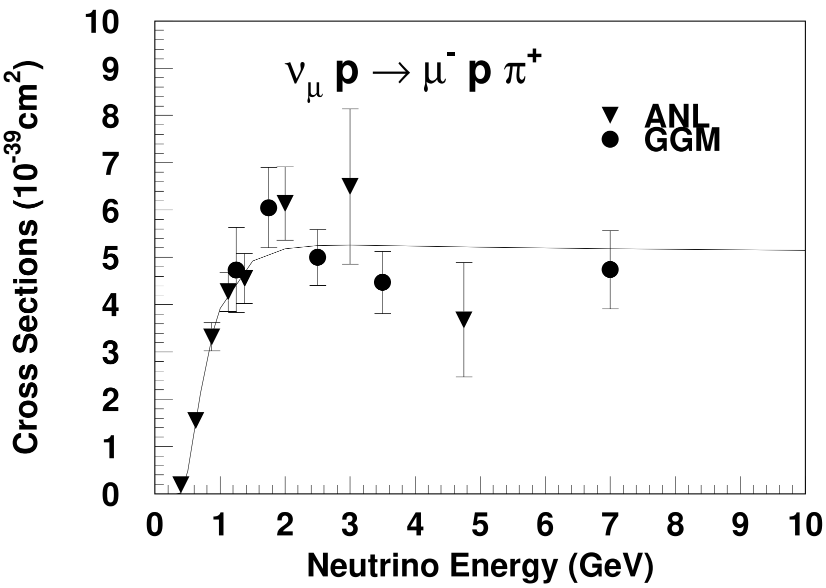

Figure 4–12: Cross sections of CC single-pion production $\nu_\mu p \rightarrow \mu^- p \pi^+$. Calculation (solid line) is shown with experimental data from ANL [55] and GGM [56].

To decide decay kinematics of the resonance $\Delta(1232)$, which is dominant resonance in the region of $W < 1.4$ GeV/c, we also use Rein-Sehgal's method. For the decay of other resonances, the pion direction is assumed to be uniform in the resonance rest frame. Figure 4–16 shows the angular distribution of pions in the reaction of $\nu p \rightarrow \mu^- p \pi^+$ for our simulation and experimental data [57].

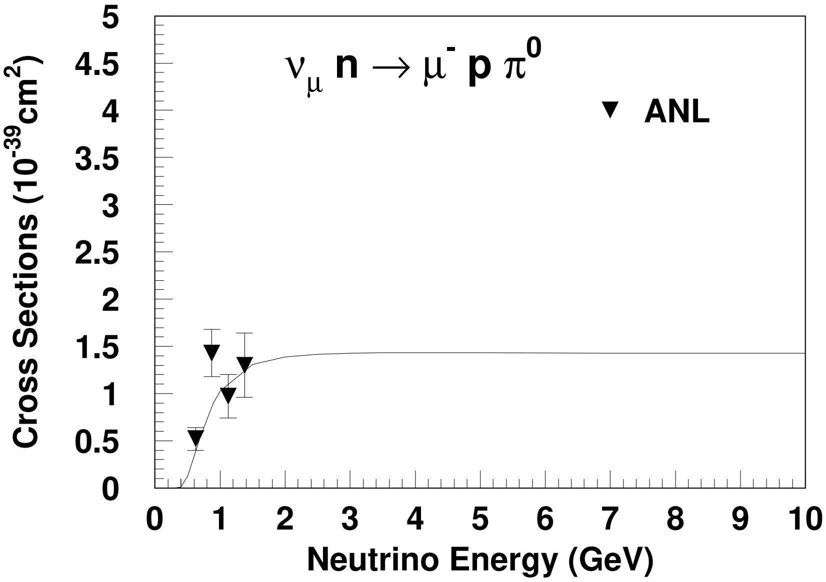

Figure 4–13: Cross sections of CC single-pion production $\nu_\mu n \to \mu^- p \pi^0$. Calculation (solid line) is shown with experimental data from ANL [55].

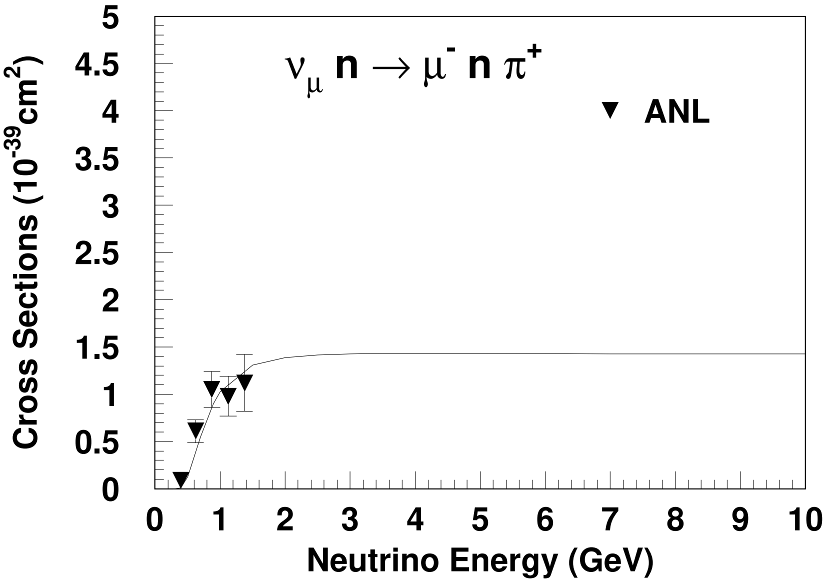

Figure 4–14: Cross sections of CC single-pion production $\nu_\mu n \to \mu^- n \pi^+$. Calculation (solid line) is shown with experimental data from ANL [55].

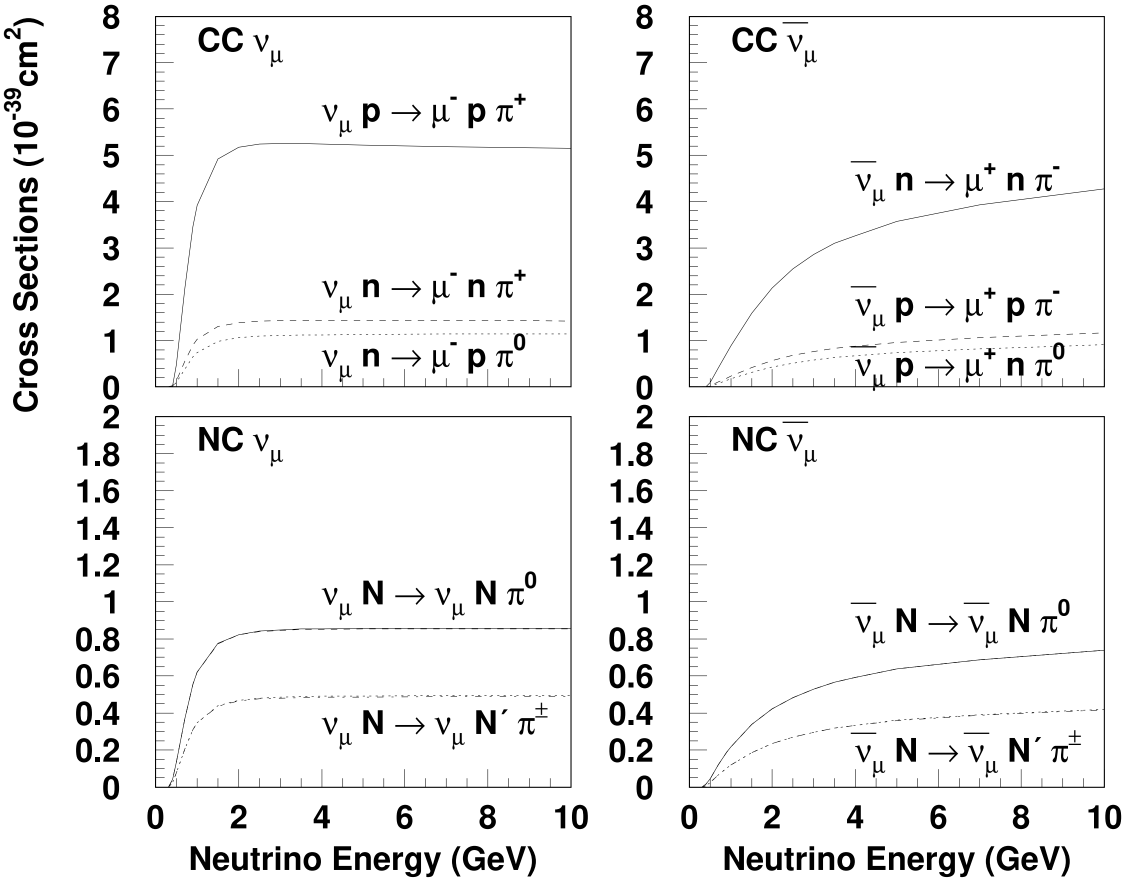

Figure 4–15: Calculated cross sections of CC and NC single-pion productions.

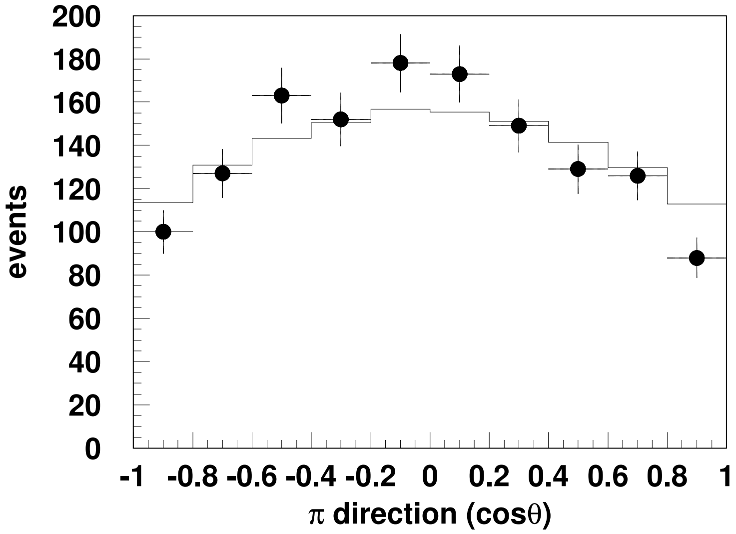

Figure 4–16: Angular distribution of pions from the $\Delta(1232)$ decay in the interaction $\nu p \rightarrow \mu^- p \pi^+$. In Adler frame (rest frame of resonance), θ is defined as opening angle between the pion direction and $(\vec{k}_1 - \vec{k}_2)/|\vec{k}_1 - \vec{k}_2|$ where $\vec{k}_1$ and $\vec{k}_2$ are the momentum vector of the initial and final lepton, respectively. The calculation (solid line) is shown along with experimental data [57].

4.4.3 Multi-Pion Productions

The cross section of CC deep inelastic neutrino-nucleon scattering is expressed as:

$$\begin{aligned}
\frac{d^2\sigma^{\nu,\bar{\nu}}}{dxdy} &= \frac{G_F^2 M_N E_\nu}{\pi}\left((1 - y + \frac{1}{2}y^2 + C_1)F_2(x,q^2) \pm y(1 - \frac{1}{2}y + C_2)xF_3(x,q^2)\right) \quad (4\text{-}9)\\
C_1 &= \frac{yM_l^2}{4M_N E_\nu x} - \frac{xyM_N}{2E_\nu} - \frac{M_l^2}{4E_\nu^2} - \frac{M_l^2}{2M_N E_\nu x}\\
C_2 &= -\frac{M_l^2}{4M_N E_\nu x}
\end{aligned}$$

where $x = -q^2/(2M_N(E_\nu - E_l))$ is Bjorken scaling variable, $y = (E_\nu - E_l)/E_\nu$ is the fractional energy transferred to the hadron system, $M_N(M_l)$ is nucleon (lepton) mass and $E_\nu(E_l)$ is initial neutrino (final lepton) energy. The nucleon structure functions F_2 and xF_3, as a function of x and q^2, are taken from the $\overset{(-)}{\nu}_\mu$+Fe scattering experiment [58]. By integrating Equation (4-9) with the constraint of $W > 1.3$ GeV$/c^2$, where W is the invariant mass of the hadronic system, we get the CC cross section of multi-pion production, $\overset{(-)}{\nu} N \rightarrow \mu^\pm N' m\pi$ $(m \geq 1)$. In the integration in the region of $1.3\text{GeV}/c^2 < W < 1.4\text{GeV}/c^2$, the contribution from one pion productions $(m = 1)$ is subtracted in order to keep consistency with the single-pion productions described in section 4.4.2.

Using the measurement of charged pion multiplicity by the Fermilab 15-foot hydrogen bubble chamber experiment [59], we adopt the mean multiplicity of each pion to be

$$< n_\pi >= 0.09 + 1.83 lnW^2 \tag{4-10}$$

where $< n_{\pi^+} >=< n_{\pi^-} >=< n_{\pi^0} >$ is assumed. For an individual Monte Carlo event, the pion multiplicity is determined using KNO (Koba-Nielsen-Olesen) scaling [60]. Figure 4–17 compares the calculated multiplicity from KNO scaling with experimental data [59].

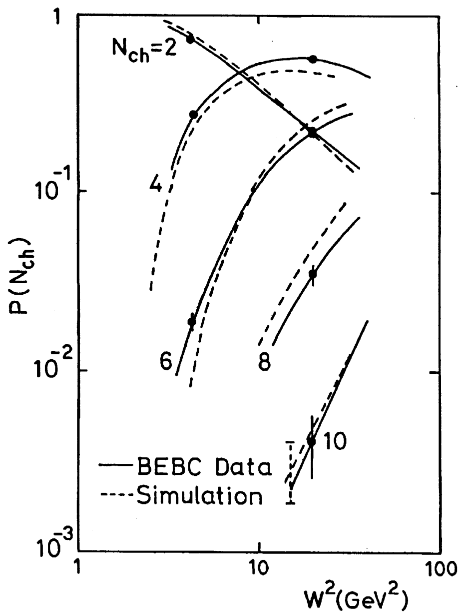

Figure 4–17: KNO scaling for the $\nu_\mu p \to \mu^- X$ process, together with the data from BEBC experiment [59].

We also adopt the forward-backward asymmetry of the produced pions in the hadronic center of mass system [61]

$$\frac{n_\pi^{forward}}{n_\pi^{backward}} = \frac{0.35 + 0.41 lnW^2}{0.5 + 0.09 lnW^2} \tag{4-11}$$

where 'forward' means the direction of the hadronic system in the laboratory frame.

For the NC multi-pion production, we adopt the following relations between CC cross section and NC cross section which have been estimated from experimental data [62].

$$\frac{\sigma(\nu N \to \nu X)}{\sigma(\nu N \to \mu^- X)} = \begin{cases} 0.26, & E_\nu \leq 3\text{GeV} \\ 0.26 + 0.04 \times \dfrac{E_\nu - 3}{3}, & 3\text{GeV} \leq E_\nu \leq 6\text{GeV} \\ 0.30, & 6\text{GeV} \leq E_\nu \end{cases} \tag{4-12}$$

$$\frac{\sigma(\bar{\nu} N \to \bar{\nu} X)}{\sigma(\bar{\nu} N \to \mu^+ X)} = \begin{cases} 0.39, & E_\nu \leq 3\text{GeV} \\ 0.39 - 0.02 \times \dfrac{E_\nu - 3}{3}, & 3\text{GeV} \leq E_\nu \leq 6\text{GeV} \\ 0.37, & 6\text{GeV} \leq E_\nu \end{cases} \tag{4-13}$$

The calculated total cross sections of CC neutrino interactions and CC anti neutrino interactions are shown in Figure 4–18 and 4–19, respectively, along with experimental data. Here, total cross sections are calculated by summing up the cross sections of quasi-elastic scatterings, single-pion productions, and multi-pion productions.

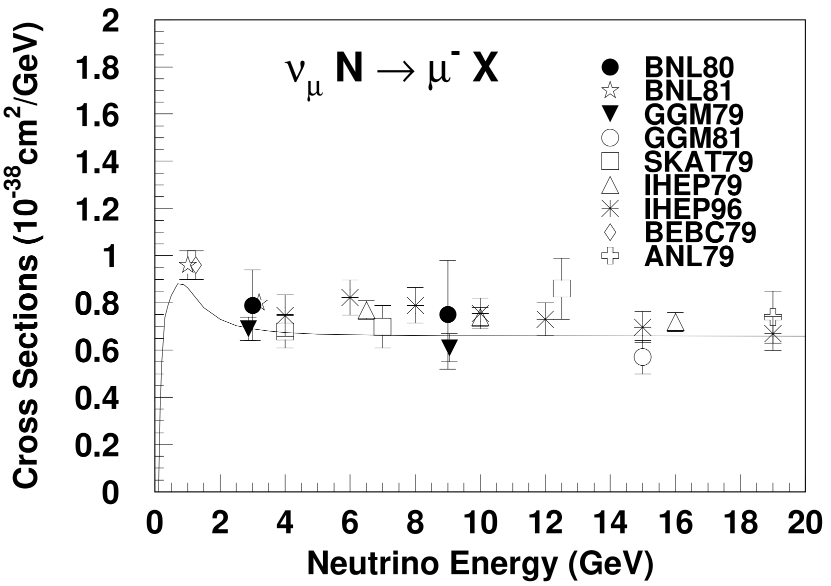

Figure 4–18: The total cross section of CC neutrino interactions. Calculation (solid line) is shown along with experimental data of BNL80 [63], BNL81 [64], GGM79 [65], GGM81 [66], SKAT79 [67], IHEP79 [68], IHEP96 [69], BEBC79 [70], and ANL79 [71].

4.4.4 Coherent Pion Productions

In coherent neutrino-nucleus interactions, the nucleus recoils as whole, without any change of charge or isospin. Because the transferred momentum is very small in the processes, angular distributions of recoil leptons and produced pions have sharp peaks in the forward direction. The cross sections for the coherent pion productions are expressed [73] as

$$\frac{d\sigma}{dxdyd|t|} = \frac{G_F^2 M_N}{2\pi^2} f_\pi^2 A^2 E_\nu (1-y) \frac{1}{16\pi} (\sigma_{total}^{\pi N})^2 (1+r^2) (\frac{M_A^2}{M_A^2+Q^2})^2 e^{-b|t|} F_{abs} \quad (4\text{-}14)$$

$$r = \frac{Ref_{\pi N}(0)}{Imf_{\pi N}(0)} \quad (4\text{-}15)$$

where $f_\pi = 0.93 m_\pi$, $A(=16)$ is atomic number of oxygen, M_A is the axial-vector mass, $b = 80\text{GeV}^{-2}$, t is the square of 4-momentum transferred to the nucleus. F_{abs} is the term for taking into account the pion absorption in the nucleus. Calculated cross sections are shown in Figure 4–20.

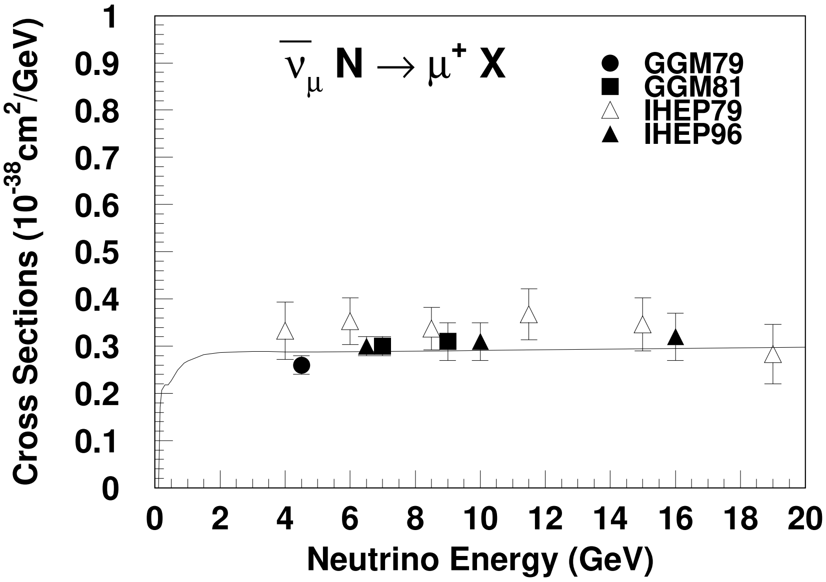

Figure 4–19: The total cross section of CC anti-neutrino interactions. Calculation (solid line) is shown along with experimental data of GGM79 [72], GGM81 [66], IHEP79 [68], and IHEP96 [69].

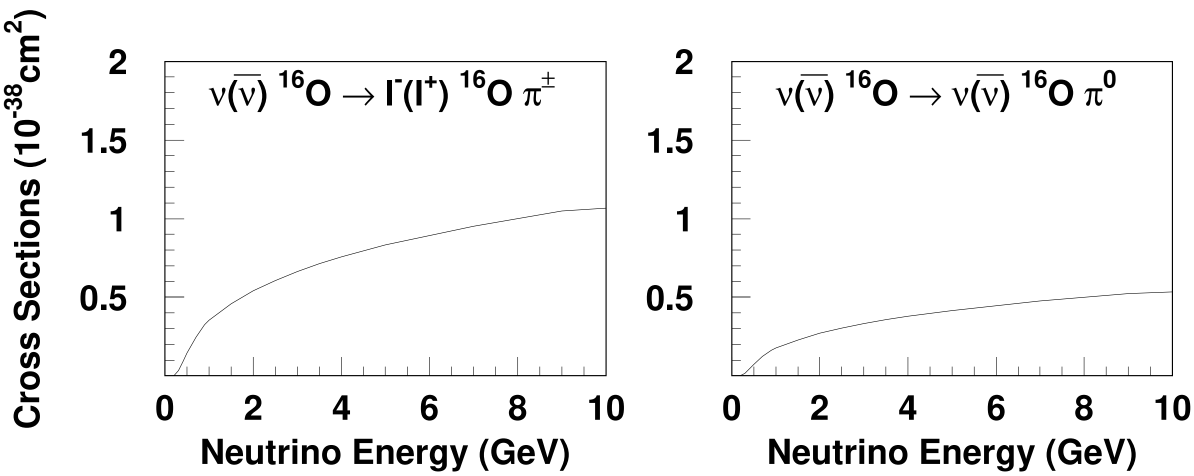

Figure 4–20: The cross sections of coherent pion productions.

4.5 Detector Simulation

Simulated kinematics of proton decays and neutrino interactions are passed through a detector simulation program. The detector simulation simulates the propagation of particles, Cherenkov radiation, propagation of Cherenkov photons in the detector water, and the response of the PMTs and ADC/TDC electronics. Based on the GEANT package [74], the custom detector simulation program was developed for the Super–Kamiokande detector.

4.5.1 Photon Generation and Propagation

In this detector simulation, Cherenkov photons are generated according to Equation (3-2) and (3-3). The photons propagate in the water with the group velocity $c/n'(\lambda)$ where $n'(\lambda)$ is wavelength dependent, effective refractive index. Figure 4–21 shows the effective refractive index in our simulation.

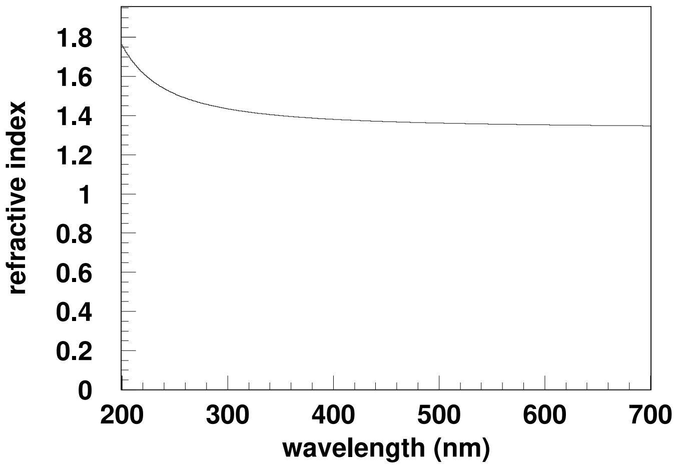

Figure 4–21: The effective refractive index in water. The group velocity of light is $c/n'(\lambda)$ where $n'(\lambda)$ is the effective refractive index.

In the propagation of the photons in water, scattering and absorption processes are taken into account in the simulation. For photons with short wavelength ($\lambda \lesssim 450$ nm), Rayleigh scattering is a dominant interaction which is caused by small particles ($r \ll \lambda$, r is radius of a particle and λ is wavelength of photon) in water as well as by H_2O molecule. The cross section is written as

$$\frac{d\sigma}{d\Omega} = \frac{r^6}{\lambda^4} \left| \frac{\varepsilon - 1}{\varepsilon + 2} \right|^2 |\vec{\epsilon}_i \cdot \vec{\epsilon}_f|^2 \tag{4-16}$$

where ε is permittivity of the particle, $\vec{\epsilon}_i$ and $\vec{\epsilon}_f$ are initial and final polarization vector of the photon, respectively. The cross section has a power dependence of λ^{-4} and becomes large at short wavelength. For longer wavelength ($\lambda \gtrsim 450$ nm), an absorption by H_2O molecule becomes the dominant process. The amplitude of the absorption as a function of a wavelength are taken from experimental data. Moreover, Mie scattering, which has sharp peak in forward direction, is considered in our simulation. This scattering is caused by relatively large particle ($r \gg \lambda$). Figure 4–22 shows the angular distribution of Rayleigh scattering and Mie scattering. Figure 4–23 shows the wavelength dependence of attenuation coefficient of photons in our simulation compared with measurement results of the laser system (section 3.3.4). In our simulation, the attenuation coefficients of the Rayleigh scattering and Mie scattering are tuned to be consistent with the laser measurement. Moreover, these parameters are confirmed by cosmic ray muon events (section 3.3.5).

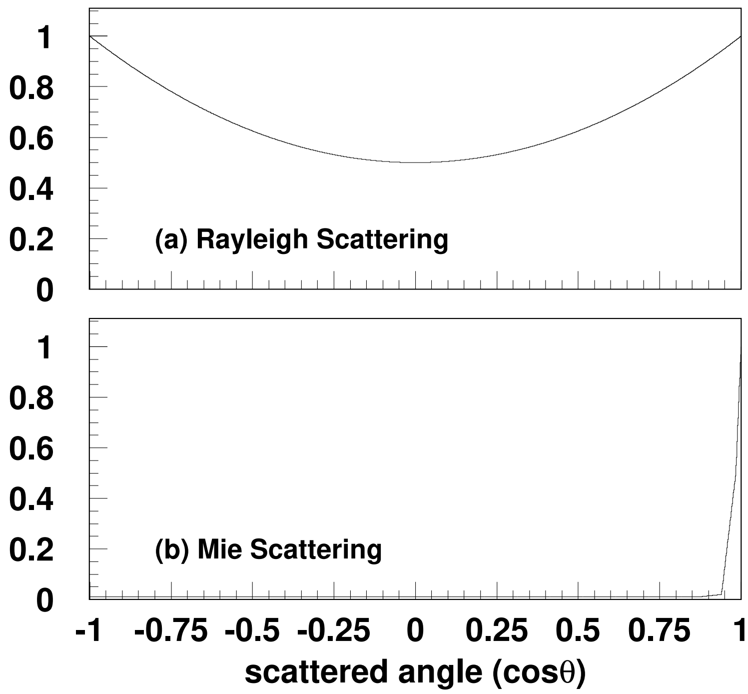

Figure 4–22: The angular distribution of Rayleigh and Mie scatterings.

When a photon arrives at black plastic sheet, reflection or absorption are simulated using the measured probabilities shown in Figure 4–24.

On arriving at the PMT surface, some of photons are reflected according to the measured probability shown in Figure 4–25. For simulating PMT response in photon detection, measured quantum efficiency shown in Figure 3–6 is used. Total amount of detected p.e.s in each PMT is calculated by summing up the individual detected p.e. using measured one p.e. distribution (Figure 3–7). For simulating timing resolution, timing information in each PMT is smeared according to measured timing resolution as a function of detected p.e.s. The measured timing resolution is already shown in Figure 3–14.

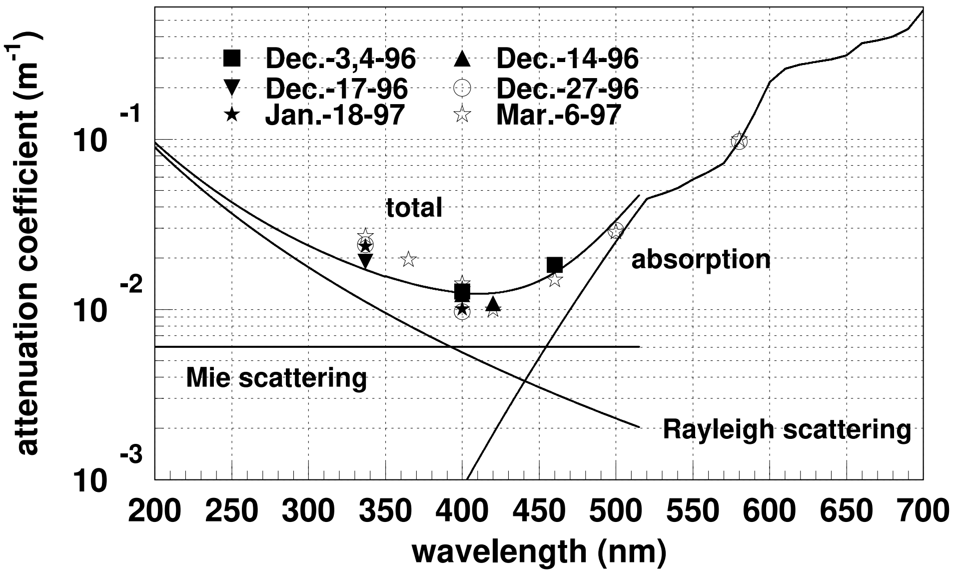

Figure 4–23: The wavelength dependences of photon attenuation coefficient in our simulation (solid lines) are shown compared with measurement results by the laser system (section 3.3.4).

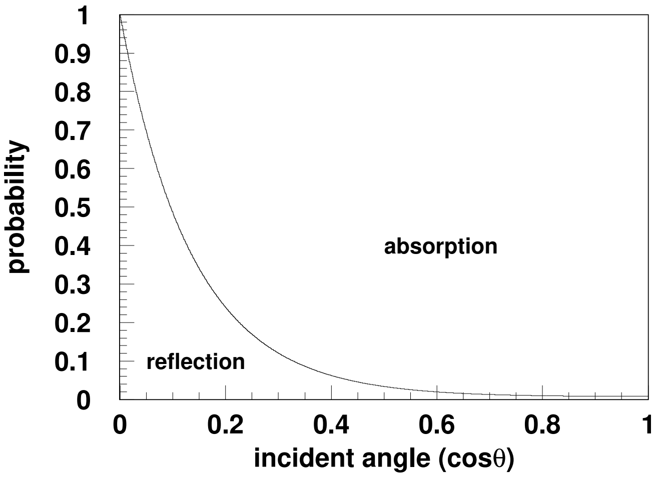

Figure 4–24: The reflection and absorption probability of light on black sheet. The vertical direction corresponds to $\cos\theta = 1$.

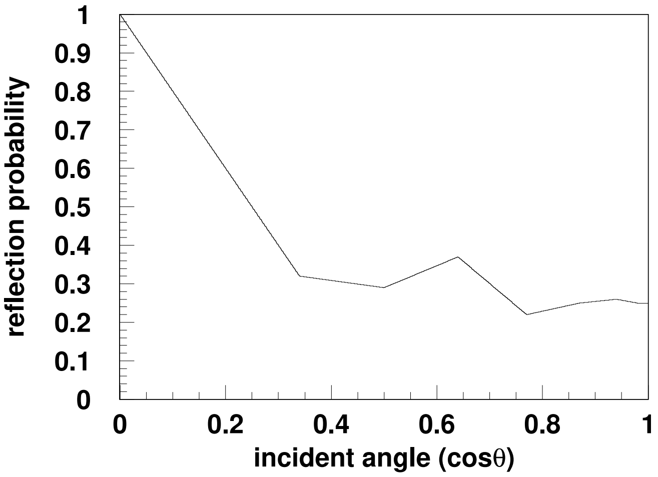

Figure 4–25: The reflection probability of light on PMT surface. The vertical direction corresponds to $\cos\theta = 1$. Measured points are connected and used in our simulation.

4.5.2 Hadron Propagation

If a π^0 escapes from ^{16}O nucleus or a π^0 is generated by free proton interactions, it immediately decays to two gammas (98.8% branching ratio). However, $\pi^\pm$ have relatively long lifetime and we need to simulate the pion propagation in water. We select CALOR [75] program for simulating hadronic interactions in water which well reproduces pion interactions even in low energy ($\sim$ 1GeV) region. For much lower energy region ($p_\pi \leq 500$ MeV/c), we developed a custom hadron simulation program [40] which uses measured pion cross sections [76]. In the custom simulation program, we considered elastic scatterings, inelastic scatterings, absorptions, and charge exchange.

5 Event Selection

5.1 Reduction for Fully Contained Sample

Since its start of operation on 1st April 1996, the Super–Kamiokande has been continuously taking data except 10% down time due to detector calibrations, maintenances of the detector and so on. The 90% live-time data are sent to physics analysis streams. The rate of trigger we use in this analysis is about 10 Hz and about 800,000 events are recorded every day. 2.7 Hz are due to cosmic ray muons in which 2 Hz muons enter the inner detector. About 6 Hz are due to relatively low energy (a few MeV) events caused by radioactivity in the detector water or gamma ray from surrounding PMTs and rocks. Remaining 1 Hz are due to fake triggers caused by reflection of PMT signals or unwanted PMT signals following highly energetic events ("after pulsing").

Therefore, we should eliminate these backgrounds while accepting the possible proton decay signals. What we are looking for are signal events which occur in the inner detector and have about 1 GeV energy deposit. The reduction algorithms for this analysis select fully contained events in which at least 30 MeV visible energy is observed in the inner detector and no outer detector activity is seen. The selected events are called fully contained events which are commonly used for the proton decay searches and the atmospheric neutrino analyses.

The reduction procedure consists of several reduction steps as shown in Figure 5–1. Starting from the raw data of 800,000 events/day, four reduction software are applied to reject

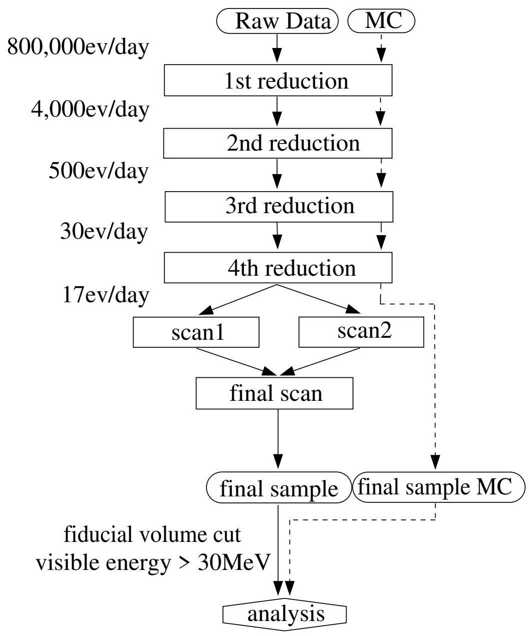

Figure 5–1: The reduction flow for the fully contained sample. Event rates are shown on the left side.

most background events resulting in 17 remaining events per day. These remaining events are scanned doubly by physicists using an interactive graphic event display to eliminate most of the remaining backgrounds and check the data quality. After the scanning, further scanning is done to check the scanning quality.

Event reconstructions (section 6) are performed for these events and finally, a fiducial volume cut and a minimum energy cut are applied.

5.2 First Reduction

The first reduction algorithm comprises several simple criteria to eliminate most of the background events. Criteria to select fully contained event candidates are:

(a) PE(300ns) $>$ 200 p.e.
PE(300ns) is defined as the maximum of the total number of p.e. of the inner detector in a sliding 300 nsec window.

and

(b) NHITA(800ns) $\leq$ 50 or outer trigger bit is off
NHITA(800ns) is defined as the total number of fired PMT in the outer detector in a fixed 800 nsec window.

and

(c) TIMDIF $>$ 100 μsec
TIMDIF is a time interval from the previous event.

In criterion (a), PE(300ns)=200 p.e. corresponds to lower momentum cut of 22 MeV/c for electrons and 190 MeV/c for muons. Figure 5–2 shows the typical PE(300ns) distribution for the raw data. As shown in the figure, the raw data consist of cosmic ray muons (hatched region), low energy radioactivity events (peak around 60 p.e.), and electrons from the decay of cosmic ray muons (peak around 500 p.e.). Lower peak of the hatched region is made by cosmic ray muons passing through the outer detector (PE(300ns) is calculated with inner PMTs). As explained below, the 60 p.e. peak is eliminated by the criterion (a) and the cosmic ray muons are rejected by NHITA(800ns) cut (criterion (b)). The 500 p.e. peak is rejected by the TIMDIF cut (criterion (c)).

By criterion (b), cosmic ray muons causing the outer detector activity are eliminated. Figure 5–3 shows the NHITA(800ns) distribution for (a) raw data, (b) periodical trigger events, and (c) Xe lamp events. The periodical trigger events are made by inputting trigger signals every 6 sec. We check the random coincidence using these data. Figure 5–3–(b) shows that the criterion (b) (and criterion (a) in the second reduction) are quite safe for fully contained events. Figure 5–3–(c) shows the NHITA(800ns) distribution for Xe lamp data. The light source was located at the center of the inner tank and total p.e. in each event is around 370,000 p.e. corresponding to 40 GeV. This figure shows that the light shield between the inner and the outer detector is good and the light leak from the inner to the outer detector is negligible.

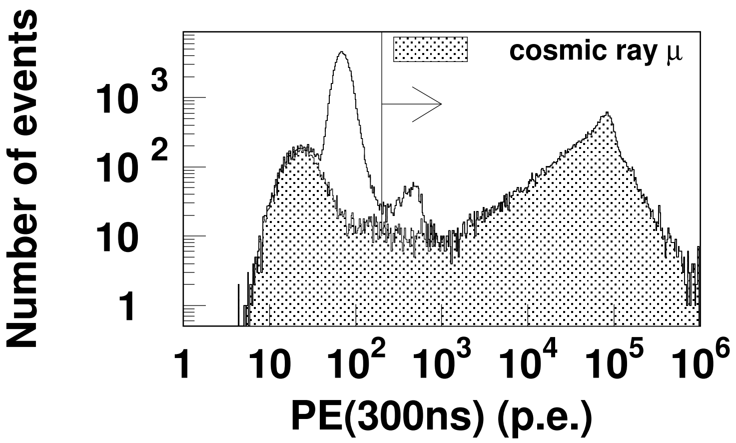

Figure 5–2: PE(300ns) distribution for raw data. All data and cosmic ray muons (hatched region) are shown. The muon sample is selected by requiring NHITA(800ns) $>$ 25 which corresponds to the rejection criterion (a) in the second reduction. The highest peak around 60 p.e. corresponds to low energy radioactivity events and another peak around 500 p.e. corresponds to electrons from the decay of cosmic ray muons. The selection criterion (a) in the first reduction is shown by arrow.

Criterion (c) eliminates the electron events from the decay of cosmic ray muons using the time difference from the preceding events (TIMDIF). This criterion also eliminates fake trigger events caused by reflection signals of PMT and "after pulsing" events following energetic events. Figure 5–4 shows the TIMDIF distribution for the raw data. Nominal value of 10^{-1} sec corresponds to the trigger rate of 10 Hz. In short TIMDIF region, peaks around 10^{-6} sec and 10^{-5} sec correspond to reflection of PMT signals and "after pulsing" respectively. Decay curve between 10^{-6} sec and 10^{-5} sec is made by decay electrons from stopping cosmic ray muons. Those unwanted events are eliminated by the TIMDIF cut (c).

Besides these criteria for fully contained events, there are separate criterion to select electrons from the muon decay.

(a') time interval from the primary fully contained event candidate is less than 30 μsec

These events are attached to the fully contained candidates as sub-events and never used as primary contained events. They are analyzed only as decay electrons following primary contained events. In the reconstruction step, further selection criteria (appendix A.5) are applied to these sub-events to select pure decay electrons.

5.3 Second Reduction

The second reduction algorithm also comprises simple criteria to reject remaining background. Criteria for selecting fully contained events are:

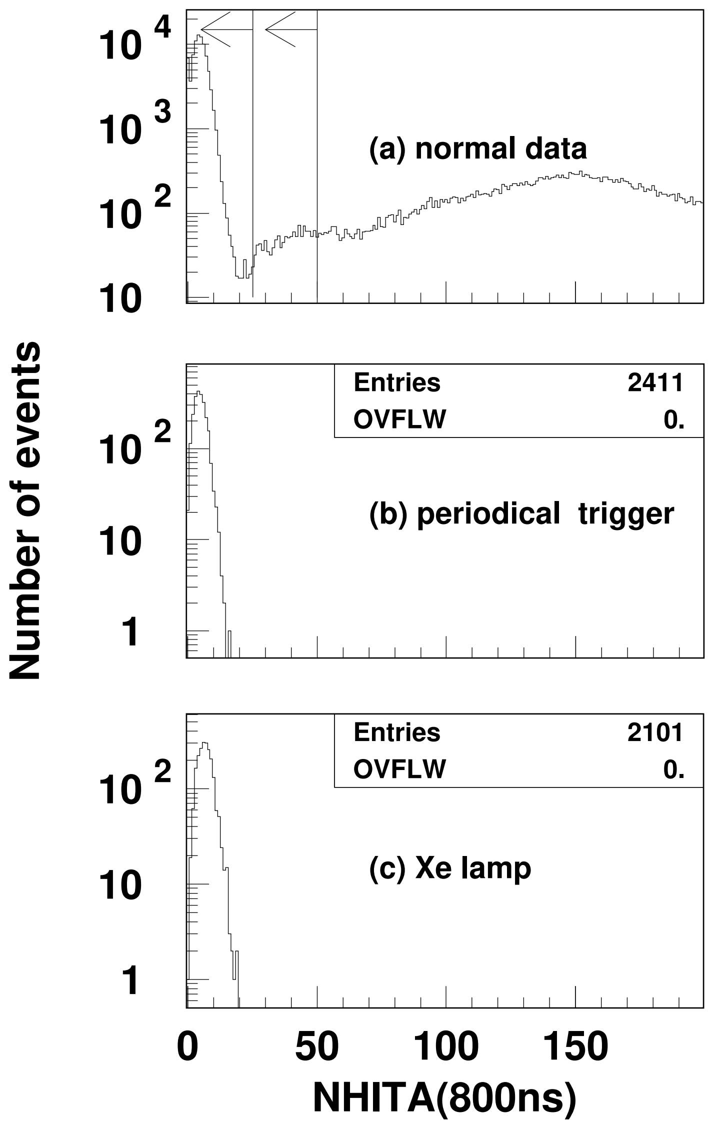

Figure 5–3: NHITA(800ns) distributions for (a) normal data, (b) periodical trigger data, and (c) Xe lamp data. The cut criteria are shown by arrows for NHITA(800ns) ≤ 50 (first reduction) and NHITA(800ns) ≤ 25 (second reduction).

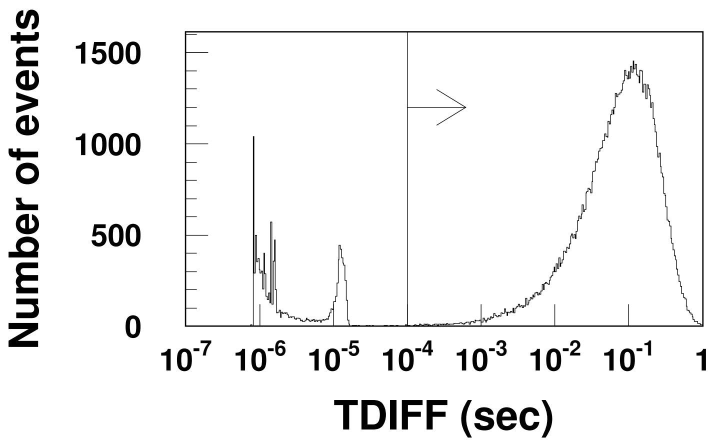

Figure 5–4: TIMDIF distribution for raw data. Events with TIMDIF $> 10^{-4}$ sec are selected by the criterion (c).

(a) NHITA(800ns) $\leq$ 25 or outer trigger bit is off or total number of p.e. in the inner detector $>$ 100,000 p.e.

and

(b) PEMAX/PE(300ns) $<$ 0.5
PEMAX is defined as maximum number of p.e.s observed by one inner PMT.

The criterion (a) is similar to the criterion (b) in the first reduction but the threshold of 25 is more stringent. However the cut is still safe as shown in Figure 5–3. This eliminates remaining cosmic ray muons. Criterion (b) rejects events in which majority of total p.e. in the inner detector is observed in a single PMT. This rejects events which occurred very close to an inner PMT or electrical noise events. Because the dynamic range of the ATM ADC is 250 p.e., this criterion is effective only for low energy events with PE(300ns) $<$ 500 p.e. corresponding to a visible energy of 55 MeV. Figure 5–5 shows the PEMAX/PE(300ns) distribution for data after the first reduction.

5.4 Third Reduction

After the first and second reductions, remaining backgrounds are mostly noise events and cosmic ray muons which have a small number of outer detector hits and pass the first and second reductions. To eliminate these backgrounds, third reduction algorithms are developed. This algorithms comprise several algorithms dedicated to specific backgrounds; cosmic ray stopping muons, through going muons, noise events called flasher, and low energy events. There are several cut conditions:

- through going muon cut.

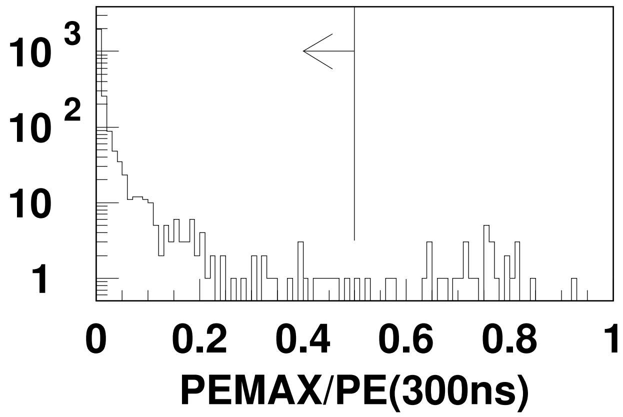

Figure 5–5: PEMAX/PE(300ns) distribution for data after the first reduction. The selection criterion (b) in the second reduction is shown by the arrow.

- stopping muon cut.
- veto counter cut.
- flasher event cut.
- low energy event cut.
- accidental coincidence event cut.

These backgrounds and cut conditions are explained in following sections.

5.4.1 Through Going Muon Cut

By the first and second reductions, most of cosmic ray muons are eliminated using the outer detector information (NHITA(800ns) cut). Therefore, remaining cosmic ray muons have only a small number of fired outer detector PMTs. To eliminate these muons keeping high efficiency of saving the fully contained events, vertex and direction of the muons are reconstructed and cut criteria using only the outer detector PMTs around the reconstructed entrance and exit points are developed. The accidental coincidence hits are reduced by restricting the outer detector PMTs used in the cuts.

Selection criteria for through going muons are:

(a) PEMAX $>$ 230 p.e.
PEMAX is defined as the maximum number of p.e. in one inner PMT

and

(b) goodness of through going muon fit $>$ 0.75

and

(c) NHITA(entrance) > 9 or NHITA(exit) > 9
NHITA(entrance) (NHITA(exit)) is defined as the number of fired outer detector PMTs in fixed 800 nsec window located within 8 m from the reconstructed entrance (exit) position.

Those which satisfy all criteria are thrown away as through going muons. PMTs near the exit point of a through going muon typically detect large photoelectron numbers, and the signals are recorded as overflowed ADC counts (saturated PMTs). The fitter for through going muons reconstructs the entrance and exit points of muons by finding the clustered earliest hit PMTs and saturated PMTs, respectively. The goodness of through going muon fitter is defined as:

$$goodness = \frac{1}{\sum_i \frac{1}{\sigma_i^2}} \times \sum_i \frac{1}{\sigma_i^2} \exp\left[-\frac{(t_i - T)^2}{2(\sigma_i \times 1.5)^2}\right] \tag{5-1}$$

where T is the entering time of the muon, t_i is TOF subtracted time of the i-th PMT, and σ_i is the time resolution of the i-th PMT. Typical goodness for a reconstructed through going muon is 0.9. Figure 5–6 shows the NHITA(entrance/exit) distribution for periodical trigger events. In the figure, entrance and exit points are randomly selected in the inner detector surface. The criteria (c) is quite safe for accidental coincidence.

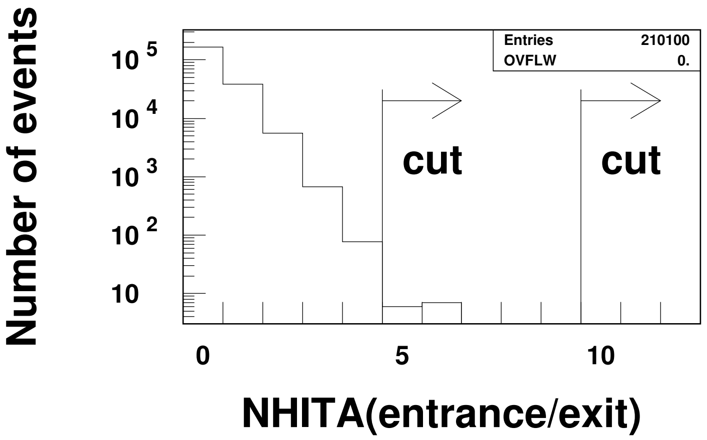

Figure 5–6: NHITA(entrance) or NHITA(exit) distribution for periodical trigger events. Cut conditions for through going muons (section 5.4.1) and stopping muons (section 5.4.2) are shown by arrows.

5.4.2 Stopping Muon Cut

Selection criteria for stopping muons are:

(a) clustered earliest hit PMTs (entrance point) is found by a stopping muon fitter

and

(b) NHITA(entrance) > 9
or
NHITA(entrance) > 4 and goodness of the stopping muon fitter > 0.5

Those which satisfy both criteria are thrown away as stopping muons. The fitter for stopping muons reconstructs the entrance of muons by finding the clustered earliest hit PMTs. The goodness is defined as Equation (5-1). Most of the fully contained events have small goodness value (< 0.5). As shown in Figure 5–6, the NHITA(entrance) > 4 cut is still safe.

5.4.3 Veto Counter Cut

After these cosmic ray muon cuts, there are still some stopping cosmic ray muons with clustered entrance points. Figure 5–7–(a) shows the X and Y vertex distribution for the events reconstructed in the upper region of the detector (Z>1760 cm).

These clustered events in the Figure 5–7–(a) are cosmic ray muons which pass through PMT cable bundles. These cable bundles cross the top part of the outer detector. It is found that these bundles shield the emitted light from muons and cause the inefficiency of the outer detector. To eliminate these muons, four plastic scintillation counters measuring 2 m $\times$ 2.5 m are placed on the top of the detector at Z = 2210 cm level as shown in Figure 5–7–(b). Since April 12th, 1997, the installed veto counters have been used in the third reduction. Event, in which one veto counter is fired and cross point of the reconstructed muon track and Z = 2210 cm plane is within 4 m from the counter position, is eliminated as muons. These muons are well eliminated as shown in Figure 5–7–(b).

5.4.4 Flasher Event Cut

After the cosmic ray muon cuts, most of the remaining backgrounds are noise events called "flasher" which are caused by a discharge from a PMT. Once the bad PMT causing flasher events is identified, high voltage power for the PMT is turned off. However there are still many "flasher" events in the data. We use characteristics of the flasher to eliminate them.

One of characteristics is that some flasher events have long tail in timing distribution as shown in Figure 5–8. To eliminate such kind of flashers, selection criteria for flasher events are defined:

(a) NHIT(minimum) ≥ 15
or
NHIT(minimum) ≥ 10 and total number of hits in the inner detector ≤ 800
NHIT(minimum) is defined as a minimum number of hits in 100 nsec width sliding window between 1200 and 1700 nsec.

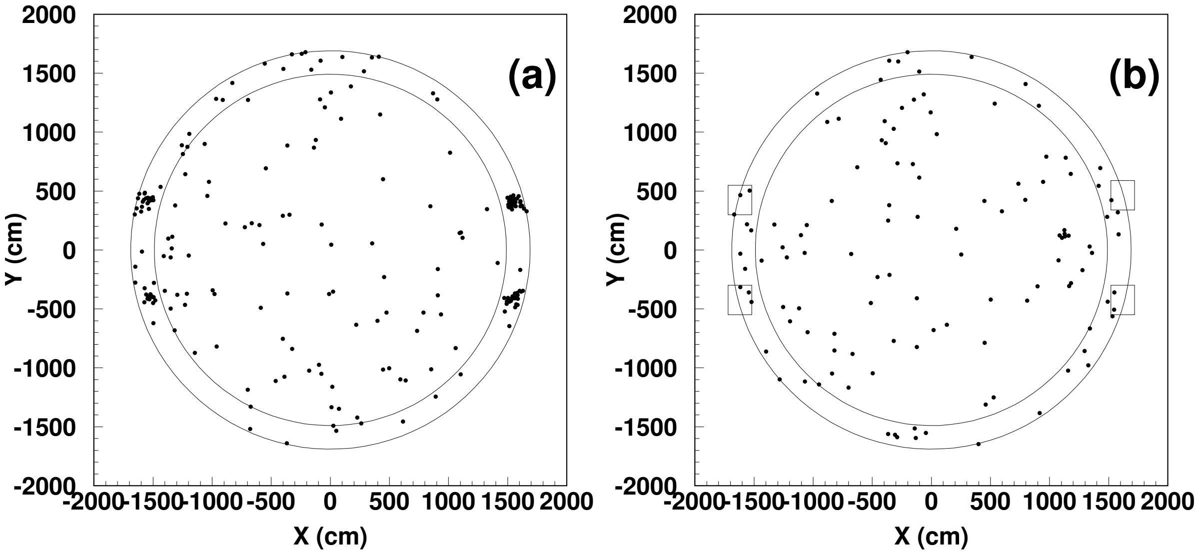

Figure 5–7: X and Y vertex distribution for the fully contained data with Z > 1760 cm. Outer circle shows the the inner detector wall and the inner circle shows the fiducial volume (2 m from the wall). In figure (a), data before April 12th, 1997 are shown and four clustered vertex are seen around cable bandles. Since April 12th, 1997, the installed scintillation counters have been used in the reduction. In figure (b), data after April 12th, 1997 are shown and the veto counter cut are applied. Four boxes show the veto counter located at Z = 2210 cm, 400 cm above the top wall of the inner detector.

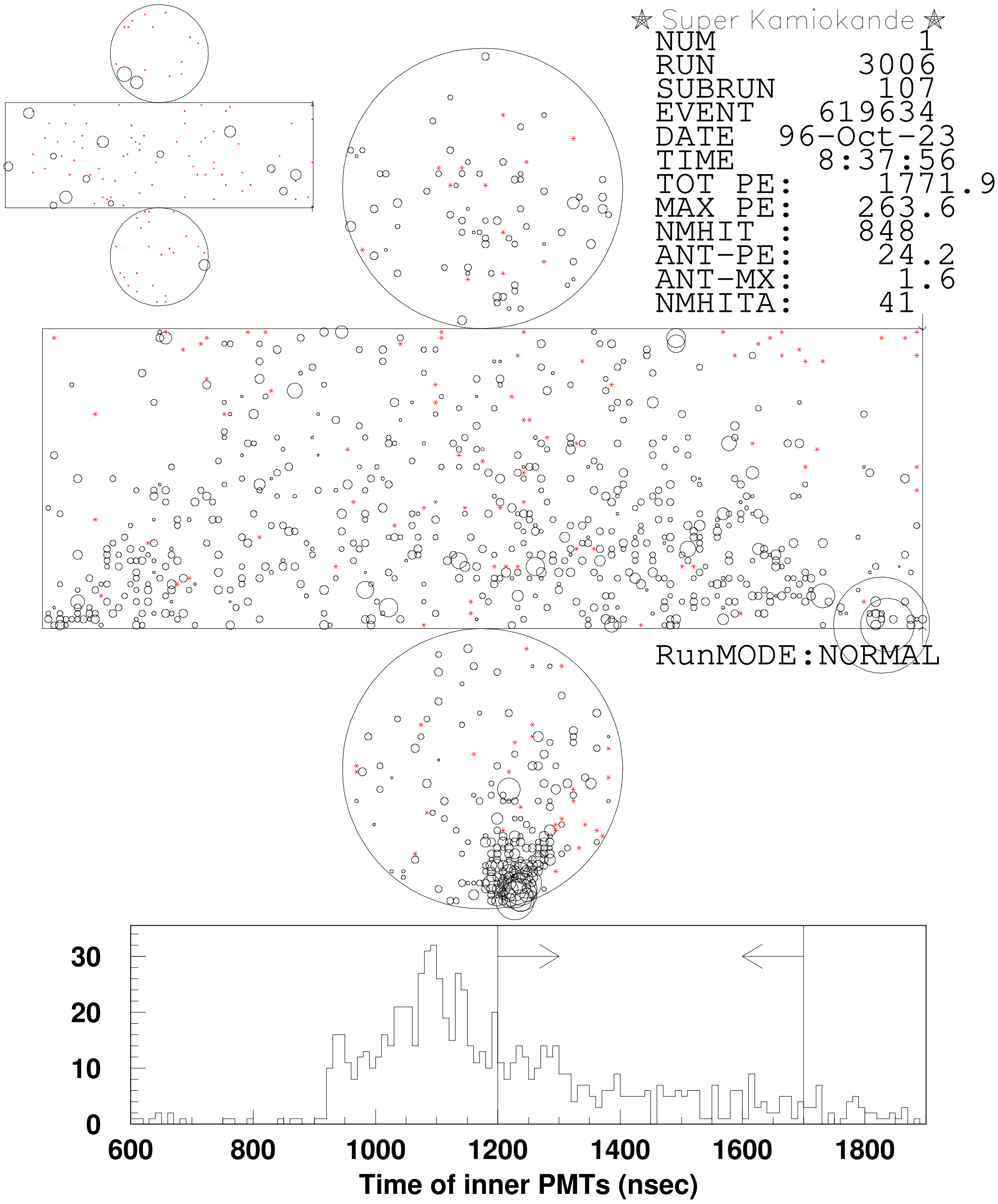

Figure 5–8: Typical flasher event which have a tail in the time distribution. The time distribution from 1200 to 1700 nsec are used to cut flasher events. Comparison should be made with Figure 5–9.

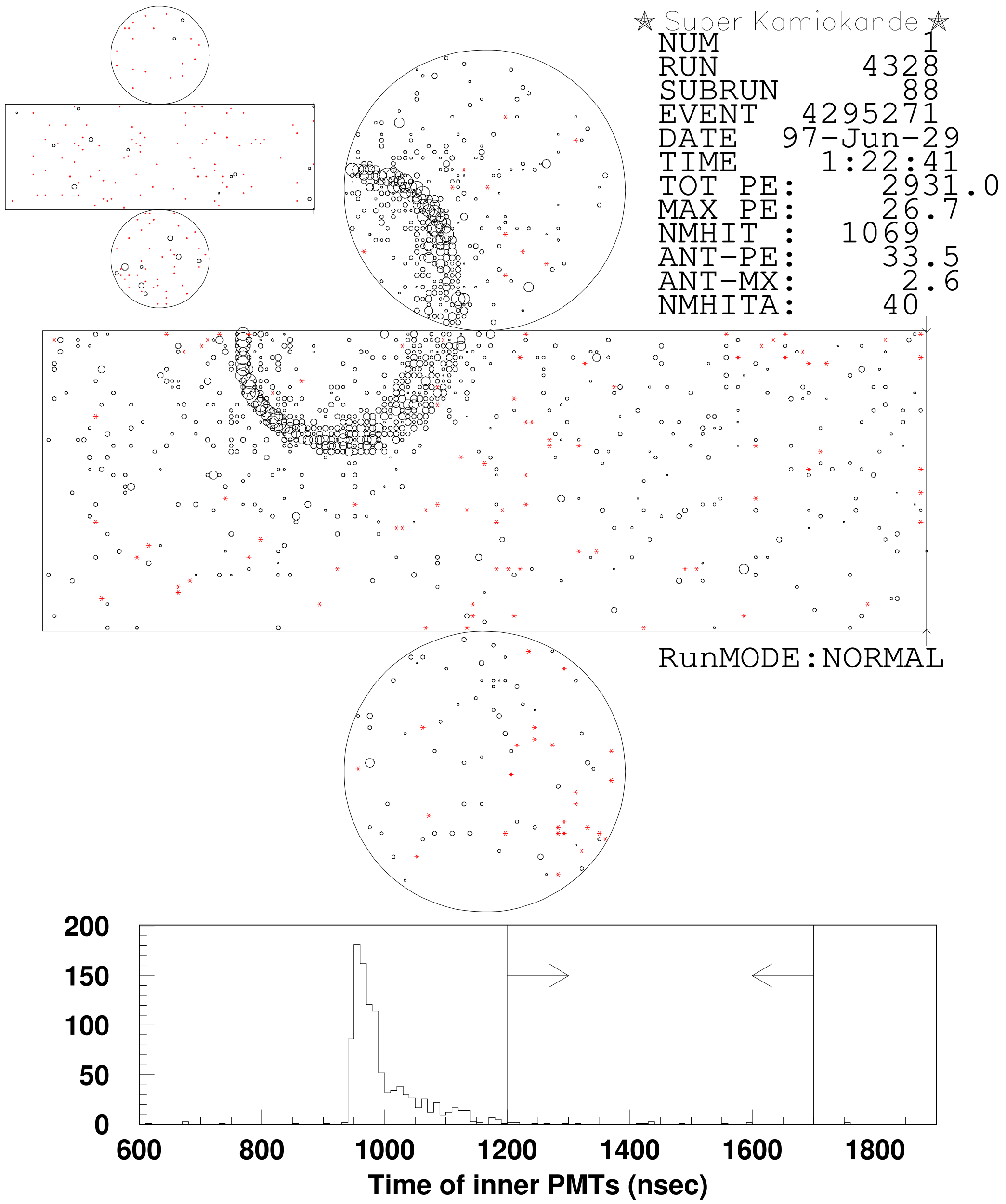

Figure 5–9: Typical fully contained event and its timing distribution. The time distribution from 1200 to 1700 nsec are used to cut flasher events. Clearly no significant tail in the time distribution is seen.

As shown in the histogram in Figure 5–9, timing window from 1200 to 1700 nsec is off timing from primary events and there are only few fired PMTs in the region for normal events. Figure 5–10 shows the NHIT(minimum) distribution for the $p \to e^+\pi^0$ Monte Carlo events. The flasher cut NHITA(minimum) $\geq$ 15 or 10 is quit safe for the $p \to e^+\pi^0$ events.

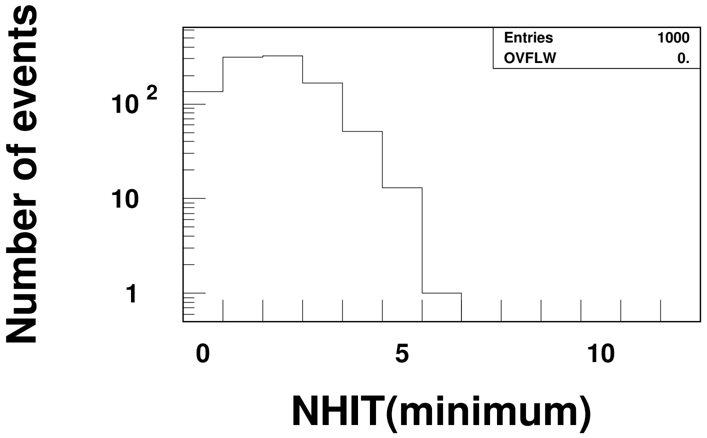

Figure 5–10: NHIT(minimum) distribution for $p \to e^+\pi^0$ Monte Carlo events. The flasher cut NHITA(minimum) $\geq$ 15 or 10 is quit safe for the $p \to e^+\pi^0$ events.

Another characteristic of flasher events is repeated event pattern corresponding to each source PMT. For this purpose, eight types of flasher patterns are characterized and compared with all data. This cut is only performed for the events with total number of fired PMTs $\leq$ 1000 which corresponds to low energy of $\sim$ 180 MeV far away from the energy regions of $p \to e^+\pi^0$ events.

In the fourth reduction, more general flasher cut using repeated event patterns is performed.

5.4.5 Low Energy Event Cut

There are still low energy events which might be caused by radioactivities in the detector or flashers. Minimum energy cut is applied to eliminate these remaining backgrounds.

(a) NHIT(50ns) $<$ 50
NHIT(50ns) is the maximum number of hit PMTs in 50 nsec timing window after subtracting TOF.

Those which satisfy the criterion are eliminated as low energy events. NHIT(50ns) $=$ 50 corresponds to about visible energy of 9 MeV.

5.4.6 Accidental Coincidence Event Cut

There are some low energy events which are followed by cosmic ray muons within the timing window of the event. These accidental coincidence events are still remained in the reduction stream because there are no on-timing outer detector activities and PE(300ns) are large due to the muons. The cut criteria to eliminate these events are defined as:

(a) NHITA(off) > 19
NHITA(off) is the number of fired PMTs in the outer detector in a fixed 500 nsec off-timing window between 1300 and 1800 nsec.

and

(b) PE(off) > 5000 p.e.
PE(off) is defined as the total number of p.e.s of the inner detector in a fixed 500 nsec off-timing window between 1300 and 1800 nsec.

Those which satisfy the both criteria are eliminated as accidental coincidence events.

5.5 Fourth Reduction

After the third reduction, most of remaining backgrounds are flasher events. The flasher events have typically many repeated, similar patterns. Therefore, in the forth reduction, repeated events are eliminated as the flasher background.

To define the estimator to compare the event pattern, detector walls are divided into about 200×200 cm square patches including 6∼9 PMTs. The total number of p.e.s in each patch is calculated (Q_i). In comparison of event A and B, the estimator of event pattern matching is defined as:

$$r = \frac{\sum_i (Q_i^A - < Q^A >)(Q_i^B - < Q^B >)}{N \sigma_{Q_A} \sigma_{Q_B}} \tag{5-2}$$

where $< Q >$ is the average of Q_i and σ_Q is the RMS deviation of Q about $< Q >$ and N is the number of patches. The r takes a value close to unity when the event pattern of A and B are very similar. If

$$r > 0.1608 \times \log_{10}((\mathrm{PETOT^A} + \mathrm{PETOT^B})/2) + 0.1299, \tag{5-3}$$

the event A satisfies the "match" condition against the event B where PETOT is the total number of p.e.s. Figure 5–11 shows the maximum r distribution with the "match" condition for (a) data after the third reduction, (b) atmospheric neutrino Monte Carlo, and (c) $p \to e^+\pi^0$ Monte Carlo.

Actually each event A is compared with other events B only when the following criterion is satisfied.

$$\left| \frac{\mathrm{PETOT^A} - \mathrm{PETOT^B}}{\sqrt{\mathrm{PETOT^A} + \mathrm{PETOT^B}}} \right| < 5. \tag{5-4}$$

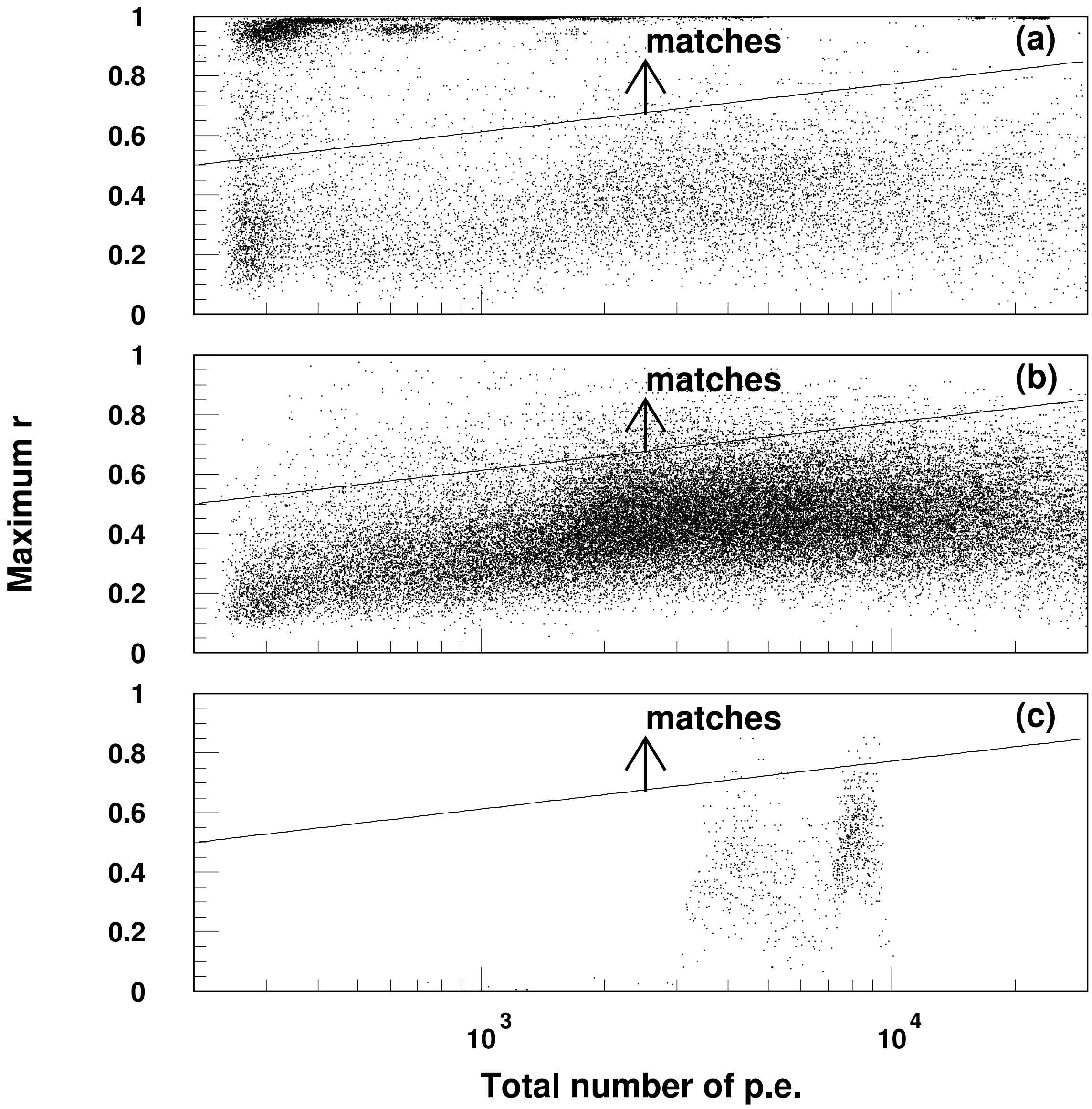

Figure 5–11: Distribution of maximum value of matching estimator r for (a) data after the third reduction, (b) atmospheric neutrino Monte Carlo, and (c) $p \to e^+\pi^0$ Monte Carlo. The "match" condition is defined as a function of total number of p.e.s. Those which have maximum $r \simeq 1.0$ in the figure (a) are flasher events.

Total number of “match” events $N^A_{\rm match}$ from the comparisons is used for discriminating the flasher events. Figure 5–12 shows the $N_{\rm match}$ distributions for (a) data, (b) atmospheric neutrino Monte Carlo, and (c) $p \rightarrow e^+\pi^0$ Monte Carlo. The threshold value for the $N_{\rm match}$ is selected as a function of the maximum value of r for each event as shown in the figure. The selection efficiency is 99.95% for the atmospheric neutrino Monte Carlo. For $p \rightarrow e^+\pi^0$ signal, no events are rejected in the fourth reduction for 1000 generated events.

5.6 Event Scanning

After these four reduction programs are applied, remaining events are scanned independently by two physicists using an interactive graphic event display. The scanners separate the fully contained events and other backgrounds. Moreover, the scanners check the data quality at the same time. If they find bad runs (or subruns), in which, for example, there are many flasher events or many PMTs are in bad condition, these runs (subruns) are assigned as bad runs (subruns) and eliminated from further analyses.

After the double scanning, further scanning is performed to check the scanning quality of the double scanning and make final decision to identify fully contained events. Since the result of event scanning is finally decided by the final scanner, scanning efficiency is checked by comparing independent scanning results by two final scanners. In a part of data (1013 events), one scanner identifies 267 events in the fiducial volume as fully contained events. On the other hand, another scanner identifies the 267 events and another event as fully contained events. Additional one event is found to have visible energy less than 30 MeV. Therefore, after minimum visible energy cut of 30 MeV, scanning efficiency is estimated to be larger than 99% for fully contained events in the fiducial volume. For $p \rightarrow e^+\pi^0$ events in the fiducial volume, the inefficiency of this reduction chains including scanning is estimated to be $< 0.1\%$ from Monte Carlo samples.

Applying the fiducial volume cut and minimum visible energy cut of 30 MeV, we obtain 4474 fully contained events. Background contaminations from cosmic ray muons, flashers, and radioactivities are negligible in the data sample. The characteristics of the fully contained events are described in section 8.1. The background contaminations are discussed again in the section 8.1.

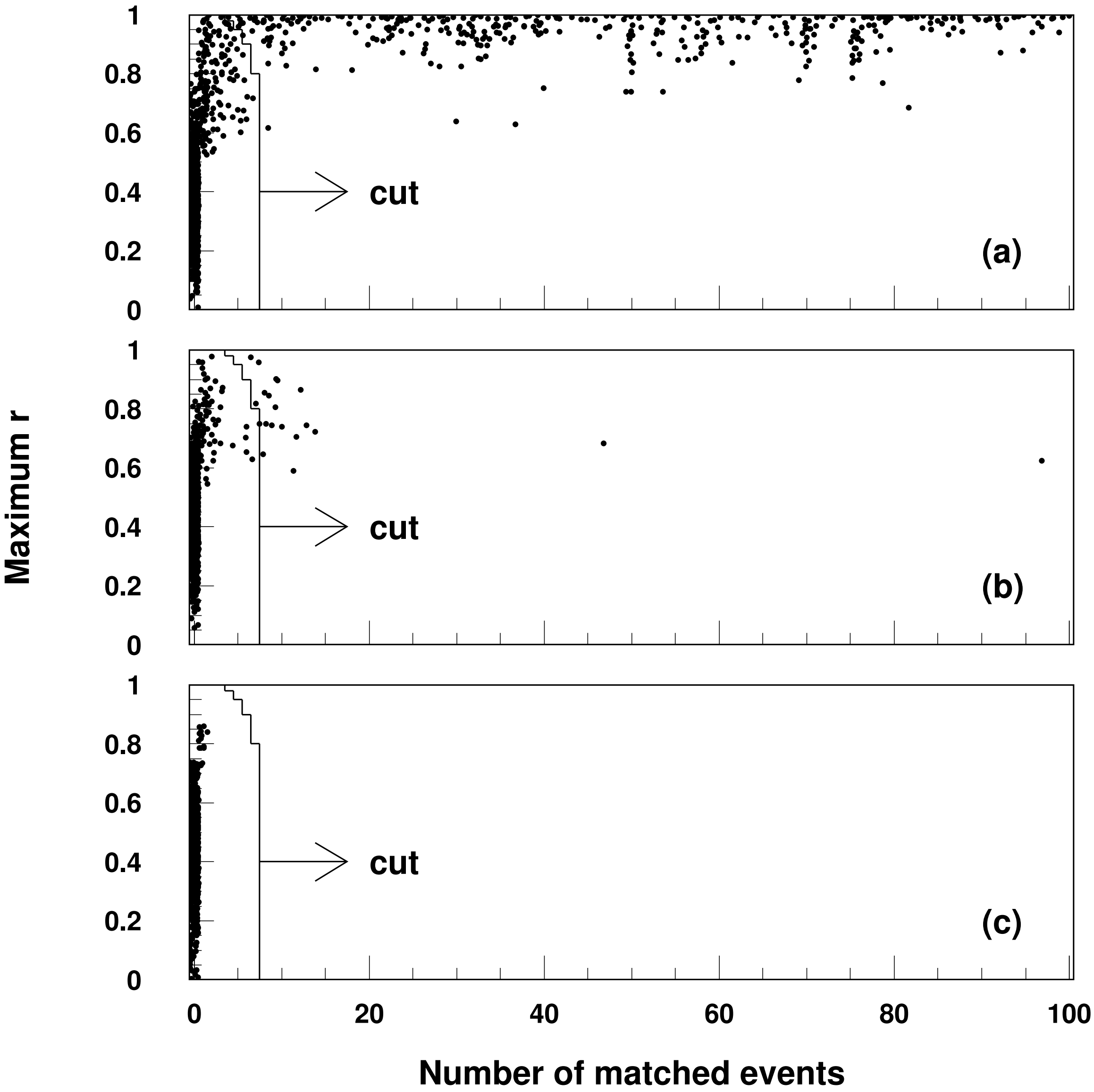

Figure 5–12: Total number of matched events and the maximum value of matching estimator r for (a) data after the third reduction and (b) atmospheric neutrino Monte Carlo and (c) $p \to e^+\pi^0$ Monte Carlo. Threshold of the number of matched events for the flasher cut is defined as a function of the maximum value of r.

6 Reconstruction

After applying reduction programs, we apply reconstruction algorithms to the fully contained event sample. Here, we get physics measurements such as vertex positions, number of rings, particle types, momentum vectors, and the number of decay electrons. The procedure of these reconstructions is

Vertex Fitter	vertex position
$\Downarrow$	
Ring Fitter	number of rings
$\Downarrow$	
Particle Identification	particle type, particle direction
$\Downarrow$	
MS Vertex Fitter	vertex position, ring direction (only for single-ring events)
$\Downarrow$	
Energy Reconstruction	particle momentum
$\Downarrow$	
Decay Electron Finding	the number of decay electrons
Ring Number Correction	correction of the number of rings

We start from the vertex fitter program to obtain the vertex position of events. With the knowledge of the vertex position, ring fitter positively identifies each ring. After that, particle identification program identifies the particle type for each ring. Here, particle direction of each ring is also reconstructed. For single-ring events, this particle type information is used to reconstruct the vertex position in "MS vertex fitter". Finally, momentum for each ring is determined and decay electrons are identified. These reconstruction algorithms are explained in the following sections (for details, see appendix A).

6.1 Vertex Fitter

The reconstruction procedure starts from the vertex fitting. The vertex position is estimated by finding the position at which the timing residual ((photon arrival time)−(time of flight)) distribution is most peaked. We take into account the track length of the particle and scattered light as well as direct (non-scattered) light to calculate the time of flight of Cherenkov photons. Because the number of rings has not yet estimated at this point, this vertex fitter searches for the vertex position with single ring assumption. Details of the algorithm are described in appendix A.1.

6.1.1 Performance of Vertex Fitter

The performance of the vertex fitter is investigated for $p \to e^+\pi^0$ events. Figure 6–1 shows the distance between the reconstructed vertex position and true (generated) position for the $p \to e^+\pi^0$ Monte Carlo events. The vertex resolution is estimated to be 18 cm. The vertex resolution for single-ring events is discussed in section 6.4.

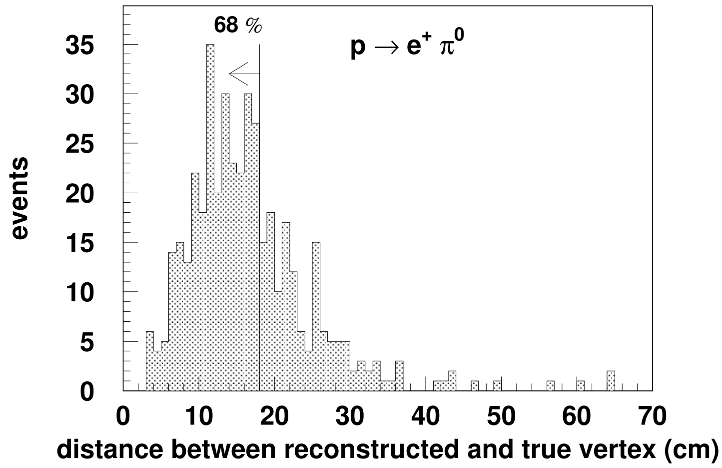

Figure 6–1: The vertex resolution for the $p \to e^+\pi^0$ events. The distances between the reconstructed vertex and true (generated) vertex are filled in the histogram. The events in which π^0 interacts in ^{16}O nucleus are not filled in the histogram. The estimated vertex resolution is 18 cm.

6.2 Ring Fitter

After reconstruction of the vertex position and one dominant ring direction, other possible rings are looked for and probable rings are reconstructed in this ring fitter. Using the reconstructed ring(s), we can reconstruct the total momentum and total invariant mass of $p \to e^+\pi^0$ events and those of atmospheric neutrino events.

Starting from one ring reconstructed by the vertex fitter, a second ring is looked for by using a known technic for a pattern recognition, Hough transformation [77]. If a probable second ring is found and regarded as a true ring, the program goes back to look for a third ring. This iteration is performed up to 4 times (fifth ring) until no more probable ring is found. Details of the algorithm are described in appendix A.2.

6.2.1 Performance of Ring Fitter

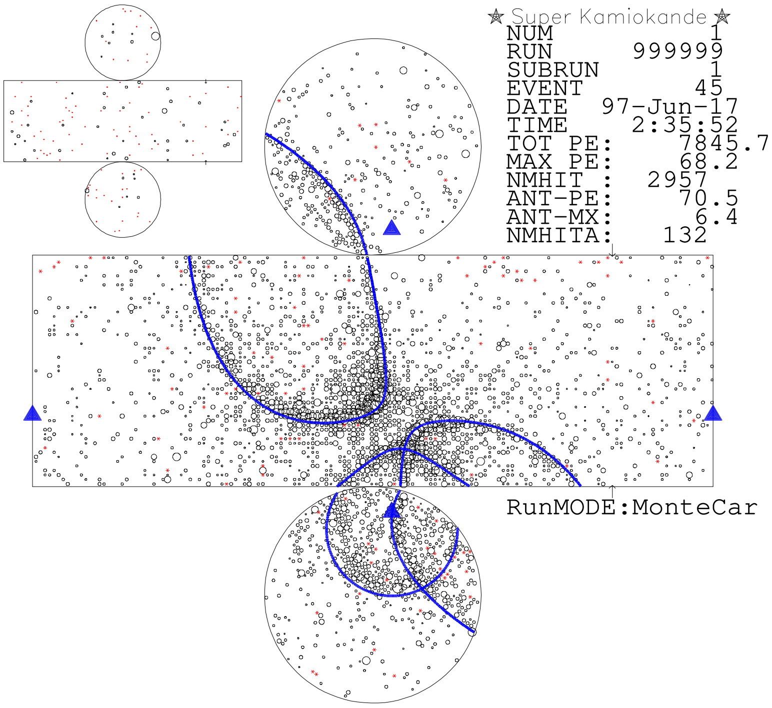

Figure 6–2: An example of the result of the ring fitting. A $p \to e^+\pi^0$ Monte Carlo event is reconstructed by the vertex fitter and the ring fitter. The reconstructed Cherenkov rings are drawn by three lines projected on the inner detector wall. The fitters fit well the positron ring (left upper one) and two gamma rings (lower two). The four triangles in the figure show the reconstructed vertex position. The left and right triangles indicate the height of the vertex and other two indicate azimuthal angle coordinate of the vertex.

An example of the result of the ring fitting is shown in Figure 6–2. In the $p \to e^+\pi^0$ event, the positron ring (left upper one) is well fitted by the vertex fitter and remaining two gamma rings are also well reconstructed by the ring fitter. The distribution of the number of reconstructed rings for the $p \to e^+\pi^0$ event sample is presented in section 9.1.

The performance of the ring fitter for single-ring events is also studied. Figure 6–3 shows the efficiency of single-ring identification for quasi-elastic scattering events. The efficiency is $\sim 96\%$ for the momentum region of $p < 1.33$ GeV/c.

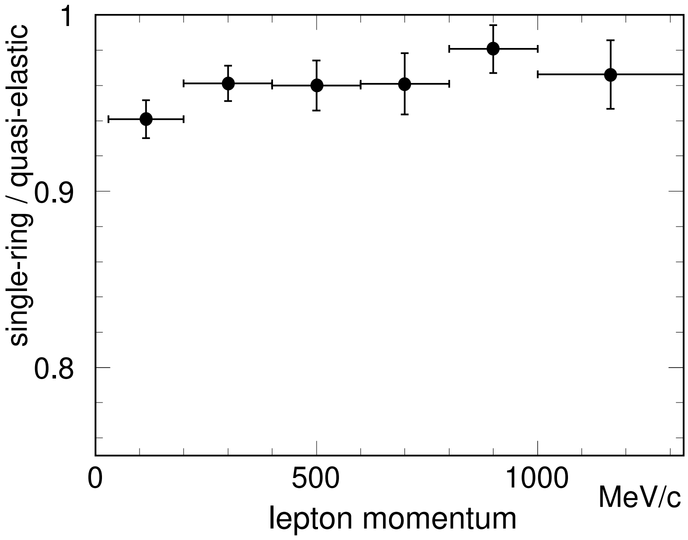

Figure 6–3: The efficiency of single-ring identification for quasi-elastic scattering events. Using atmospheric neutrino Monte Carlo, the fraction of (single-ring quasi-elastic events)/(quasi-elastic events) is plotted as a function of momentum. The efficiency is $\sim 96\%$ for the momentum region.

6.3 Particle Identification

The program "particle identification" determines the particle type of each ring using its Cherenkov ring pattern and opening angle. Each ring is classified as a showering particle ($e^{\pm}, \gamma$) or a nonshowering particle ($\mu^{\pm}, \pi^{\pm}$). The showering (nonshowering) particles are sometimes called e-like (μ-like). To identify the particle type, we start from "ring separation" (appendix A.4.1) to get the observed p.e. distribution given by each ring. The examples of the separated p.e. distributions are shown in Figure A–10 and A–11 for the $p \to e^+\pi^0$ event. After the ring separation, the observed p.e.s are compared with expected p.e. distributions of an electron particle and a muon particle. One of two particle types which better reproduces the observed p.e. distribution is selected as a reconstructed particle type. Details of the algorithm are described in appendix A.3.

6.3.1 Performance of Particle Identification

To check the performance of our particle identification, we use atmospheric neutrino Monte Carlo events. Figure 6–4 shows the particle identification results for the atmospheric neutrino Monte Carlo events and data. In the figures, particle identification parameters $P = (\sqrt{-\log P_1(\mu)} - \sqrt{-\log P_1(e)})$ are filled for single ring events with the visible energy below 1.33 GeV. Here, $P_1(e)$ and $P_1(\mu)$ are estimated probabilities for an electron assumption and a muon assumption, respectively. If $P > 0$ ($P < 0$), the ring is identified as showering (nonshowering) type. Ignoring the relative normalization difference between e-like and μ-like events, the parameter distributions agree well between data and Monte Carlo. From the Monte Carlo sample, misidentification probabilities are estimated to be $0.5 \pm 0.1\%$ for CC QE events of ν_e and $0.7 \pm 0.1\%$ for CC QE events of ν_μ. Also, the particle identification program was checked using a 1 kton water Cherenkov detector with e and μ beams from the 12 GeV proton synchrotron at KEK [78].

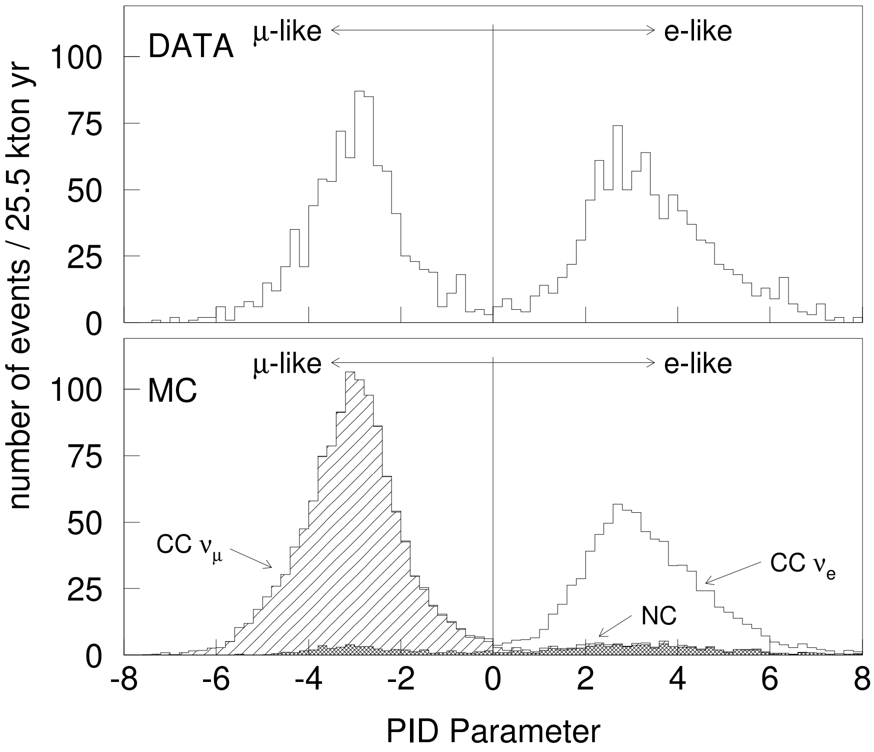

Figure 6–4: Particle identification parameter distributions for data and atmospheric neutrino Monte Carlo. Single ring events with the visible energy below 1.33 GeV are filled in the figures. Positive (negative) parameters correspond to e-like (μ-like) events.

Moreover, cosmic ray stopping muon data and their decay electrons are used for investigating the particle identification performance. Figure 6–5 shows the particle identification parameters for the stopping muons and their decay electrons in each divided exposure period. These distributions are stable and also agree well with Monte Carlo. From the data, the misidentification probabilities for stopping muons and decay electrons are $0.4 \pm 0.1\%$

and 1.8 ± 0. ... robabil-
ity are $0.1^{+(}_{-(}$ ... with the
atmospheric ... y higher
energy of th ... electrons
is a little wc

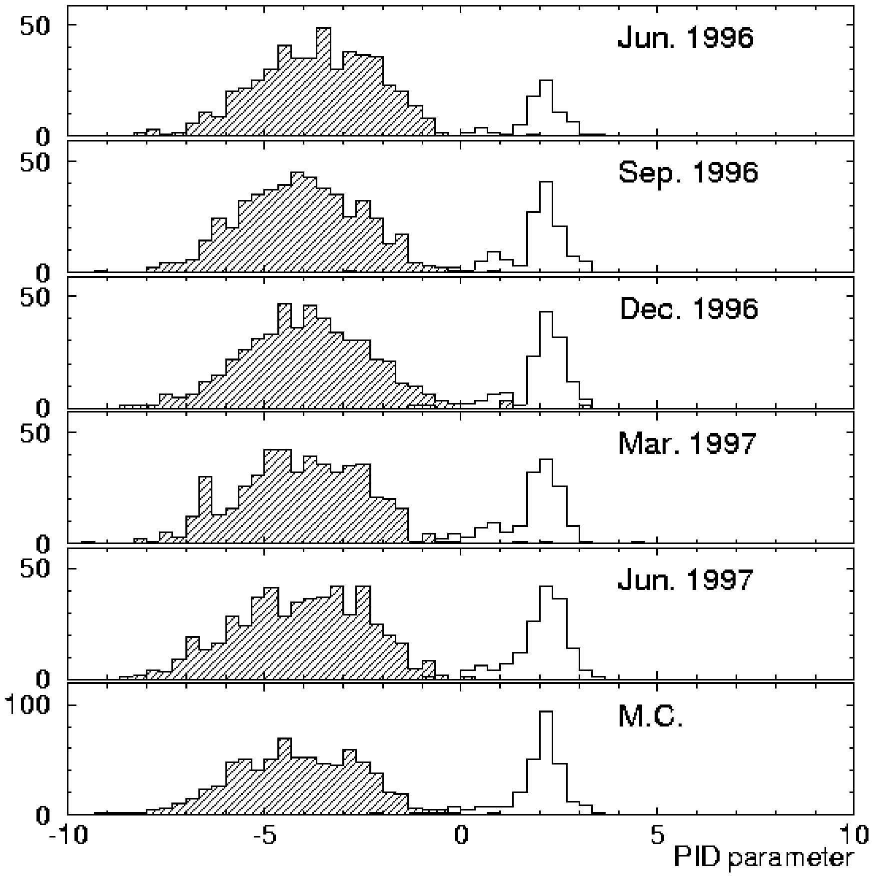

Figure 6–5: Particle identification parameter distributions for cosmic ray stopping muons (shaded histograms) and their decay electrons (blank histograms). The bottom figure shows Monte Carlo simulation.

In these investigations, we use only single ring events. However, the misidentification probability differs between single ring and multi ring events due to overlapping rings. Using a $p \to e^+\pi^0$ Monte Carlo sample the multi-ring misidentification is estimated to be 2% as is shown in Figure 9–3.

6.4 MS Vertex Fitter

The vertex position of multi-ring events are determined by the vertex fitter explained in section 6.1 which uses mainly timing information to reconstruct the vertex position. On the other hand, the vertex position of single-ring events, which is also reconstructed by the vertex fitter, is improved by the MS vertex fitter. This vertex fitter uses the Cherenkov ring pattern information in addition to the timing information and improves the vertex resolution in the longitudinal direction. The ring direction is also reconstructed again in the fitting.

MS vertex fitter uses the expected p.e. distribution like the particle identification. However, the Cherenkov opening angle, which is treated as a variable parameter and optimized in the particle identification (appendix A.3), is fixed in MS vertex fitter. In calculating the expectation, a particle type which is determined by the particle identification and an estimated momentum are used. The fitter selects a vertex position where expected p.e. distribution most reproduces the observed distribution.

6.4.1 Performance of MS Vertex Fitter

Figure 6–6 shows the vertex resolution along the particle direction ($\Delta \mathrm{pos}_{//}$) for MS fitter (MS-fit) compared with that for the initial vertex fitter (TDC-fit). Clearly, the vertex resolution is improved by MS fitter.

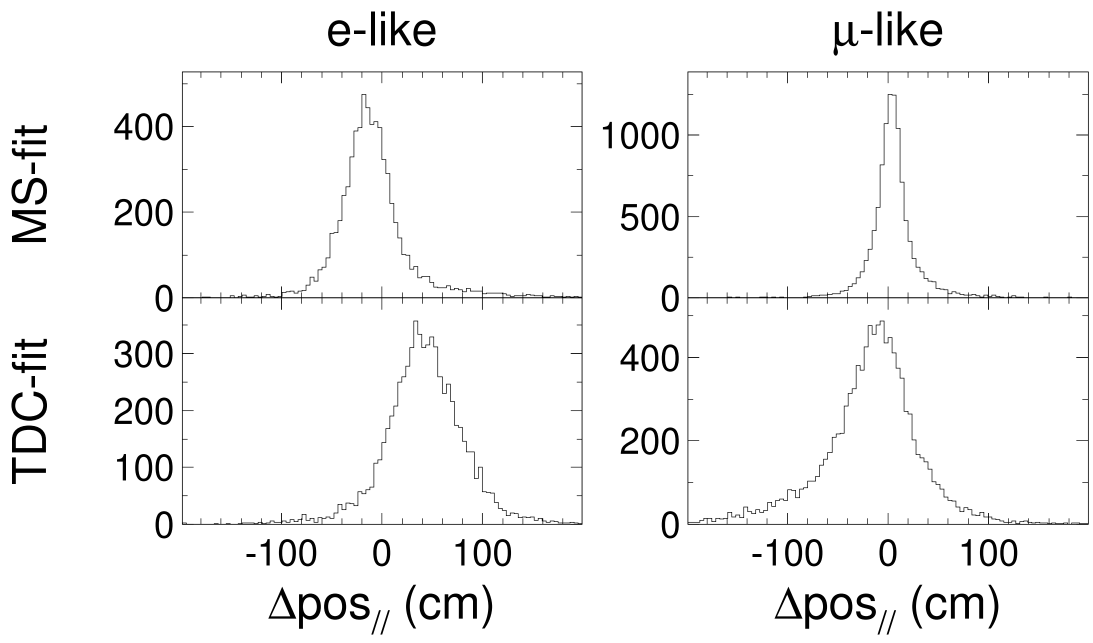

Figure 6–6: The vertex resolution along the particle direction for MS vertex fitter (MS-fit) and initial vertex fitter (TDC-fit). Single ring events in atmospheric neutrino Monte Carlo sample are used. The vertex resolutions are significantly improved by MS fitter.

The improved vertex resolution and angular resolution are shown in Figure 6–7 and 6–8, respectively. These resolutions are estimated from atmospheric neutrino Monte Carlo sample with the visible energy below 1.33 GeV. The vertex resolution is 34 cm for e-like and 25 cm for μ-like events. The angular resolution is estimated to be 3.2° for e-like and 1.9° for μ-like events.

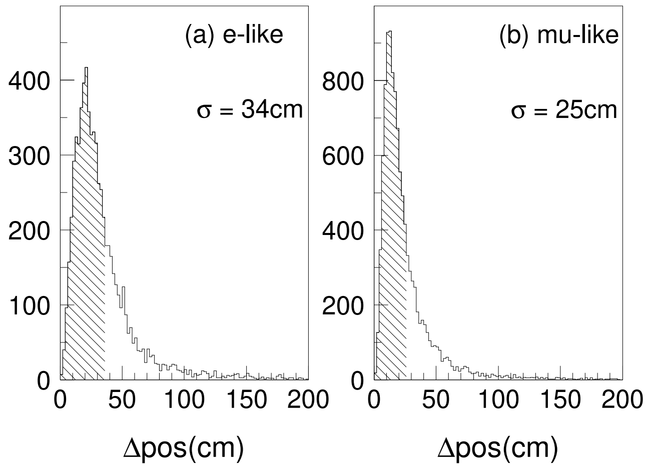

Figure 6–7: The vertex resolution after MS vertex fitter for (a) e-like single ring events and (b) μ-like single ring events estimated from atmospheric neutrino Monte Carlo sample. Distances between true vertex positions and reconstructed vertex positions (Δpos) are filled in the figures. Hatched regions show 68% of the total events. The vertex resolution is 34 cm for e-like and 25 cm for μ-like events.

6.5 Momentum Reconstruction

The momentum is estimated from the total number of p.e.s detected within a 70° half opening angle towards the reconstructed ring direction. For single ring events, observed p.e.s in each PMT q_i (i refers to a PMT number) are used. On the other hand, for multi ring events, observed p.e.s given by each ring $q_{i,n}$ (n refers to a ring number) are used for each ring momentum. The separated p.e.s $q_{i,n}$ are calculated from q_i by "ring separation" described in appendix A.4.2. The number of observed p.e.s is corrected for light attenuation in water, PMT angular acceptance, and PMT coverage.

$$RTOT_n = constant \times \frac{G}{G^{\mathrm{MC}}} \times \sum_{\theta_{i,n}<70^\circ} q_{i,n} \times \exp(\frac{r_{i,n}}{L}) \times \frac{1}{f(\Theta_{i,n}^{\mathrm{PMT}})} \times \cos\Theta_{i,n}^{\mathrm{PMT}} \qquad (6\text{-}1)$$

where

G	PMT gain parameter for the event sample which is deduced from cosmic ray muon sample (see section 3.3.5). For momentum reconstruction of data and Monte Carlo, G^{data} (deduced from through going muons of data) and G^{MC} (deduced from through going muons of Monte Carlo) are used, respectively.
$\theta_{i,n}$	opening angle of the i-th PMT towards the n-th ring direction.

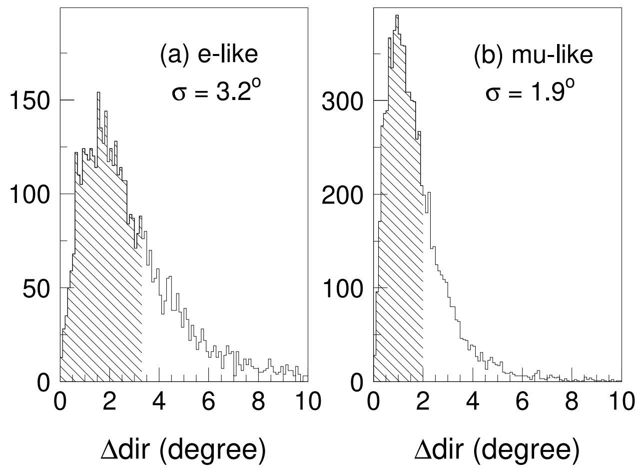

Figure 6–8: The angular resolution after MS vertex fitter for (a) e-like single ring events and (b) μ-like single ring events estimated from atmospheric neutrino Monte Carlo sample. Opening angles between true lepton directions and reconstructed directions (Δdir) are filled in the figures. Hatched regions show 68% of the total events. The angular resolution is 3.2° for e-like and 1.9° for μ-like events.

$q_{i,n}$ fractional p.e.s of the i-th PMT due to the n-th ring calculated by the ring separation (appendix A.4.2). For single ring events, $q_{i,n} = q_i$.

$r_{i,n}$ travel length of emitted Cherenkov photons for the i-th PMT.

L attenuation length for the event sample (see section 3.3.5). For momentum reconstruction of data and Monte Carlo, L^{data} (deduced from through going muons of data) and L^{MC} (deduced from through going muons of Monte Carlo) are used, respectively.

$f(\Theta_{i,n}^{\mathrm{PMT}})$ effective cross section of a PMT as a function of the incident angle $\Theta_{i,n}$ (Figure 6–9).

The ratio of gain parameters corrects for the PMT gain difference between data and Monte Carlo. This term also corrects for the time variation of the PMT gain observed in the Super–Kamiokande detector (Figure 7–14). In the summation, there are correction terms for attenuation length, PMT angular acceptance, and PMT coverage. To reject the effect of possible decay electrons following the primary events, we only use observed p.e.s whose timing information is within -50 to $+250$ nsec timing window from the peak of the timing residual. This corrected number of p.e.s $RTOT_n$ is converted to the particle momentum assuming the particle is an electron for e-like ring and a muon for μ-like ring. Figure 6–10 shows the relation between $RTOT$ and the momentum for electrons and muons. Due to nonnegligible muon mass, the relation for muons deviates from a linear line.

6.5.1 Performance of Momentum Reconstruction

Figure 6–11 shows the momentum resolution for single ring electrons and muons. For single ring events, the reconstructed momentum resolution is estimated to be $\pm(2.5/\sqrt{P(\mathrm{GeV})}+$

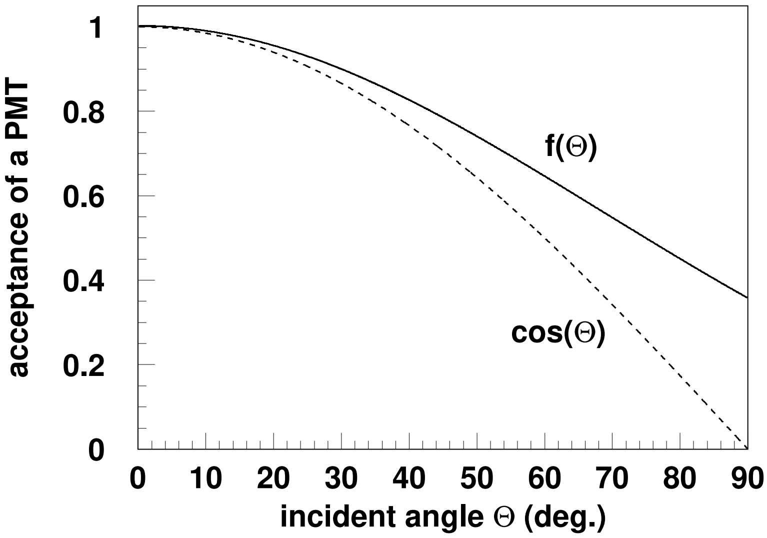

Figure 6–9: The effective cross section of the PMT as a function of incident angle Θ. The vertical direction corresponds to $\Theta = 0$.

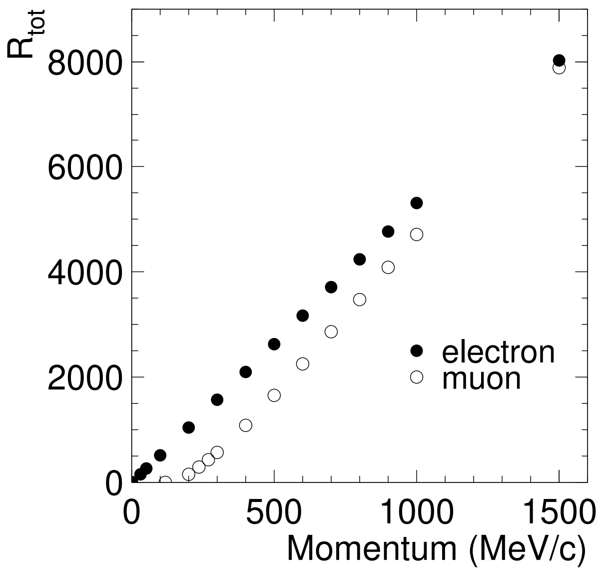

Figure 6–10: The relation between $RTOT$ and the momentum for electrons and muons.

0.5)% for electrons and $\sim \pm 3\%$ for muons. However, the momentum resolution for multi

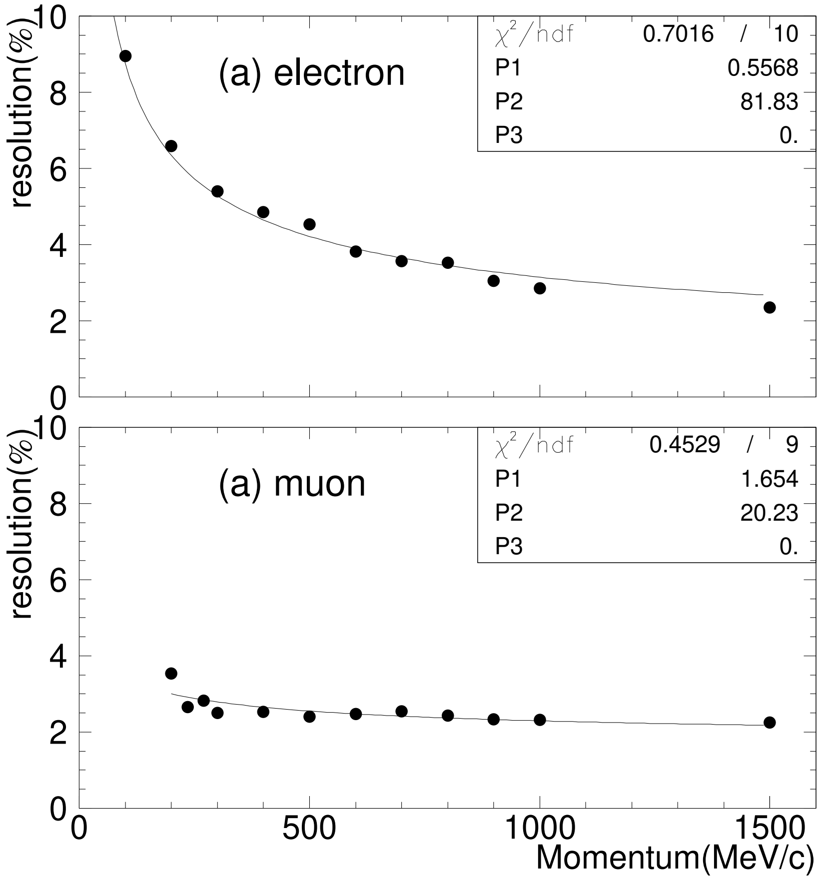

Figure 6–11: The momentum resolution for single ring electrons and muons. The reconstructed momentum resolution is estimated to be $\pm(2.5/\sqrt{P(\mathrm{GeV})} + 0.5)\%$ for electrons and $\sim \pm 3\%$ for muons.

ring events is different from that for single ring events due to ring overlapping. Using the $p \to e^+\pi^0$ Monte Carlo events, the momentum resolution is estimated as shown in Figure 6–12. The resolution for positrons and gammas are 6% and 14%, respectively. The averaged resolution is $\pm 10\%$ for each ring in the $p \to e^+\pi^0$ events.

The calibration of the absolute energy scale is important and described in section 7.

6.6 Decay Electron Finding

We identify decay electrons following the primary events to reject atmospheric neutrino background but accept proton decay signal. The energy spectra of decay electrons are shown

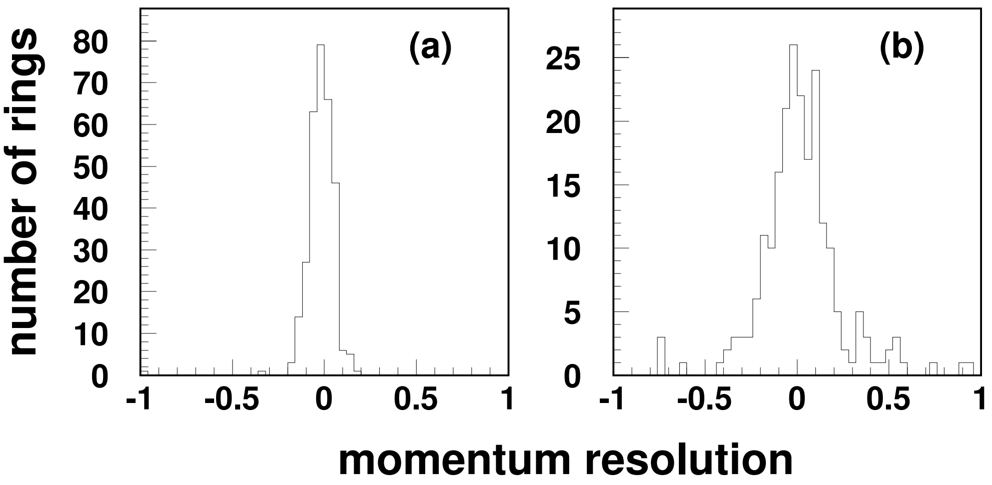

Figure 6–12: The momentum resolution for $p \to e^+\pi^0$ events. The fractional momentum differences are filled for (a) positron rings and (b) gamma rings. The resolution for positrons and gammas are 6% and 14%, respectively.

in Figure 7–8 and the mean energy is 37 MeV. Since the trigger threshold corresponds to 5.7 MeV electrons, most of decay electrons can be detected. Details of the decay electron finding are described in appendix A.5.

To study the background contamination for muon decay detection, we collect about 32000 cosmic ray stopping muons with total p.e.s below 10000 p.e. ($\sim$ 1.5 GeV/c). No event has more than one decay and therefore the contamination level is less than 10^{-4}.

The analysis efficiency for detection of decay electrons is estimated to be 80% for μ^+ and 63% for μ^- by a Monte Carlo study. The difference in these efficiencies is due to μ^- capture on ^{16}O. This efficiency was confirmed to an accuracy of 1.5% using stopping cosmic ray muons.

6.7 Ring Number Correction

Finally, ring number correction is performed. In this step, final ring momenta are checked and in case of very low momentum, the ring is rejected as a fake ring. The rejection criteria are defined as following.

(1a) $E_A < E_B$
E_A and E_B are visible energy of ring-A and ring-B, respectively.

(1b) $\theta_{A-B} < 30°$
θ_{A-B} is the opening angle between ring-A and ring-B directions.

(1c) $E_A \cos\theta_{A-B} < 60$ MeV

(2a) $E_A/\Sigma_i E_i < 0.05$
The fractional visible energy of ring-A is smaller than 0.05.

(2b) $E_A < 40$ MeV

If the conditions 1a$\cap$1b$\cap$1c are satisfied and/or 2a$\cap$2b are satisfied, the ring-A is discarded as a fake ring. This ring number correction is performed only for more than 2 ring events.

7 Energy Calibration

The energy scale of the Super–Kamiokande detector is checked using several calibration sources. The cosmic ray muons stopping in the detector are major calibration sources ranging from ~200 MeV/c to few GeV/c. Another source is neutrino-induced π^0 events which is used by calibrating the invariant mass. These π^0s are unique multi-ring sources which is important for the $p \to e^+\pi^0$ search. There are also electrons from stopping cosmic ray muons and a linear accelerator. In section 7.1, the method and results of these calibration are described. The results of scale calibrations are summarized in section 7.1.6. In section 7.2, the time variation of the energy scale are studied. Finally, uniformity of the energy scale in the detector are discussed.

7.1 Absolute Energy Scale Calibration

7.1.1 Cosmic Ray Stopping Muons - I

Stopping cosmic ray muons decay to electrons and many of these electrons are observed as separate events. Reconstructing the vertex positions of both the muons and the decay electrons, one can measure muon ranges in the detector. Because this range is an independent measurement of muon energy, one can utilize it for calibrating the energy scale derived from the number of p.e.'s (section 6.5) which is used in proton decay analysis. Figure 7–1 shows the schematic view of this calibration method.

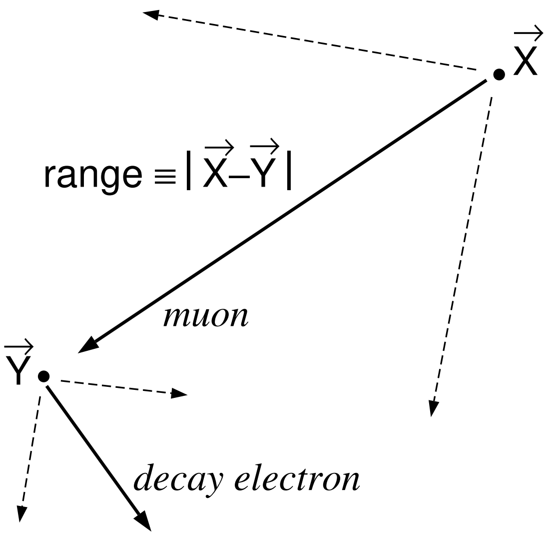

Figure 7–1: Schematic view of energy scale calibration using muon range. The muon traverses the detector (solid line arrow) emitting Cherenkov light (dashed line arrow) and stops and decays to the electron. Using muon vertex $\vec{X}$ and decay electron vertex $\vec{Y}$, range could be defined as $|\vec{X} - \vec{Y}|$.

Criteria for selecting cosmic ray muons for the calibration are:

(a) 200 p.e. $<$ total p.e..

(b) one cluster of hit PMTs in the outer detector.

(c) entrance point is on top wall, $\cos\theta_z > 0.94$.

(d) one decay electron with time difference > 0.8 μsec.

(e) range > 7 m.

Criterion (a) corresponds to 190 MeV/c muon momentum. Criterion (b) requires an entrance point of a muon in the outer detector. In criterion (c), $\cos\theta_z$ is the zenith angle of a muon and vertically down-going muons are selected. Criterion (d) surely selects muon events and time difference > 0.8 μsec ensures not to affect energy and track reconstruction of the muon events. By reconstructing muon vertex $\vec{X}$ and decay electron vertex $\vec{Y}$, a range of the muon could be defined as $|\vec{X} - \vec{Y}|$. Resolutions of both the muon vertex and the decay electron vertex are better than 50 cm. In Figure 7–2, horizontal axis shows the muon range $|\vec{X} - \vec{Y}|$ and vertical axis shows $p_\mu/|\vec{X} - \vec{Y}|$ where p_μ is the reconstructed muon momentum from the number of p.e.'s. Figure 7–2–(a) and (b) show the distributions for the real data and Monte Carlo events, respectively. These Monte Carlo events are generated using the reconstructed vertex and momentum vectors of the muon data. Only flat distribution regions of the range > 7 m are used in the calibration (criterion (e)).

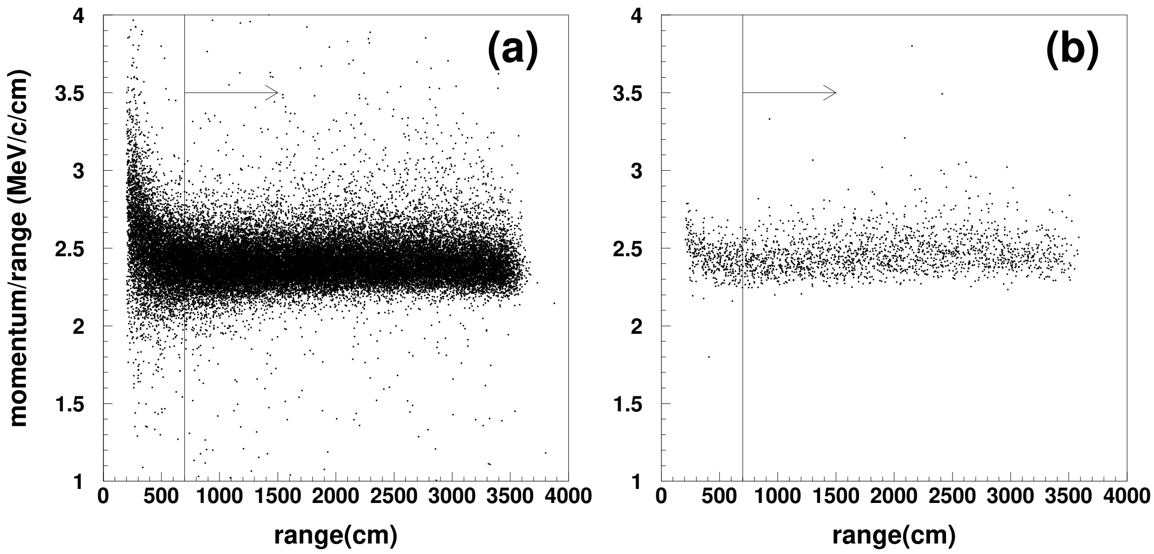

Figure 7–2: Range v.s. momentum/range distribution for stopping cosmic ray muons. Both (a) data and (b) Monte Carlo are shown. Only muons with range > 7 m are used in the calibration.

For comparison of the data and the Monte Carlo, both samples are divided by the 5 m step of the range from 10 m to 35 m and one 3 m step of the range from 7 m to 10 m, resulting 6 bins. Figure 7–3 shows the averaged $p_\mu/|\vec{X} - \vec{Y}|$ in each range bin for the data and the Monte Carlo. They agree within 2.5% level.

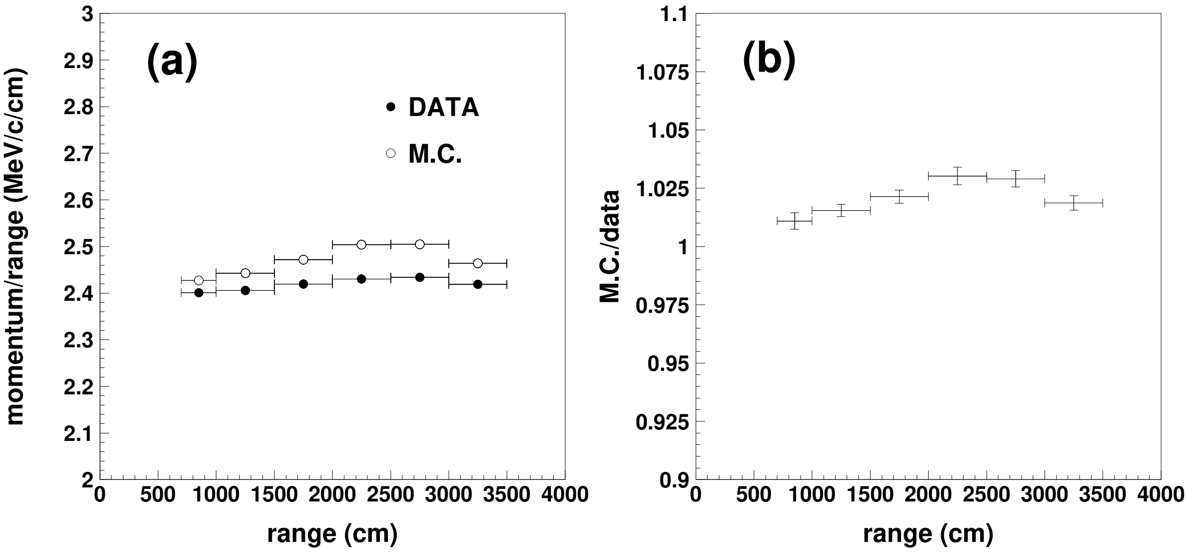

Figure 7–3: Range v.s. averaged momentum/range for data and Monte Carlo. Figure (a) shows the averaged momentum/range in each range bins for data (filled circles) and Monte Carlo (empty circles). For comparison of the data and the Monte Carlo, both samples are divided by the 5 m step of the range from 10 m to 35 m and one 3 m step of the range from 7 m to 10 m, resulting 6 bins. Figure (b) shows ratios of Monte Carlo to data. From the comparison of the data and the Monte Carlo, the energy scale of data agrees with Monte Carlo within 2.5% level.

7.1.2 Cosmic Ray Stopping Muons - II

Another calibration method using stopping cosmic ray muons is to utilize half opening angle of Cherenkov ring. The opening angle θ of Cerenkov ring has dependence on the particle velocity $\beta(= v/c)$ as $\cos\theta = 1/n\beta$. Because $|d\theta/dp_\mu|$ is large at low momentum p_μ region, this calibration method is possible in the low momentum region of $p_\mu \lesssim 500$ MeV/c. Therefore this calibration method is supplemental with the method using muon range (section 7.1.1).

Criteria for selecting cosmic ray muons for this calibration are:

(a) $200 <$ total p.e. < 1500.

(b) one cluster of hit PMTs in the outer detector.

(c) entrance point is on top wall, $R < 14.9$ m, $\cos\theta_z > 0.9$.

(d) one decay electron with time difference > 0.8 μsec.

Criterion (a) roughly corresponds to the muon momentum of 190 MeV/c to 380 MeV/c. Criterion (b) requires an entrance point of a muon in the outer detector. Criterion (d) surely selects muon events and also prevents decay electrons from affecting energy and track reconstructions of the muon events. Cherenkov opening angle for each event is reconstructed in particle identification algorithm (section A.3).

Figure 7–4 shows the reconstructed Cherenkov opening angle and reconstructed muon momentum $p_{p.e.}$ distributions for data and Monte Carlo. These Monte Carlo events are generated using reconstructed vertex and momentum vectors of muon data. The momentum dependence of the Cherenkov opening angle is seen both in the data and the Monte Carlo. In Figure 7–5, the opening angle is transformed to expected muon momentum p_θ by the relation $\cos\theta = 1/n\beta = \sqrt{1 + m^2/p_\theta^2}/n$.

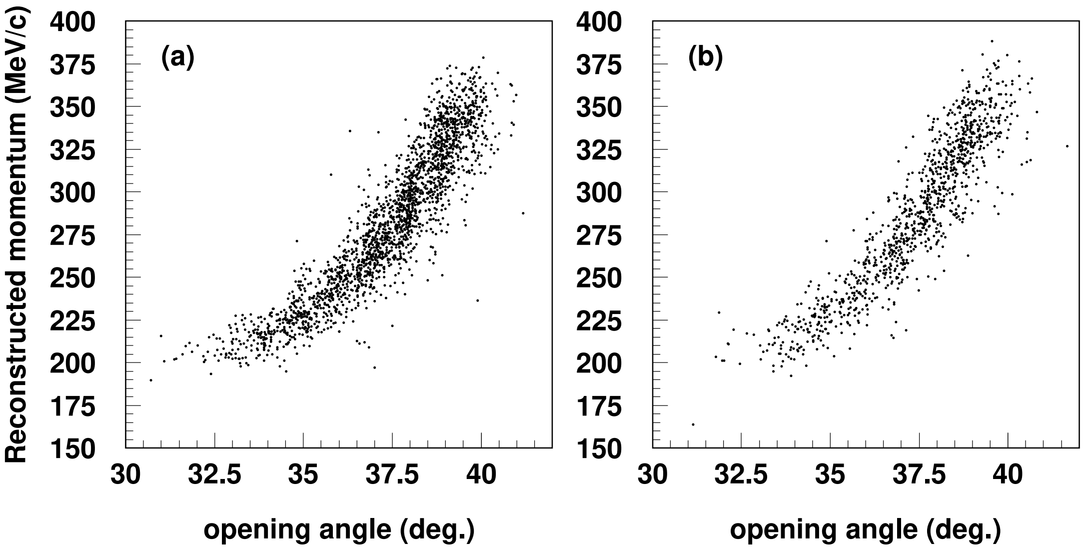

Figure 7–4: Reconstructed Cherenkov angle and reconstructed momentum distributions for stopping cosmic ray muons. Both (a) data and (b) Monte Carlo show clear momentum dependence of the Cherenkov opening angle.

Because there are good agreements between $p_{p.e.}$ and p_θ in Figure 7–5, we can compare energy scale of the data with that of the Monte Carlo by comparing ratios of $p_{p.e.}/p_\theta$. Figure 7–6 shows the averaged $p_{p.e.}/p_\theta$ in each expected momentum bin for the data and the Monte Carlo. They agree within 2.5% level.

7.1.3 Neutrino-Induced Neutral Pions

Invariant mass of a neutrino-induced π^0 could be a calibration source of the absolute energy scale. Because the reconstructed mass depends on the fitted vertex position and ring direction as well as absolute energy scale, this calibration checks the combined systematic error

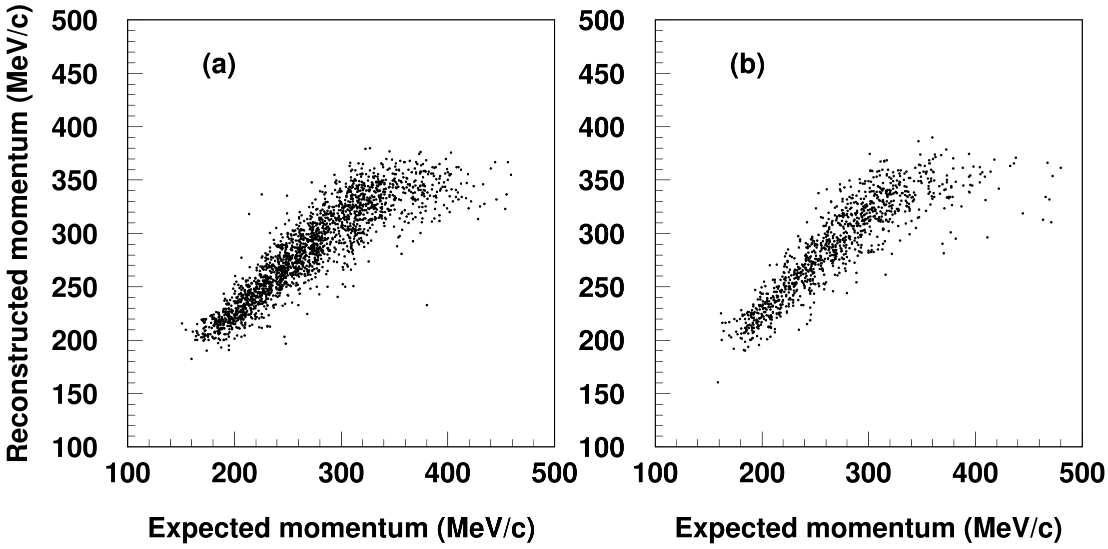

Figure 7–5: Expected muon momentum derived from reconstructed Cherenkov angle and reconstructed momentum distributions for stopping cosmic ray muons. Both (a) data and (b) Monte Carlo are shown. The expected momentum p_θ is derived using the opening angle and the relation $\cos\theta = 1/n\beta = \sqrt{1 + m^2/p_\theta^2}/n$.

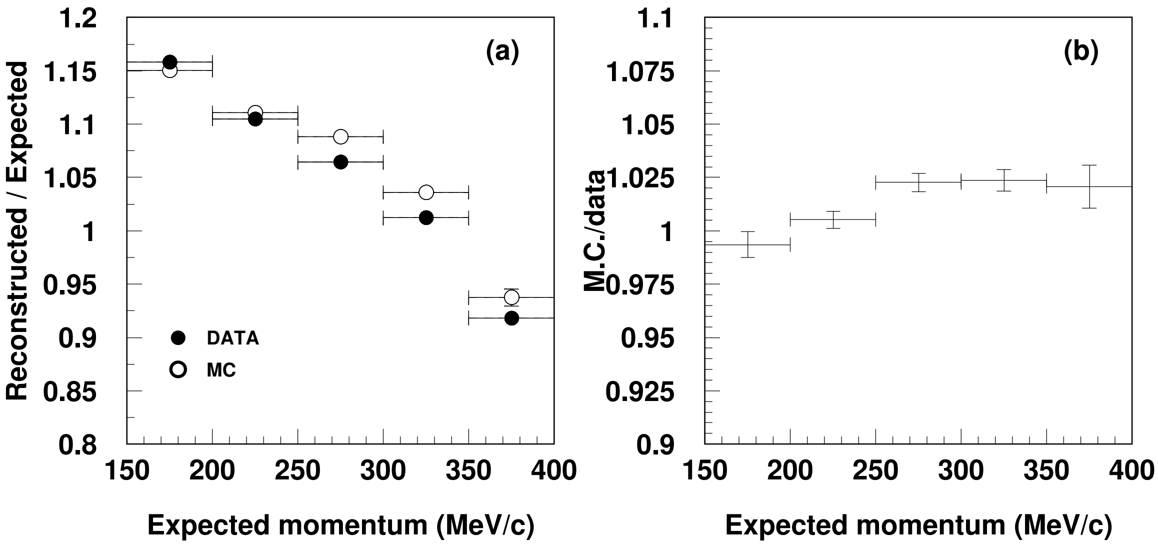

Figure 7–6: The ratio of muon momentum derived from the number of p.e.s and that derived from reconstructed Cherenkov angle for stopping cosmic ray muons. Figure (a) shows the momentum ratios for data and Monte Carlo in each expected momentum bin. Figure (b) shows the ratio of the data and the Monte Carlo.

for the reconstructed mass. Because invariant mass of one combination of two e-like rings is required to be consistent with π^0 mass in the $p \to e^+\pi^0$ search (section 9.1), this comparison of data and Monte Carlo is important. In fully contained event sample (section 8), π^0 events are collected by following criteria.

(a) 2 rings.

(b) both e-like rings.

(c) no decay electron.

By these criteria, we select 2-ring events caused by 2 γ-ray from π^0 decay. Criterion (c) rejects the contamination of $\pi^\pm\pi^0$ and $\mu^\pm\pi^0$ events.

Figure 7–7 shows the reconstructed mass distribution for the selected data and atmospheric neutrino Monte Carlo. Here reconstructed mass M is defined as $M = \sqrt{E_{\rm tot}^2 - P_{\rm tot}^2}$ where $E_{\rm tot} = \sum_{i=1}^{2} |\vec{p}_i|$ and $P_{\rm tot} = |\sum_{i=1}^{2} \vec{p}_i|$. $\vec{p}_i$ is the momentum vector of i-th ring. Reconstructed mass distributions are fitted by a combined function of $f(x) = P1 + P2 \times x + P3 \times \exp[-(x - P4)^2/2P5^2]$ corresponding to a linear background and Gaussian distribution of the π^0 mass. The fitted mass peaks agree with each other within 3% level.

7.1.4 Electrons from Muon Decay

Electrons from the decay of stopping cosmic ray muons could be the relatively low energy (~ 50 MeV) calibration sources which are almost uniformly distributed in the detector. The positron spectrum from the decay of μ^+ is precisely calculated by pure $V - A$ theory as

$$\frac{d\Gamma}{dE_e} = \frac{G_F^2}{12\pi^2} m_\mu^2 E_e^2 (3 - \frac{4E_e}{m_\mu}), \quad E_e \leq \frac{m_\mu}{2}$$

where E_e, m_μ, and G_F are positron energy, muon rest mass, and Fermi coupling constant. In case of μ^-, however, most of μ^- are bound in a ^{16}O orbit and the electron spectrum from the decay of the bound μ^- are distorted [79]. The calculated spectra for the μ^+ decay and bound μ^- decay are shown in Figure 7–8. While the electron spectrum has higher energy tail than the positron spectrum, the difference of mean energy is less than 1%.

Selection criteria for the decay electron events are:

(a) the number of hits in 50 ns window > 40.

(b) time interval from a stopping muon ΔT is 1.5μsec $< \Delta T < 8.0\mu$sec.

(c) the vertex is within fiducial volume.

Criterion (a) corresponds to ~ 8 MeV electron energy and reject ~ 6 MeV gamma rays from μ^- capture on the nucleon. Figure 7–9–(a) shows the reconstructed momentum distributions for data and Monte Carlo. In the Monte Carlo, measured μ^+/μ^- ratio of 1.37 [80] is used. The mean values of the reconstructed momentum agree with each other within 2.2% level. In Figure 7–9–(b), the momenta of the electrons of the data are multiplied by 0.978 and compared with the Monte Carlo.

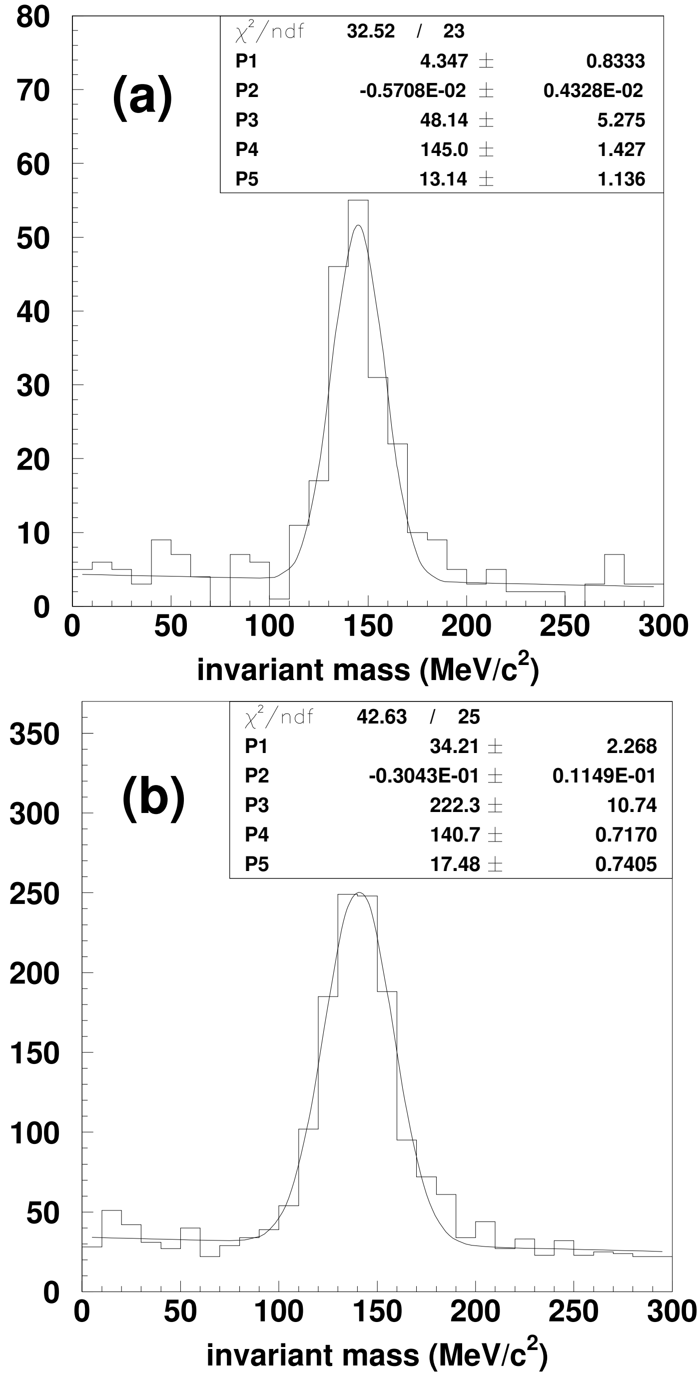

Figure 7–7: The invariant mass distributions for neutrino-induced π^0 events. (a) data and (b) atmospheric neutrino Monte Carlo. Events having two e-like ring with no decay electron are filled in the figure. Reconstructed mass distributions are fitted by a combined function of $f(x) = P1 + P2 \times x + P3 \times \exp[-(x - P4)^2/2P5^2]$. The fitted peaks of invariant mass $P4$ agree well with each other within 3% level.

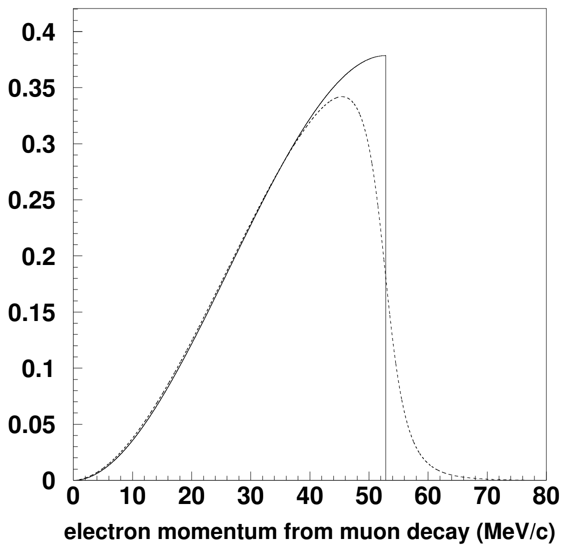

Figure 7–8: Calculated spectrum of $e^{\pm}$ from the decay of muons. Solid line shows spectrum for the decay of free μ^+ and dotted line shows spectrum for the decay of bound μ^- in ^{16}O.

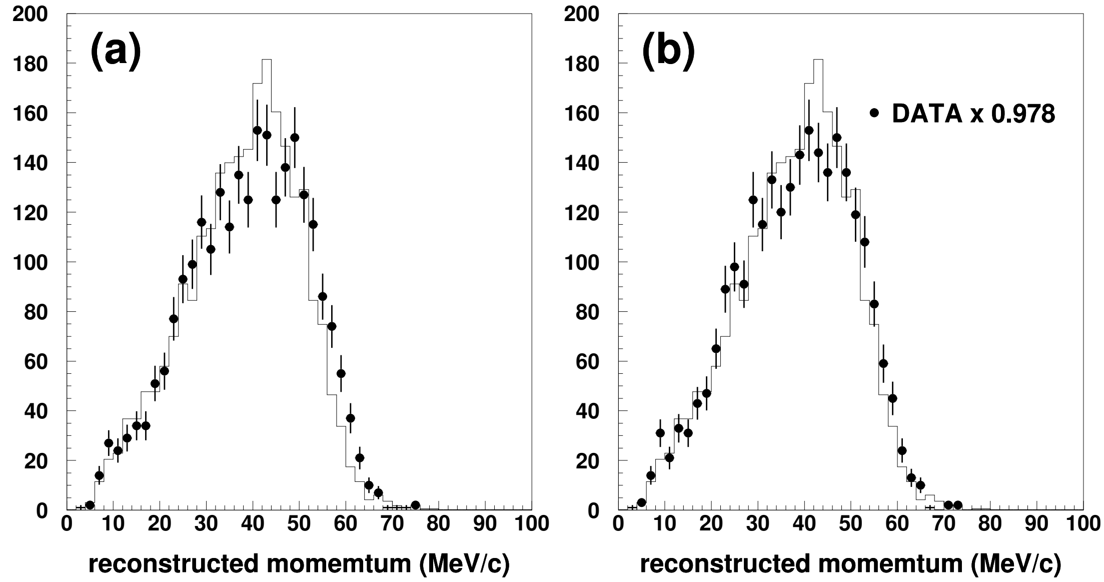

Figure 7–9: The reconstructed momentum distributions for decay electrons. Figure (a) compares the data (filled circles) and Monte Carlo (histogram). The mean values of the reconstructed momentum agree with each other within 2.2% level. In Figure (b), the momenta of data are multiplied by 0.978 to ajust the mean value.

7.1.5 Electrons from Linear Accelerator

For studying the detector response to electrons, a linear accelerator (LINAC) is located near the detector. The LINAC [81] can produce mono-energetic electrons ranging from 5 MeV to 16 MeV which is suitable for studying solar neutrino events. For the proton decay analysis, only 16 MeV data samples are used to calibrate absolute energy scale. The accelerated electrons are injected vertically down-ward to the detector water from the endcap of the beampipe at $(x, y, z) = $ (1237cm,−70.7cm,1206cm). Single electron events are selected and compared with Monte Carlo in Figure 7–10. The mean values of the reconstructed

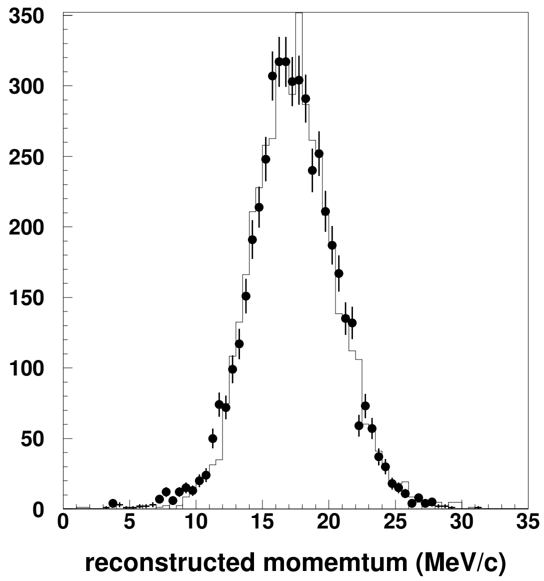

Figure 7–10: The reconstructed momentum distributions for electrons from LINAC. Data (filled circles) and Monte Carlo (histogram) are shown.

momentum are 17.27 MeV/c (data) and 17.46 MeV/c (Monte Carlo) with an agreement of 1.1% level. The fitted peak values by Gaussian distribution are 17.25 MeV/c (data) and 17.22 MeV/c (Monte Carlo) with an agreement of 0.2% level. Therefore, the systematic uncertainty of the energy scale from this calibration is 1.1%.

7.1.6 Summary of Scale Calibrations

In sections 7.1.1 to 7.1.5, several energy calibration sources and calibration results are described. In all comparisons, the absolute energy scale of data agrees well with that of Monte Carlo. Figure 7–11 summarizes the results of all calibrations.

As shown in the Figure, the energy scale of data is well reproduced by the Monte Carlo in the momentum range from ∼200 MeV/c to a few GeV/c. The uncertainty of the energy scale is ±3%.

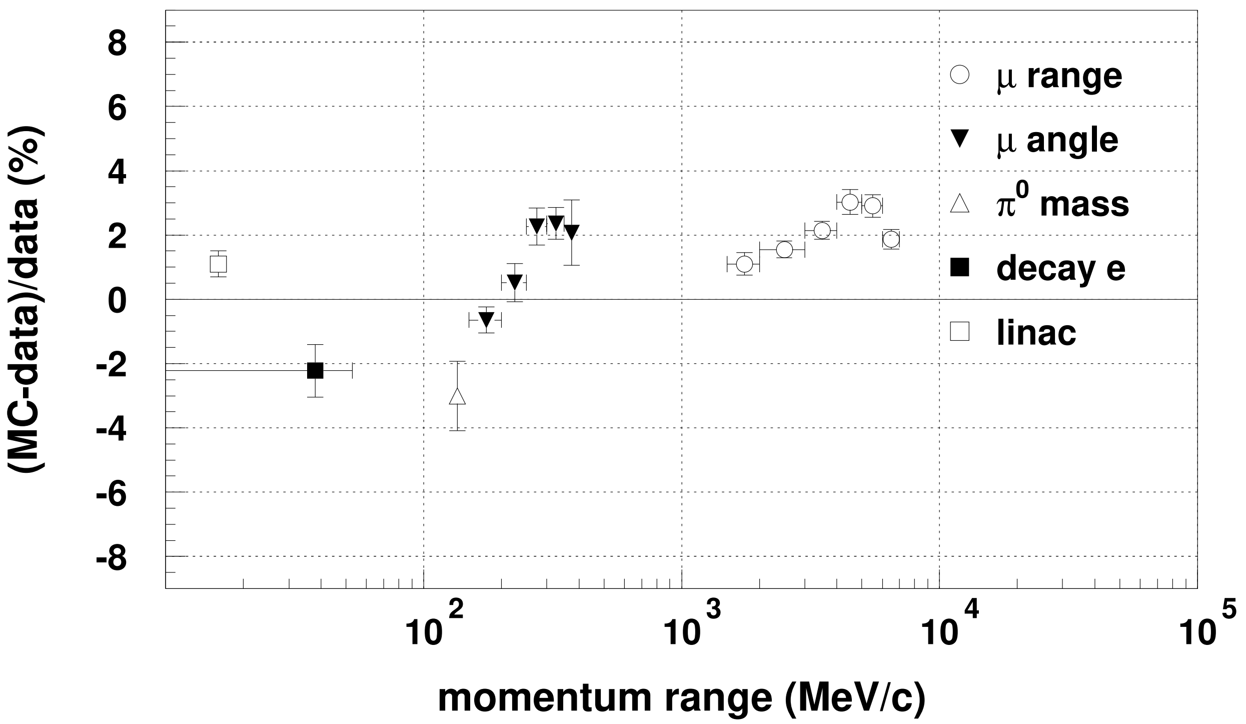

Figure 7–11: Summary of absolute energy scale calibrations. Horizontal axis shows the momentum range of each calibration and vertical axis shows the scale difference between data and Monte Carlo (MC−data/data).

7.2 Detector Stability

The stability of a detector is important for a long term observation. In the Super–Kamiokande detector, several quantities are monitored periodically to check the detector stability.

The time variation of the dark rate of the inner PMTs are checked using several sampled runs and shown in Figure 7–12. The dark rate is stable around 3.1 kHz and we don't need

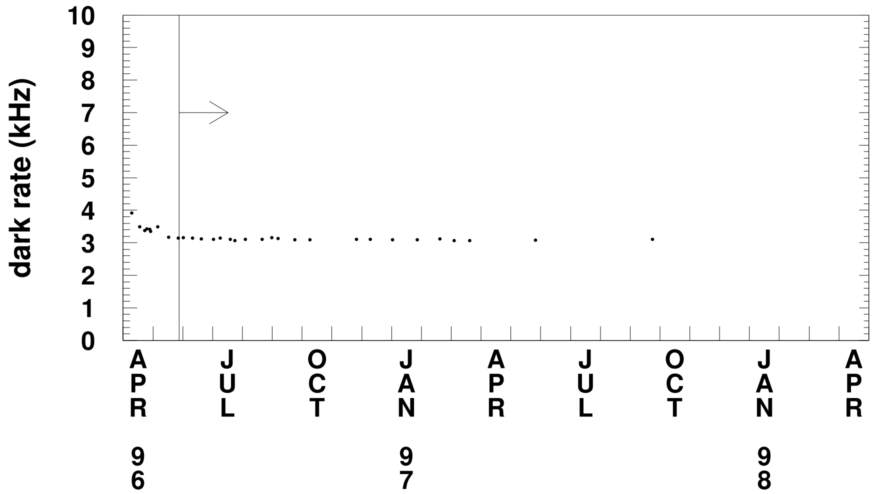

Figure 7–12: The stability of the dark rate of the inner PMTs. It is stable around 3.1 kHz.

time dependent corrections for the variation.

The hit rate for each PMT is always checked and PMTs with abnormal hit rate are assigned as bad channels. These bad channels comprise abnormal PMTs, broken ATM channels and broken channels of high voltage power supplies. Figure 7–13 shows the time variation of the number of bad channels. The number of bad channels, having increased during 1996, is stable from 1997 at 110 $\sim$ 120. ADC/TDC information of these selected bad channels is not used in any event reconstructions and proper correction is performed for the lost information.

Because the light attenuation length in the detector water directly affects the number of p.e.s observed by PMTs, monitoring the attenuation length is important for the momentum reconstruction. Also the PMT gain is crucial and we need to monitor the stability of the gain. Using cosmic ray muons we monitor the time variations of both the attenuation length and the gain (section 3.3.5). Figure 7–14 shows the time variation of the attenuation length and the PMT gain derived from cosmic ray muons. The measured attenuation length varied from 90 m to 120 m during the exposure period analyzed in this thesis. The PMT gain has been increasing by 4% during the period. As described in section 6.5, the measured attenuation length and the PMT gain are used in the momentum reconstruction to correct the number of detected p.e.s.

To check the stability of the reconstructed momentum, decay electrons from stopping cosmic ray muons are used. Figure 7–15–(a) shows the time variation of the reconstructed

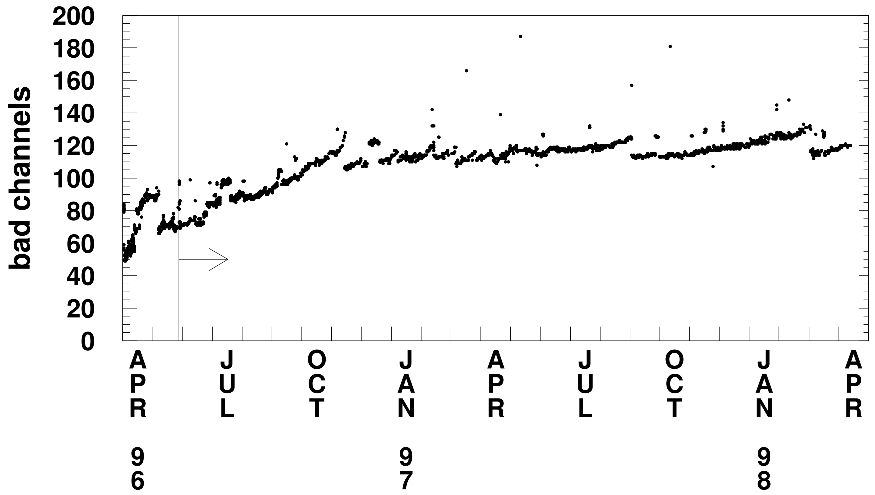

Figure 7–13: The time variation of the number of bad channels.

momentum of the decay electrons. Even though the total number of p.e.s (without any corrections) in the electron events increased by 5% as shown in Figure 7–15–(b), the reconstructed momentum of the decay electrons is stable at $\pm 1\%$ level. Therefore the correction for the bad channels, the attenuation length, and the PMT gain successfully works.

Finally, the stability of the particle identification performance is checked using stopping cosmic ray muons and electrons from the decay of the muons. No significant time variation is seen in Figure 6–5.

7.3 Detector Uniformity

Decay electrons from stopping cosmic ray muons are also utilized to study the uniformity of the detector gain. The decay electrons are good calibration sources because the vertices distribute almost uniformly in the detector and the momentum vector points almost uniformly in all directions so that we can investigate position and direction dependence of the detector gain from the reconstructed momentum of the electrons.

To avoid the muon polarization effect in the estimation of the zenith and azimuthal angle dependence of the detector gain, only electrons decaying in the direction perpendicular to the initial muon direction are used. This condition is $-0.25 < \cos \Theta_{e \leftrightarrow \mu} < 0.25$ where $\Theta_{e \leftrightarrow \mu}$ is the opening angle between the electron and muon directions. Using the selected electrons, the reconstructed momentum of the electrons are plotted as a function of the zenith angle of the electrons. Figure 7–16–(a) shows the zenith angle dependence of the reconstructed momentum. From the figure, the detector gain is uniform in all zenith angle within $\pm 0.6\%$ level.

Figure 7–16–(b) shows the azimuthal angle dependence of the reconstructed momentum. Again, the detector gain is uniform in all azimuthal angle within $\pm 1\%$ level.

Figure 7–17 shows the vertex position dependence of the reconstructed momentum. The

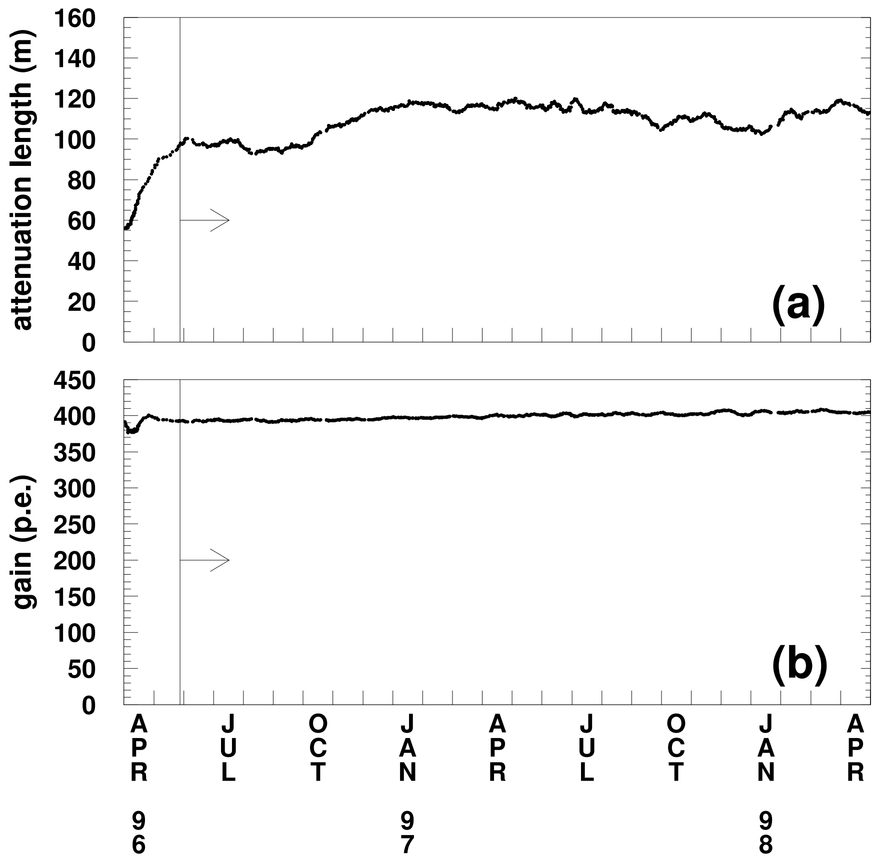

Figure 7–14: The time variation of the light attenuation length and the PMT gain from cosmic ray muons. Figure (a) shows the time variation of the measured attenuation length during the exposure period. It varies from 90 m to 120 m. Figure (b) shows the measured PMT gain which has increased by $\sim 4\%$ level. These monitored values are used to correct the number of detected p.e.s in the momentum reconstruction.

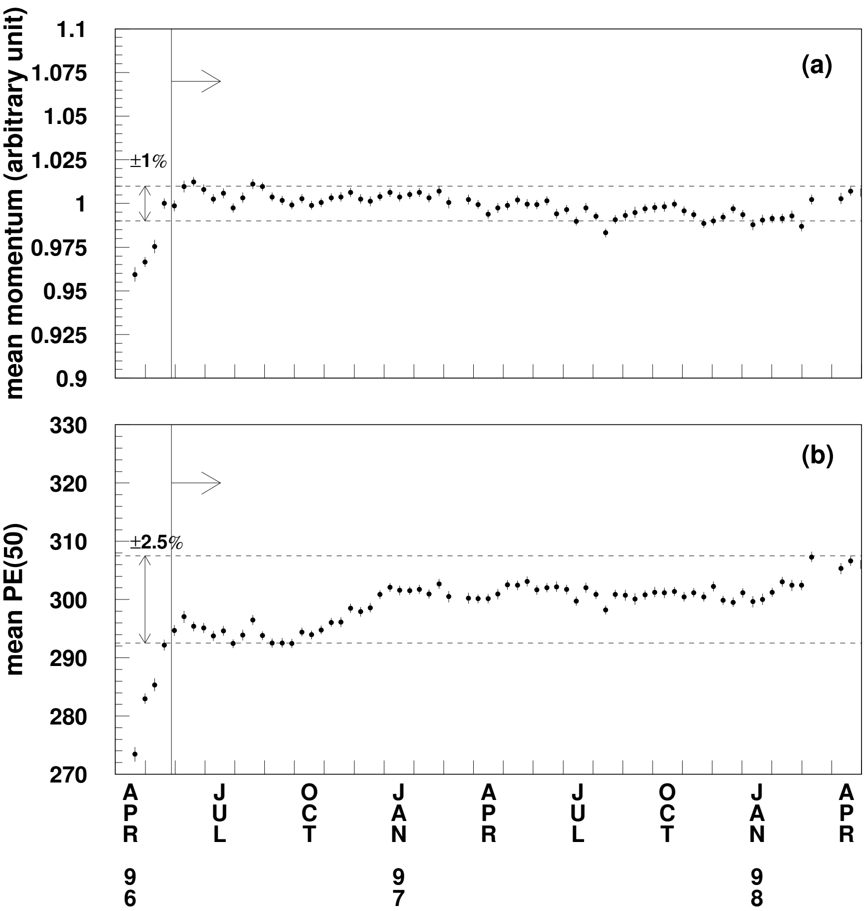

Figure 7–15: Figure (b) shows the total number of p.e.s in 50 nsec time window for electrons from the decay of stopping cosmic ray muons and (a) shows the reconstructed momentum for the electrons. While total number of p.e.s increased by 5%, the reconstructed momentum was stable within ±1%.

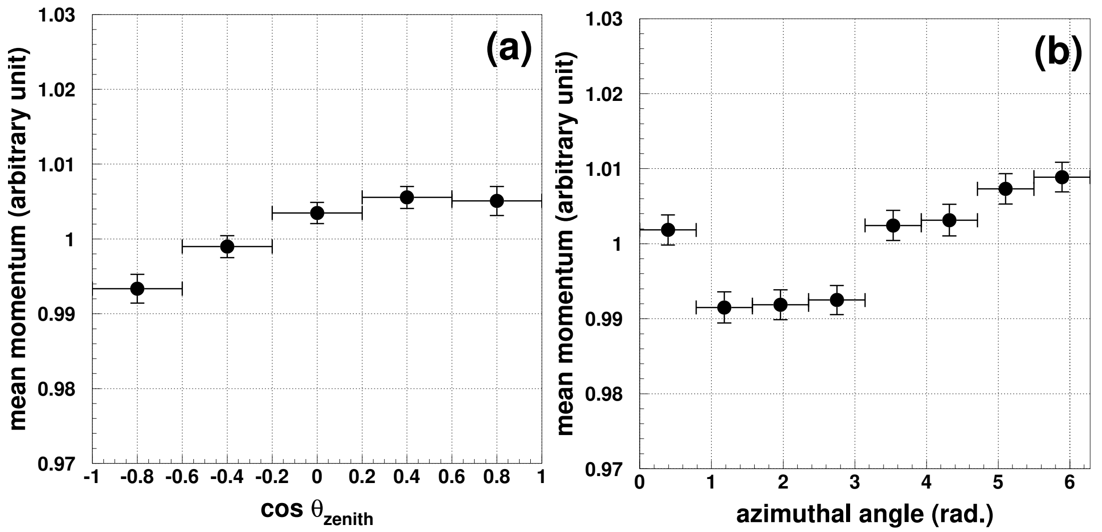

Figure 7–16: The gain uniformity of the Super–Kamiokande. In figure (a), the mean values of reconstructed momentum for decay electrons are shown as a function of the zenith angle. $\cos\theta_{\rm zenith} = 1(-1)$ corresponds to downward (upward) electrons. Figure (b) shows the momentum as a function of the azimuthal angle. The detector gain is uniform within $\pm 1\%$ level.

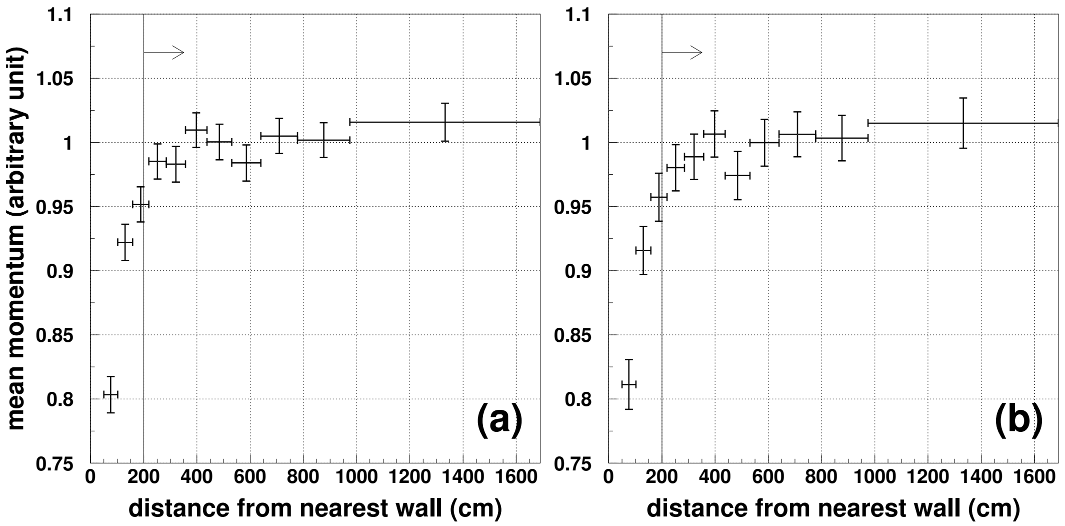

Figure 7–17: The position dependence of the reconstructed momentum for (a) data and (b) Monte Carlo. The mean values of reconstructed momentum for decay electrons are shown as a function of the distance from the nearest wall. The fiducial volume are shown by an arrow. In the fiducial volume, the position dependence of the reconstructed momentum is at 3% level in data. This position dependence of data is well reproduced by MC.

mean momenta are plotted as a function of distance from nearest wall. In the fiducial volume, the position dependence of the reconstructed momentum is at $\pm 3\%$ level for data. The shape of the Monte Carlo (b) reproduces the data well.

8 Characteristics of the Fully Contained Sample

The reduction algorithms (section 5) are applied to the raw data to select fully contained events. The same algorithms are also applied to the atmospheric neutrino MC and $p \to e^+\pi^0$ MC. The characteristics of the selected data as well as that of the atmospheric neutrino MC are compared and discussed in this section. The renormalization of the MC taking into account the neutrino oscillations is discussed in section 8.2. In section 8.1, the data are compared with the atmospheric neutrino MC without neutrino oscillations. The characteristics of the $p \to e^+\pi^0$ MC are discussed in section 9.

8.1 General Distributions

The distributions of the number of rings for the selected data and the atmospheric neutrino MC are shown in Figure 8–1. As discussed in section 9, multi-ring events are used in this proton decay search while single-ring events are used in the atmospheric neutrino analysis. The atmospheric neutrino MC is normalized by livetime. 4476 fully contained events are observed with expected number of events of 4764.1 in the fiducial volume. There is $\sim 25\%$ uncertainty in the absolute normalization in which the absolute neutrino flux uncertainty is 20% and the neutrino cross section uncertainty is 15%. The 10% discrepancy between the data and the MC is within the uncertainty. Also, the data shape is well reproduced by the atmospheric neutrino MC.

Visible energy distributions for all events, single-ring events, and multi-ring events are shown in Figure 8–2. The multi-ring events around 1 GeV is relevant to this analysis.

Figure 8–3 shows the vertex position distributions for the data and the atmospheric neutrino MC. The samples in (a) and (d) are divided into single-ring events ((b) and (e)) and multi-ring events ((c) and (f)). Both for single-ring and multi-ring samples, the shapes of the data in Z and R^2 distributions are in good agreement with that of MC. We can also see from the figures that the contamination of entering muons into the fiducial volume is negligible.

Therefore, all characteristics of the data shown here are well represented by the atmospheric neutrino MC. For the proton decay search, one have to extract possible signals from these neutrino backgrounds.

8.2 Neutrino Oscillations and Re-normalization of MC Events

The Super–Kamiokande collaboration reported the evidence for the neutrino oscillations in the atmospheric neutrinos. Due to the oscillations, the observed flavor ratio $(\nu_\mu+\overline{\nu}_\mu)/(\nu_e+\overline{\nu}_e)$ ($\equiv \nu_\mu/\nu_e$) is smaller than expected one. This anomalous flavor ratio as well as the zenith angle distributions is well explained by $\nu_\mu \leftrightarrow \nu_\tau$ two flavor oscillation hypothesis. Table 8–1 summarizes the observed fully contained events along with MC predictions. Here we show only sub-GeV sample because the interesting energy region for the proton decay search is around 1 GeV. For the sub-GeV sample, we require $p_e > 100$ MeV/c for e-like events and $p_\mu > 200$ MeV/c for μ-like events, and visible energy < 1.33 GeV. The table shows that the

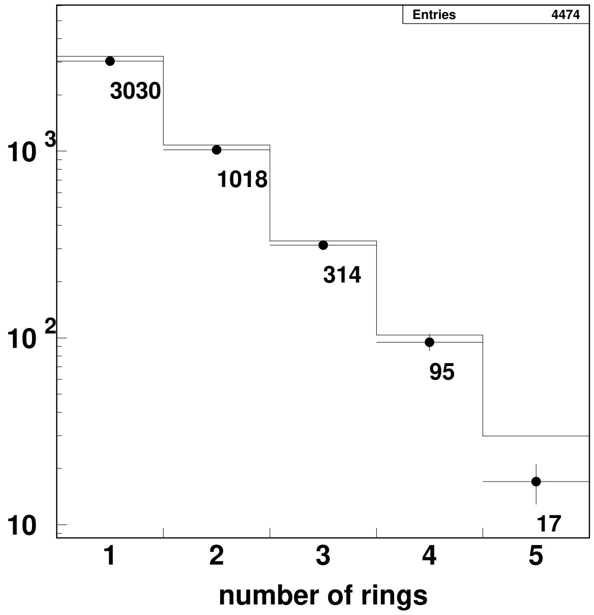

Figure 8–1: The number of ring distribution for fully contained events in data (filled circle) and atmospheric neutrino MC (histogram). The fractions of single- and multi-ring events in the data are 68% and 32% respectively.

		DATA	MC	$\nu_e, \overline{\nu}_e$ CC	$\nu_\mu, \overline{\nu}_\mu$ CC	NC
single-ring	e-like	1231	1049.1	88%	2%	10%
	μ-like	1158	1573.6	0.5%	96%	4%
multi-ring		911	1049.1	24%	43%	33%

Table 8–1: Summary of observed events and MC predictions in sub-GeV region. The estimated contributions from charged current (CC) interactions and neutral current (NC) interactions are also shown.

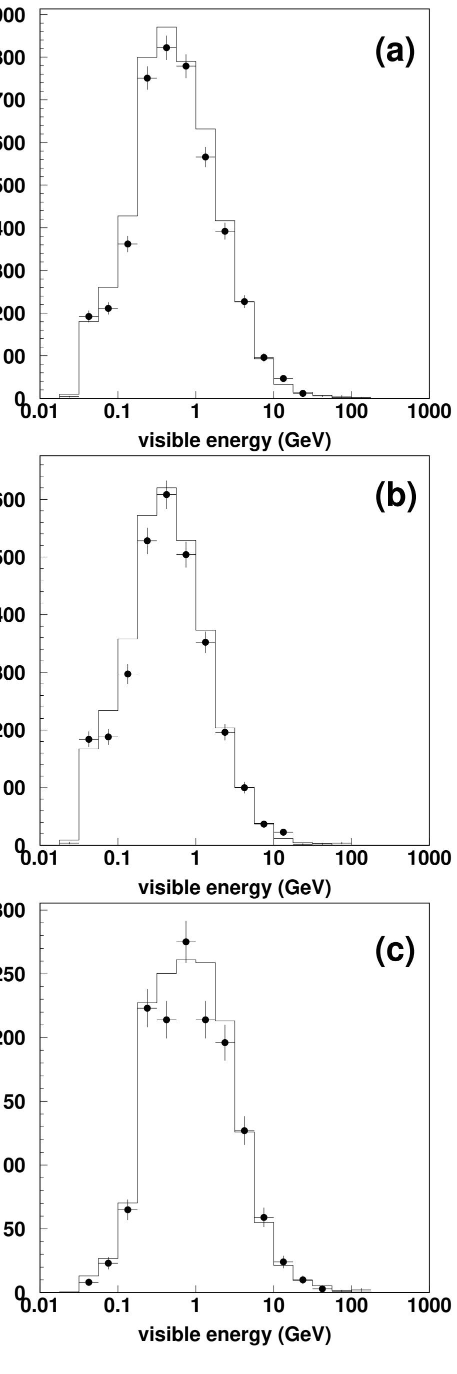

Figure 8–2: The visible energy distributions for fully contained event sample. (a) all fully contained events, (b) single-ring events, and (c) multi-ring events. The multi-ring events around 1 GeV are relevant to this analysis.

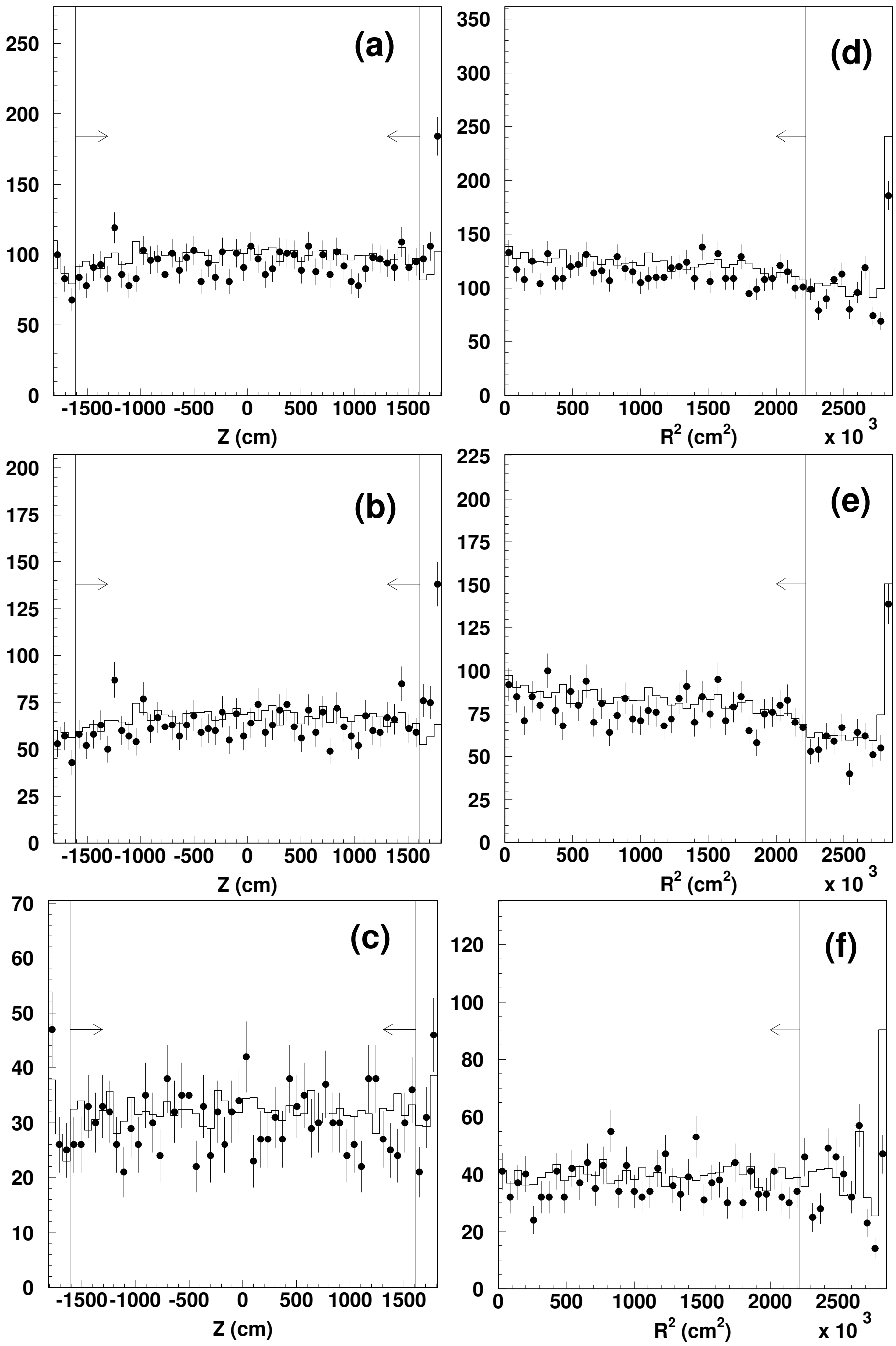

Figure 8–3: The vertex position distributions for fully contained sample. Z distributions of the events with $R < 14.9$ m are shown for (a) all, (b) single-ring, and (c) multi-ring events. Also, R^2 distributions of the events with $|Z| < 16.1$ m are shown for (d) all, (e) single-ring, and (f) multi-ring events. Lines and arrows show the fiducial volume.

number of e-like events is 17% larger than expected one while the number of μ-like events is 26% smaller. Both discrepancies are well understood by the $\nu_\mu \leftrightarrow \nu_\tau$ oscillations and the uncertainty of the absolute normalization. Figure 8–4 shows the momentum distributions for (a) sub-GeV e-like events, (b) μ-like events, and (c) the double ratio $(\mu/e)_{DATA}/(\mu/e)_{MC}$. Neither the excess of e-like events nor the deficit of μ-like events don't have any significant momentum dependence.

For various comparisons of data and atmospheric neutrino MC, the neutrino MC sample is renormalized to the number of observed atmospheric neutrino events at Super–Kamiokande in the following manner. The number of ν_e (ν_μ) CC events is normalized by the ratio of the number of single ring events with an e-like (μ-like) particle identification (PID) in the data to the number of single ring events with an e-like (μ-like) PID in the atmospheric neutrino MC. For NC events, the same normalization factor as that of the ν_e CC events is used due to the $\nu_\mu \leftrightarrow \nu_\tau$ two flavor oscillation hypothesis. For all comparisons between the data and the neutrino MC in the next section, these renormalization factors are used.

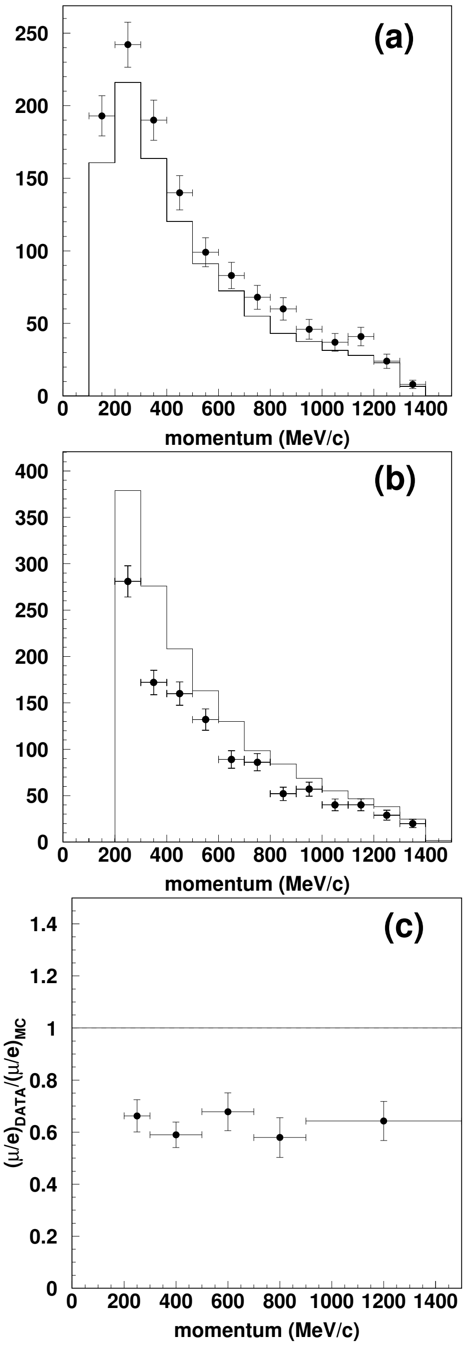

Figure 8–4: The momentum distributions for sub-GeV sample. (a) e-like events, (b) μ-like events, and (c) the double ratio $(\mu/e)_{DATA}/(\mu/e)_{MC}$ are shown as a function of momentum.

9 Proton Decay Analysis

In section 5, the reduction algorithms for fully contained events are explained. For the remaining fully contained events, additional selection criteria are required to select $p \to e^+\pi^0$ candidates. In this section, the selection criteria for the $p \to e^+\pi^0$ signal are described and after that, the results of proton decay search are shown. Finally, systematic errors concerning this proton decay search are considered.

9.1 Proton Decay Selection Criteria

To extract the $p \to e^+\pi^0$ signal from the fully contained event sample, proton decay selection criteria are defined:

(A) 6800 p.e. $<$ total p.e. $<$ 9500 p.e.

(B) the number of rings is 2 or 3

(C) all rings have a showering particle identification (PID)

(D) 85 MeV/c^2 $< \pi^0$ mass $<$ 185 MeV/c^2

(E) no decay electron

(F) 800 MeV/c^2 $<$ total invariant mass $<$ 1050 MeV/c^2 and
total momentum $<$ 250 MeV/c

Criterion (A) roughly corresponds to a total energy of 800 MeV to 1100 MeV. Figure 9–1 shows the total p.e. distribution of the $p \to e^+\pi^0$ MC sample. The shaded histogram is the distribution for free proton decays and this criteria (A) is safe for the free proton decay. On the other hand, the blank histogram shows the distribution for protons in ^{16}O. It has lower p.e. peak below the criterion (A) which is due to π^0 interactions in ^{16}O nucleus, namely π^0 absorption, charge exchange, and scattering in ^{16}O nucleus.

After the criterion (A), criterion (B) is applied to select 2 or 3-ring events. The number of ring distribution of $p \to e^+\pi^0$ MC is shown in Figure 9–2. In the sample, 98% events are categorized as 2-ring or 3-ring events and pass the criterion (B).

Criterion (C) selects $e^\pm$ and γ using particle type information. Figure 9–3 shows PID parameters for each ring of the $p \to e^+\pi^0$ sample. The negative (positive) parameter value corresponds to showering (nonshowering) particle type. After criteria (A) and (B), almost all rings are electromagnetic shower caused by positron or γ from the decay of π^0. For each ring of the proton decay sample, misidentification probability is estimated to be 2%.

Criterion (D) is applied to only 3-ring events. Here, at least one pair of rings must give a reconstructed invariant mass which is consistent with the estimated π^0 mass resolution of 135 ± 35 MeV/c^2. The invariant π^0 mass distribution for the $p \to e^+\pi^0$ MC sample is shown in Figure 9–4. The efficiency to pass the criterion (D) is 88% for 3-ring events of this sample.

Criterion (E) is required since e^+ and π^0 produce no decay electrons. This criterion is useful to reject atmospheric neutrino backgrounds without any loss of detection efficiency.

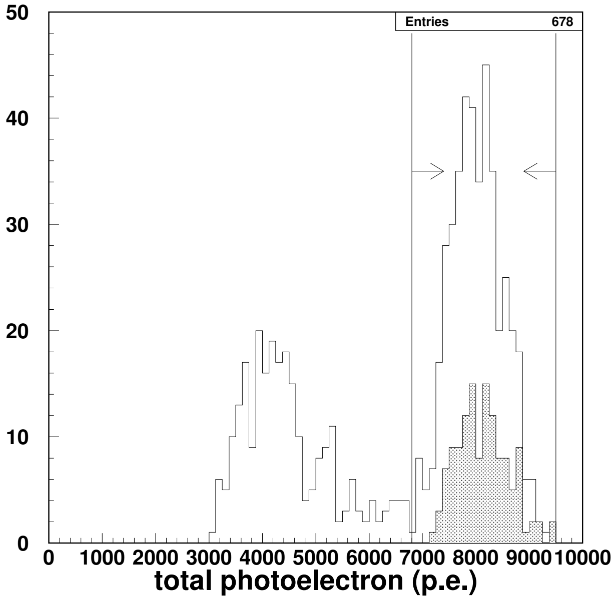

Figure 9–1: Total p.e. distribution for $p \to e^+\pi^0$ MC events. Proton decay selection criterion (A) 6800 p.e. $<$ total p.e. $<$ 9500 p.e. is shown by arrows. The shaded histogram is the distribution for free proton and the blank histogram shows the distribution for protons in ^{16}O. The high p.e. peak in the cut region corresponds to proton decay in ^{16}O without π^0 interactions in the ^{16}O nucleus or free proton decay. The lower p.e. peak below the criterion (A) corresponds to proton decay in ^{16}O with π^0 interactions in the ^{16}O nucleus, namely π^0 absorption, charge exchange, and scattering on ^{16}O.

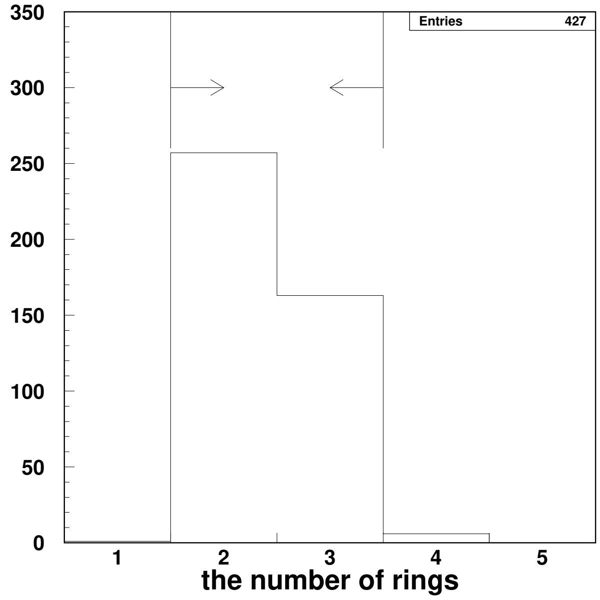

Figure 9–2: The number of ring distribution for $p \to e^+\pi^0$ MC events. Proton decay selection criterion (B) selects 2-ring and 3-ring events. In this sample, 98% events are categorized as 2-ring or 3-ring events.

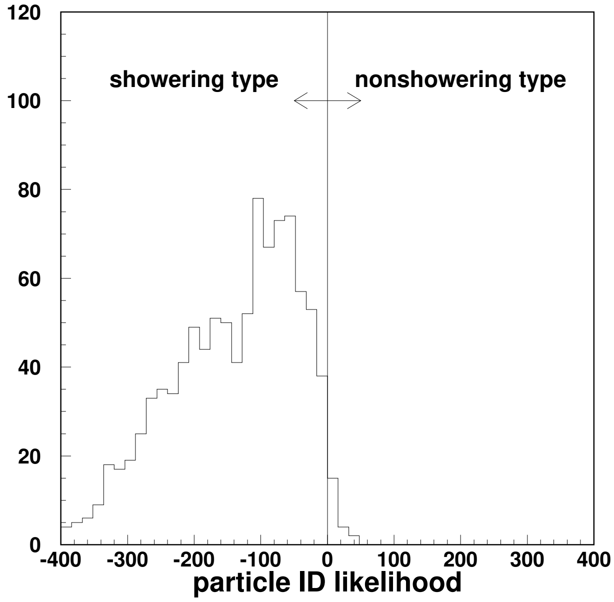

Figure 9–3: Particle ID parameter for each ring of $p \to e^+\pi^0$ MC events. The negative (positive) value of the parameter corresponds to showering (nonshowering) particle type. Misidentification probability is 2% for this sample.

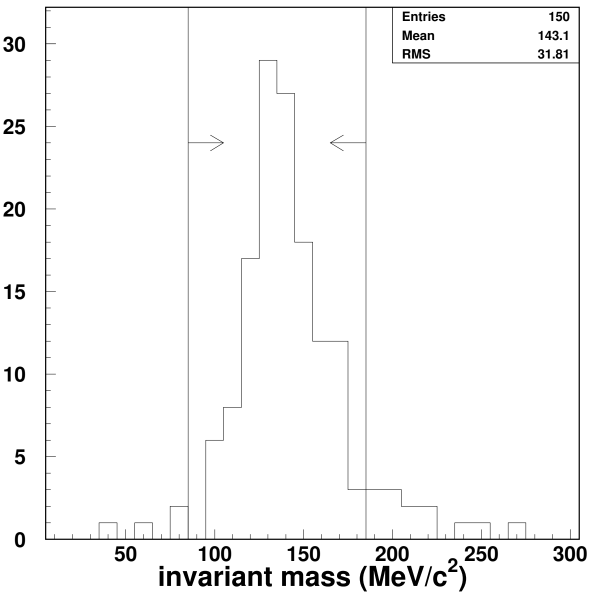

Figure 9–4: Invariant π^0 mass for 3-ring $p \to e^+\pi^0$ MC events. The proton decay selection criteria (D) 85 MeV/c < invariant π^0 mass < 185 MeV/c is shown by arrows.

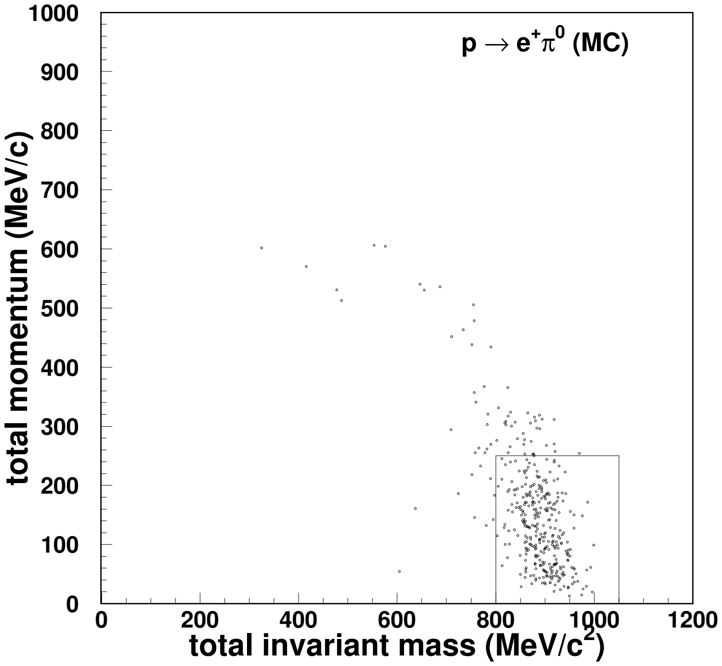

Figure 9–5: Total invariant mass and total momentum distribution for $p \to e^+\pi^0$ MC after the criteria (A)–(E) (see text). The boxed region in the figure shows the selection criterion (F) 800 MeV/c^2 < total invariant mass < 1050 MeV/c^2 and total momentum < 250 MeV/c^2.

In criterion (F), the total momentum is defined as $P_{\text{tot}} = |\sum_i^{\text{allrings}} \vec{p}_i|$ where $\vec{p}_i$ is reconstructed momentum vector of i-th ring. The total invariant mass is defined as $M_{\text{tot}} = \sqrt{E_{\text{tot}}^2 - P_{\text{tot}}^2}$ where total energy $E_{\text{tot}} = \sum_i^{\text{allrings}} |\vec{p}_i|$. Criterion (F) checks that the total invariant mass and total momentum correspond to the mass and momentum of the source proton, respectively. Figure 9–5 shows total invariant mass and total momentum distribution for the $p \to e^+\pi^0$ MC sample after the criteria (A)–(E). The boxed region in the figure shows the criterion (F). From this sample, the detection efficiency of $p \to e^+\pi^0$ events is estimated to be 44%.

In summary, detection efficiencies after each criterion are shown in fugure 9–6. The efficiency for free proton decay (star) and proton decay in ^{16}O (empty circle) are separately shown. The selection criteria (A) through (F) keep the efficiency of 91% for the free proton decay. On the other hand, only 35% proton decay in ^{16}O are identified. It is shown in Figure 9–6 that the large reduction mainly comes from the criterion (A) 6800 p.e. < total p.e. < 9500 p.e.. This means that the absorption, charge exchange and scattering of π^0's in the ^{16}O nucleus are the dominant contribution to the detection inefficiency. The combined efficiency (filled circle) are also shown in the figure and the total detection efficiency is found to be 44%.

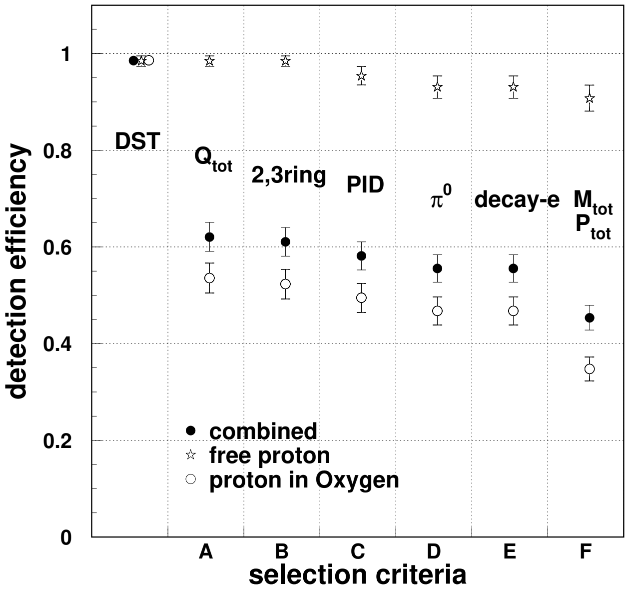

Figure 9–6: Detection efficiencies after each criterion (A)–(F) (see text) for $p \to e^+\pi^0$ MC events. DST means all fully contained events in the fiducial volume. The efficiency for free proton decay (star) and proton decay in ^{16}O (empty circle) are separately shown. The combined efficiency (filled circle) are also shown and the total detection efficiency is 44%.

9.2 Background

To estimate the background from atmospheric neutrino interactions, the atmospheric neutrino MC sample of 900 kton·year exposure equivalent is generated (section 8). The reduction algorithms (section 5) are applied to the sample in the same ways as the data to select the fully contained events (section 8). By applying the proton decay selection criteria (A) through (F) (section 9.1) to this sample, the number of background events in the signal region is estimated. In the 900 kton·year sample, there are three events which pass all selection criteria. Therefore the number of background is estimated to be 0.1 event in 32.9 kton·year. Figure 9–7 shows the total invariant mass and total momentum distribution for the neutrino MC sample after the criteria (A)–(E).

The characteristics of the three background events passing the proton decay selection criteria are listed in Tables 9–1 and 9–2. All of the three background events are caused by charged current ν_e interactions producing one electron and one π^0. Because the protons in the final state have too low momentum to produce much Cherenkov light, it is difficult to tag the proton by a water Cherenkov detector. Therefore, they mimic the proton decay signal $p \to e^+\pi^0$. The various distributions of physical quantities are discussed in the next section.

	neutrino flavor, energy (MeV/c)	interaction	comments
BG1	ν_e, 1604	$\nu_e n \to e p \pi^0$	
BG2	ν_e, 1565	$\nu_e p \to e p \pi^+$	π^+ and π^0 are produced by the π^+ in water.
BG3	ν_e, 1592	$\nu_e p \to e p (\pi^+) \pi^0$	π^+ didn't exit from ^{16}O nucleus.

Table 9–1: The characteristics of the neutrino background events.

	total p.e.	the number of ring	π^0 mass (MeV/c^2)	total mass (MeV/c^2)	total momentum (MeV/c)
BG1	7930.6	3	132.9	842.4	221.7
BG2	7808.3	2	—	886.8	153.9
BG3	7641.2	2	—	862.9	242.2

Table 9–2: The measured physical quantities of the neutrino background events. All quantities are within the proton decay selection criteria (A)–(F) (see text).

9.3 Results

Finally the same criteria are applied to the data to search for the $p \to e^+\pi^0$ signal. Figure 9–8 shows total invariant mass and total momentum distribution for the data sample after the criteria (A)–(E). In the 32.9 kton·year data, no events survive all criteria as shown in the figure.

For consistency check between data and atmospheric neutrino MC, several comparisons are made. First, the 2-dimensional distributions of total mass and total momentum (Figure 9–5, 9–7, 9–8) should be compared. To make the comparison clear, these distribution are projected in a 1-dimensional plot of "L" which is defined as a distance between each event point and a line in the proton decay signal region. Figure 9–9 shows the distribution of "L" for $p \to e^+\pi^0$ MC, atmospheric neutrino MC, and data along with the definition of "L". It is clearly seen that the data distribution are well reproduced by the neutrino MC.

Figure 9–10 compares the reconstructed total mass for atmospheric neutrino MC, the $p \to e^+\pi^0$ MC, and the data events which satisfy the criteria (B)–(E) and have a total reconstructed momentum < 250 MeV/c. For this comparison criterion (A) is not imposed to provide enough statistics. The clear peaks of π^0 mass are seen in both the data and the neutrino MC. The mass distributions for the data and the neutrino MC have good agreement.

Figure 9–11 compares the reconstructed total momentum for the three samples which satisfy the criteria (B)–(E) and have a total reconstructed mass of 800 MeV/c^2 to 1050 MeV/c^2. For this comparison criterion (A) is omitted again. The momentum distribution of data is also well reproduced by the neutrino MC.

Finally, Figure 9–12 shows the event rate after applying each of criteria (A) through (F) for the data and atmospheric neutrino MC events. The event rate is normalized to

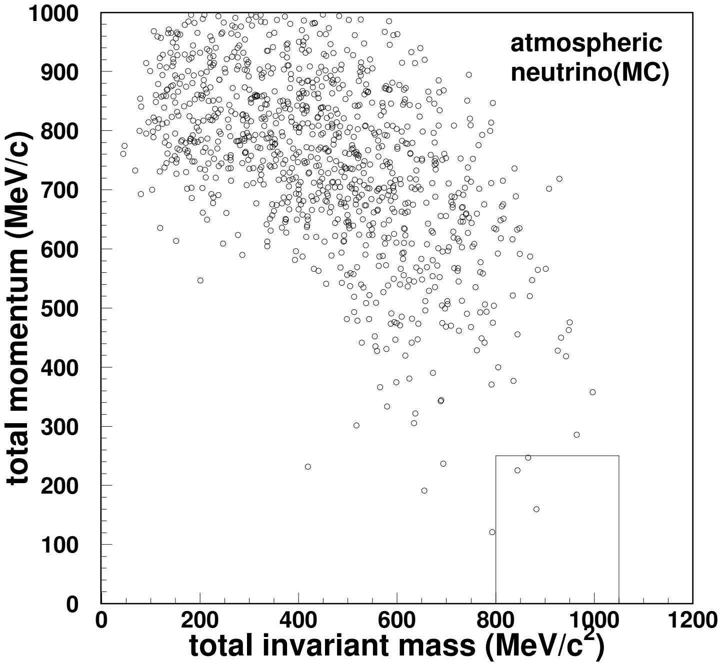

Figure 9–7: Total invariant mass and total momentum distribution for atmospheric neutrino MC after the criteria (A)–(E) (see text). The boxed region shows the selection criterion (F) 800 MeV/c^2 < total invariant mass < 1050 MeV/c^2 and total momentum < 250 MeV/c^2.

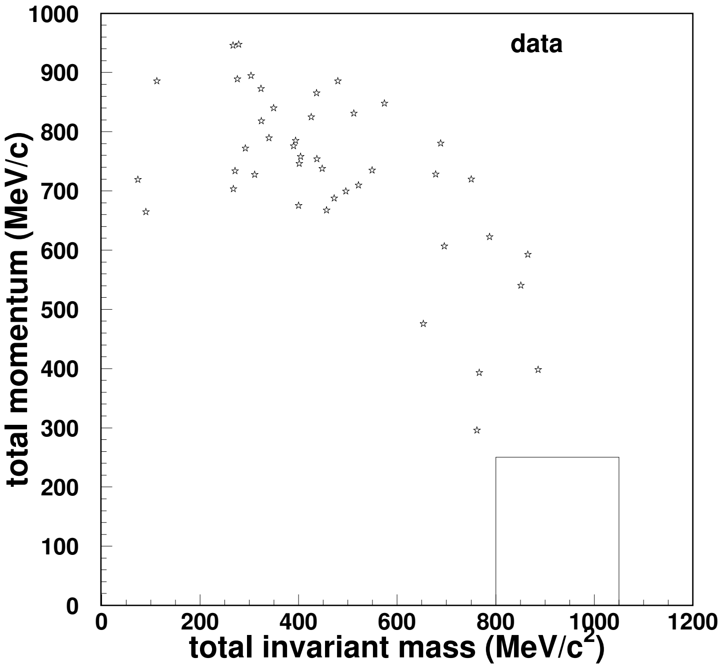

Figure 9–8: Total invariant mass and total momentum distribution for data after the criteria (A)–(E) (see text). The boxed region shows the selection criterion (F) 800 MeV/c^2 < total invariant mass < 1050 MeV/c^2 and total momentum < 250 MeV/c^2.

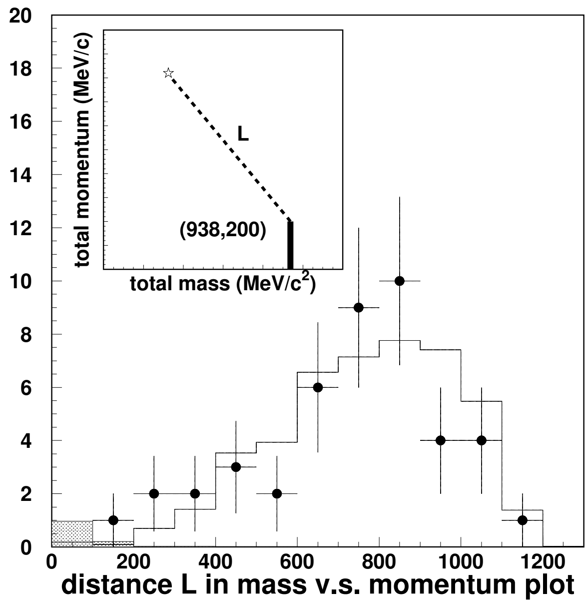

Figure 9–9: Distance "L" distributions in mass v.s. momentum plot for data (circles), normalized atmospheric neutrino Monte Carlo events corresponding to 900 kton·year (unshaded histogram), and $p \to e^+\pi^0$ Monte Carlo normalized to one event in signal region (shaded histogram) which satisfy the criteria (A)–(E) (see text). In the upper left figure, the "L" is defined as a distance between each event point and the line in the proton decay signal region.

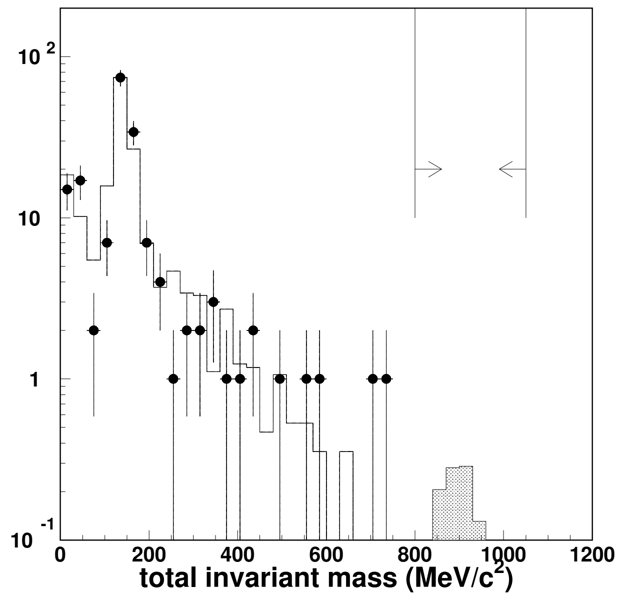

Figure 9–10: The total invariant mass distributions for data (circles), normalized atmospheric neutrino Monte Carlo events corresponding to 225 kton·year (unshaded histogram), and $p \to e^+\pi^0$ Monte Carlo events normalized to one event in signal region (shaded histogram) which satisfy the criteria (B)–(E) (see text) and have a total reconstructed momentum $<$ 250 MeV/c.

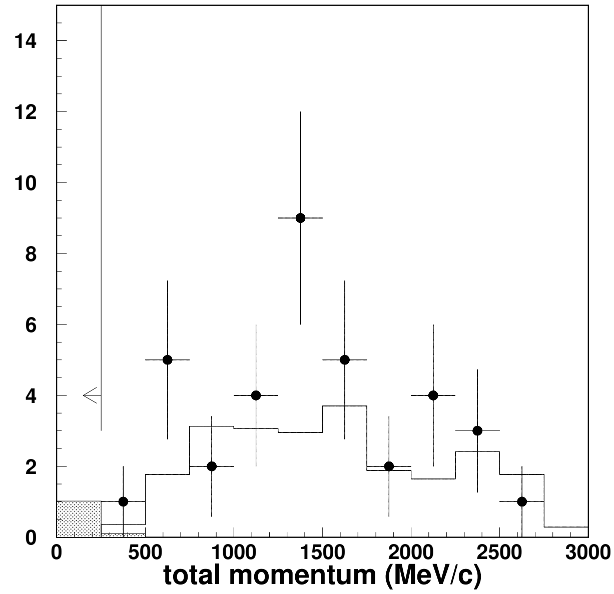

Figure 9–11: Total momentum distributions for data (circles), normalized atmospheric neutrino Monte Carlo events corresponding to 225 kton·year (unshaded histogram), and $p \rightarrow e^{+}\pi^{0}$ Monte Carlo normalized to one event in signal region (shaded histogram) which satisfy the criteria (B)–(E) (see text) and have a total invariant mass of 800 MeV/c^2 to 1050 MeV/c^2.

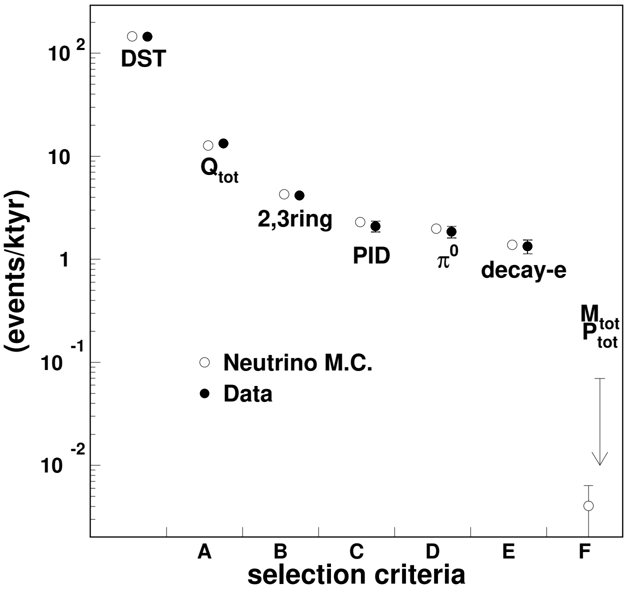

Figure 9–12: The event rate after each proton decay selection criterion (see text) for data (filled circles) and atmospheric neutrino Monte Carlo (empty circles). DST means all fully contained events in the fiducial volume. There is no event in the data after criterion (F) and only the 90% CL upper limit is shown in the last bin.

(kton·year)$^{-1}$. The event rate of the data are well represented by the neutrino MC.

9.3.1 Limit Calculation

From these results, I conclude that no evidence of the proton decay in the mode $p \to e^+\pi^0$ is observed. Therefore, I calculate the lower limit on the lifetime of proton. The quantities of this calculation are the detection efficiency of 44%, 0 candidate events out of 32.9 kton·year data, and 3 background candidates out of 900 kton·year of the simulated atmospheric neutrino interactions. Assuming mean of the number of backgrounds μ_B is known with negligible systematic uncertainty, the upper limit on mean of the number of signal N can be defined using Poisson distribution:

$$CL = 1 - \frac{e^{-(\mu_B+N)} \displaystyle\sum_{n=0}^{n_0} \frac{(\mu_B + N)^n}{n!}}{e^{-\mu_B} \displaystyle\sum_{n=0}^{n_0} \frac{(\mu_B)^n}{n!}} \tag{9-1}$$

where CL is a confidence level and n_0 is the number of observed candidates. Applying $n_0 = 0$, the upper limit N is calculated to be 2.30 at 90% confidence level. Due to 0 observed candidates, the upper limit N is independent on the background μ_B. Using the N, the upper limit on the partial lifetime of proton $\tau/B_{p\to e^+\pi^0}$ is calculated as:

$$\tau/B_{p\to e^+\pi^0} = \frac{\lambda \times \frac{10}{18} \times N_A \times \epsilon}{N} \tag{9-2}$$

where λ is the exposure of 32.9 kton·year, N_A is Avogadro's number, and ϵ is the detection efficiency for $p \to e^+\pi^0$ of 44%. Therefore, the resulting limit on the partial lifetime for $p \to e^+\pi^0$ is found to be, $\tau/B_{p\to e^+\pi^0} = 2.1 \times 10^{33}$ years at 90% confidence level. The lifetime limit will be calculated again taking into account systematic uncertainties in section 9.4.

9.4 Systematic Errors

In this section, I would like to discuss systematic errors concerning the partial lifetime limit $\tau/B_{p\rightarrow e^+\pi^0}$. The sources of systematic uncertainty are:

- detection efficiency ϵ
  - pion-nucleon scattering in ^{16}O nucleus
  - energy scale
  - uniformity of detector gain
  - particle ID
  - fitting biases
- detector exposure λ
  - detector size
  - livetime

In calculating the limit, the parameter with the dominant uncertainty is the detection efficiency. This uncertainty is primarily due to imperfectly known pion–nucleon cross sections in ^{16}O nuclei. The contributions to the detection inefficiency from the pion–nucleon scattering are summarized in Table 9–3. Because almost all events in which π^0 interacts within the ^{16}O nucleus are not able to pass the proton decay criteria, the probability of the interaction directly affects the detection efficiency of the $p \rightarrow e^+\pi^0$. To estimate the uncertainty of the pion interaction, Table 9–4 compares the probability of π^0 interaction in ^{16}O using several pion-nucleon scattering models. The fraction of π^0 free escape is most important for evaluating the detection efficiency. The model "SK" used in this analysis agrees with the model "Kam" [40] developed for the Kamiokande experiment and Nishimura's model [40, 83]. The largest difference of π^0 free escape is found to be 11% between the model "SK" and model "IMB" [82]. It contributes $\sim$15% difference in the total detection efficiency of $p \rightarrow e^+\pi^0$.

The uncertainty of the energy scale is also the possible source of the systematic error. By changing the total invariant mass and total momentum cut (criterion (F)) by $\pm$3% (section 7.1.6), the detection efficiency for $p \rightarrow e^+\pi^0$ MC events is changed by 1%. The time variations of attenuation length and PMT gain affect the total p.e.s of candidates and $\pm$5% (section 7.2) change of total p.e.s causes $<$ 1% change of detection efficiency.

The ununiformity of the detector gain can cause systematic error in the momentum balance because a positron and a $\pi^0(\gamma\gamma)$ would emit Cherenkov photons onto different sides of the detector. The 3% (section 7.3) ununiformity could change the total momentum of candidates up to $\pm$6%. By changing the total momentum cut (criterion (F)) by $\pm$6%, the contribution to the uncertainty of the detection efficiency is estimated to be $\pm$2%.

By $\pm$2% change of the particle misidentification probability of 2% (section 9.1), the contribution to the uncertainty of the detection efficiency is estimated to be $\pm$5%.

	all	identified
free proton	19%	17%
proton in ^{16}O	81%	28%
π^0 free escape	37%	27%
π^0 absorption	18%	0%
π^0 charge exchange	13%	0%
other inelastic scattering	13%	1%
total	100%	44%

Table 9–3: The detection efficiency and π^0 interactions in ^{16}O nucleus. The last column shows the fraction of $p \to e^+\pi^0$ events which pass the proton decay criteria.

	SK	Kam	Nishimura	IMB
π^0 free escape	43%	43%	46%	54%
π^0 absorption	24%	14%	27%	22%
π^0 charge exchange	16%	16%	12%	10%
π^0 other inelastic	17%	27%	15%	14%
total	100%	100%	100%	100%

Table 9–4: Comparisons of π^0–nucleon scattering probability in ^{16}O nuclei for $p \to e^+\pi^0$. The SK refers the model used in this analysis. The Kam (IMB) refers the model developed for Kamiokande [40] (IMB [82]) experiment. Estimations by Nishimura [40, 83] are also shown.

	uncertainty
detection efficiency	18%
pion-nucleon scattering in ^{16}O nucleus	15%
energy scale	<2%
uniformity of detector gain	2%
particle ID	5%
fitting biases	7%
exposure	<1%
detector size	<1%
livetime	<0.1%

Table 9–5: The list of systematic uncertainties.

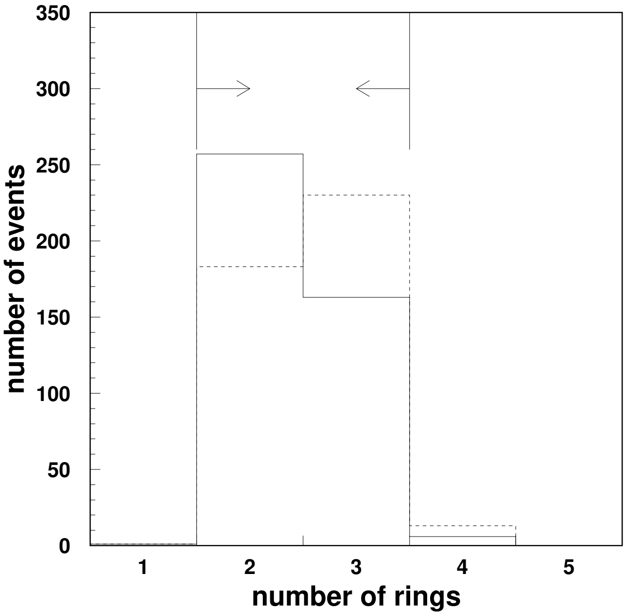

Figure 9–13: Comparison of two different ring fitting programs for $p \to e^+\pi^0$ events. Total p.e. cut (selection criterion (A) in section 9.1) is applied before the comparison. Solid histogram shows the original fitting program and dashed one shows a modified fitting program.

Unknown fitting bias in the ring counting is estimated by using a modified ring fitting program. This program uses sophisticated technic of enhancing peaks in Hough space (appendix A.2). Thanks to the technic, this modified program reconstructs more rings than the original one. In Figure 9–13, the modified and original ring fitter are compared with each other using $p \to e^+\pi^0$ MC. Although the number of 2-ring events and 3-ring events are changed by 20–30%, the total number of 2 or 3-ring events is not changed much. After applying all proton decay selection criteria, the detection efficiency is changed by 4%. Moreover, possible fitting biases in the event vertex, ring direction, and opening angle of Cherenkov ring might be sources of the systematic error. The contribution from the vertex fitting is estimated to be $\pm 3\%$ by comparing results of two different fitting algorithms. The contribution from the directional fitting is estimated to be $\pm 2\%$ by changing the total momentum cut (criterion (F)) by ± 15 MeV/c. This 15 MeV/c momentum invalance roughly corresponds to changing the ring direction by 2°. Finally, the contribution from the opening angle is estimated to be $\pm 4\%$ by changing the total momentum cut (criterion (F)) by ± 30 MeV/c. The change of the opening angle affects ring separation and therefore affect reconstructed momentum for multi-ring events. This 30 MeV/c error is estimated by changing the reconstructed opening angle by 2° and re-reconstructing the total momentum with the shifted opening angle. In total, the contribution from the possible fitting biases is estimated to be $\pm 7\%$.

Next, systematic uncertainties in the exposure are estimated. The accuracy of the detector size must be within a few cm in each dimension and it may contributes the uncertainty of the exposure by <1%. The livetime is calculated from the 48bit clock counter information recorded in TRG module. The uncertainty of the observed livetime is estimated by comparing the clock counter with another clock counter to be <0.1%.

In summary, each estimated uncertainty are listed in Table 9–5. The total uncertainty in the detection efficiency is 18%. The uncertainty in the exposure is <1% and negligible.

9.4.1 Limit Calculation by Bayesian Statistics

In section 9.3.1, simple limit calculation using Poisson distribution is performed. In the calculation, systematic uncertainties of quantities of exposure, detection efficiency, and the number of background are assumed to be negligible. In this section, the uncertainties associated with these quantities are included in the limit calculation by employing a Bayesian method [84] (for details, see [85]).

In the counting experiments, the probability to detect n events follows the Poisson distribution.

$$\mathbf{P}(n|\Gamma\lambda\epsilon b) = \frac{e^{-(\Gamma\lambda\epsilon+b)}(\Gamma\lambda\epsilon+b)^n}{n!} \tag{9-3}$$

where Γ is the event rate (proton decay rate for us), λ is exposure, ϵ is efficiency, and b is the number of background. $\mathbf{P}(A|B)$ represents the probability of proposition A, given that proposition B is true.

Applying Bayes' theorem allows us to write:

$$\mathbf{P}(\Gamma\lambda\epsilon b|n)\mathbf{P}(n) = \mathbf{P}(n|\Gamma\lambda\epsilon b)\mathbf{P}(\Gamma\lambda\epsilon b). \tag{9-4}$$

Because quantities $\Gamma, \lambda, \epsilon, b$ are independent, $\mathbf{P}(\Gamma\lambda\epsilon b)$ can be disintegrated.

$$\mathbf{P}(\Gamma\lambda\epsilon b) = \mathbf{P}(\Gamma)\mathbf{P}(\lambda)\mathbf{P}(\epsilon)\mathbf{P}(b) \tag{9-5}$$

Desired quantities of probability density function of Γ can be obtained by:

$$\mathbf{P}(\Gamma|n) = \int\int\int \mathbf{P}(\Gamma\lambda\epsilon b|n)d\lambda d\epsilon db. \tag{9-6}$$

By combining Equation (9-3), (9-4), (9-5), and (9-6), we obtain:

$$\mathbf{P}(\Gamma|n) = A\int\int\int \frac{e^{-(\Gamma\lambda\epsilon+b)}(\Gamma\lambda\epsilon+b)^n}{n!}\mathbf{P}(\Gamma)\mathbf{P}(\lambda)\mathbf{P}(\epsilon)\mathbf{P}(b)d\lambda d\epsilon db. \tag{9-7}$$

The normalization factor A is resolved by demanding $\int_0^\infty \mathbf{P}(\Gamma|n)d\Gamma = 1$. $\mathbf{P}(\Gamma), \mathbf{P}(\lambda), \mathbf{P}(\epsilon), \mathbf{P}(b)$ are prior probability density functions (priers) and they enable us to include systematic uncertainties in the limit calculation. Using the $\mathbf{P}(\Gamma|n)$, we can calculate the upper limit of the decay rate Γ^{limit} by

$$CL = \int_0^{\Gamma^{\mathrm{limit}}} \mathbf{P}(\Gamma|n)d\Gamma. \tag{9-8}$$

The lifetime limit is the inverse of Γ^{limit}.

In this method, the priors for the exposure $\mathbf{P}(\lambda)$ and detection efficiency $\mathbf{P}(\epsilon)$ are taken as Gaussian distributions, truncated to disallow unphysical regions.

$$\mathbf{P}(\lambda) \propto \begin{cases} e^{-(\lambda-\lambda_0)^2/2\sigma_\lambda^2} & \lambda > 0 \\ 0 & \text{otherwise} \end{cases} \tag{9-9}$$

$$\mathbf{P}(\epsilon) \propto \begin{cases} e^{-(\epsilon-\epsilon_0)^2/2\sigma_\epsilon^2} & 0 < \epsilon < 1 \\ 0 & \text{otherwise} \end{cases} \tag{9-10}$$

The values of σ_λ and σ_ϵ are taken from Table 9–5.

The background prior $\mathbf{P}(b)$ is taken to be a convolution of Poisson and Gaussian distributions in order to account for both the statistical uncertainty of a finite background MC sample size and the systematic uncertainty in the atmospheric neutrino fluxes and cross sections used in the background MC sample.

$$\mathbf{P}(b) \propto \int_0^\infty \frac{e^{-b^{\text{MC}}}(b^{\text{MC}})^{n_b}}{n_b!} e^{-\frac{(bC-b^{\text{MC}})^2}{2\sigma_b^2}} db^{\text{MC}} \tag{9-11}$$

where

n_b	MC events passing through proton decay criteria.
b^{MC}	true mean MC events passing through proton decay criteria.
C	MC oversampling factor.
σ_b	uncertainty due to neutrino fluxes and cross sections.

It should be noticed, however, that due to zero observed candidates, our limit calculation result is almost independent on the details of $\mathbf{P}(b)$.

Finally, the prior for the decay rate $\mathbf{P}(\Gamma)$ is taken to be uniform. This corresponds to the uniform prior implicitly used in simple Poisson limits [86].

$$\mathbf{P}(\Gamma) \propto \begin{cases} 1 & \Gamma > 0 \\ 0 & \text{otherwise} \end{cases} \tag{9-12}$$

By performing the integration of Equation (9-7) and (9-8), the upper limit of the decay rate Γ^{limit} is obtained. The resulting limit on the partial lifetime for $p \to e^+\pi^0$ is found to be:

$$\tau/B_{p\to e^+\pi^0} > 2.0 \times 10^{33} \text{ years (90\% CL).} \tag{9-13}$$

Comparing with the limit from the simple Poisson calculation (section 9.3.1), it is found that the lifetime limit is changed by only $\sim 5\%$ even if systematic uncertainties are taken into account.

10 Conclusion

In this thesis, proton decay search via $p \to e^+\pi^0$ mode was performed using 32.9 kton·year exposure (535 live-days) of Super–Kamiokande data. While the detection efficiency was 44% and estimated number of backgrounds caused by atmospheric neutrino interactions was 0.1 events in this exposure, there was no candidate events which survived the proton decay selection criteria. Observed contained events were well explained by expected atmospheric neutrino backgrounds. Therefore, I concluded that no evidence of the proton decay in the mode $p \to e^+\pi^0$ was observed. From the data, stringent partial lifetime limit of the proton has been set to be:

$$\tau_p/B_{p\to e^+\pi^0} > 2.0 \times 10^{33} \text{ years (90\% CL)},$$

which should be compared with the previous experimental results, 8.5×10^{32} years [7].

Several GUT models predict the decay rate of $p \to e^+\pi^0$ within observable range of this exposure of Super–Kamiokande data. For example, flipped $SU(5)$ model predicts the partial lifetime of the proton as:

$$\tau_p/B_{p\to e^+\pi^0} = 3 \times 10^{31-37} \text{ years [13]}.$$

On the other hand, $SO(10)$ model also admits relatively short lifetime. Especially, $SO(10)$ GUT model with the left-right symmetric intermediate symmetry of $SU(4) \otimes SU(2)_L \otimes SU(2)_R$ predicts partial lifetime of $p \to e^+\pi^0$ mode as:

$$\tau_p/B_{p\to e^+\pi^0} = 1.44 \times 10^{32.1\pm0.7\pm1.0\pm1.9} \text{ years [15, 26]}.$$

Although the new experimental limit cannot exclude these models, this can give restrictions to parameters in these models. In minimal SUSY $SU(5)$ model, predicted partial lifetime of protons via $p \to e^+\pi^0$ mode is long as $\sim 10^{34-38}$ years [28, 29, 30] and theoretical lower limit is obtained as:

$$\tau_p/B_{p\to e^+\pi^0} > 4.1 \times 10^{33} \text{ years [28]}.$$

Therefore, the new experimental limit is close to the edge of the theoretical prediction. The Super–Kamiokande sensitivity will reach to the prediction soon.

Because the background level is very low for the $p \to e^+\pi^0$ mode, Super–Kamiokande will have sensitivity for longer proton lifetime in future. Figure 10–1 shows the Super–Kamiokande detector sensitivity for the $p \to e^+\pi^0$ search. In the figure, expected sensitivities for the partial lifetime at 90% CL and 99.7% CL (3σ) are shown as a function of detector exposure. In ten years, we will reach to 10^{34} years of the partial lifetime at 90% CL. I'm looking forward to the evidence for proton decays in future Super–Kamiokande data.

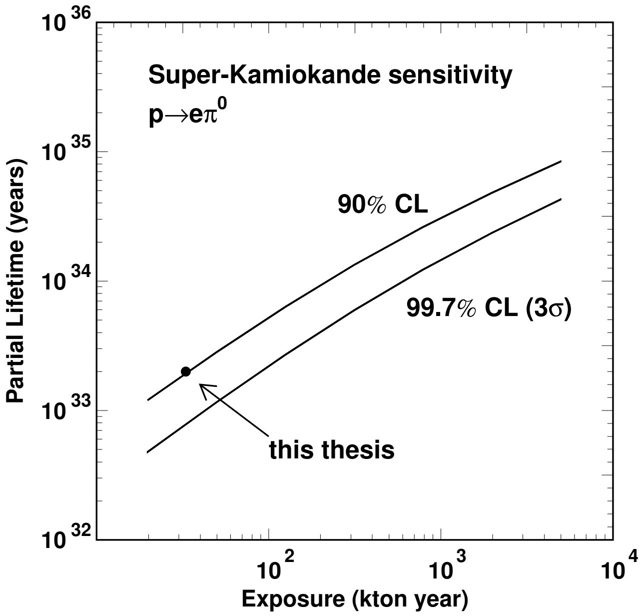

Figure 10–1: The Super–Kamiokande detector sensitivity for the $p \to e^+\pi^0$ search. Expected sensitivities for the partial lifetime at 90% CL and 99.7% CL (3σ) are shown as a function of detector exposure. The confidence level is calculated by simple Poisson distribution (Equation (9-1) and (9-2)). The point shows the result of this thesis.

Appendices

A Details of Reconstruction

A.1 Vertex Fitter

The reconstruction procedure starts from the vertex fitting. The vertex position is estimated by finding the position at which the timing residual ((photon arrival time)−(time of flight)) distribution is most peaked. Because the number of rings has not yet estimated at this point, this vertex fitter searches for the vertex position with single ring assumption. Actually, this vertex fitting algorithm consists of following three steps.

(a) Point Vertex Fitter roughly estimate vertex position.

(b) Ring Edge Finding find an edge of a Cherenkov ring.

(c) Precise Vertex Fitter precisely reconstruct vertex position using the information from (a) and (b).

Using roughly estimated vertex position in (a), Cherenkov edge position is determined in (b). In precise vertex fitting (c), we take into account the track length of the particle and scattered light as well as direct (non-scattered) light to calculate the time of flight of Cherenkov photons. These three steps are described below.

A.1.1 Point Vertex Fitter

The name of "Point Vertex Fitter" refers to the fitter which is performed with the assumption of one point-like light source. This means that the all Cherenkov light is assumed to be emitted from one point at the same time and the track length of the charged particle is neglected. The principle of the fitter is that the timing residual ((photon arrival time)−(time of flight)) distribution should be most peaked with the correct vertex position. In Figure A–1, the time of flight (TOF) subtracted TDC distributions are shown with (a) true vertex position and (b) wrong position 4 m off from the true vertex position. With the true vertex, the residual time distribution has a sharp peak as shown in Figure A–1–(a). The finite width of the distribution comes from the time resolution of the PMTs. The long tail is made by scattered light and reflected light from the detector wall. On the other hand, with the wrong vertex position, the residual time becomes a wide distribution as shown in Figure A–1–(b).

To find the vertex position, we define the estimator G_p as

$$G_p = \frac{1}{N}\sum_i \exp\left(-\frac{t'_i - t_0}{2(<\sigma> \times 1.5)^2}\right) \qquad \text{(A-1)}$$

where N is the number of fired inner PMTs, t'_i is TOF subtracted timing of i-th PMT, and $<\sigma>$ is typical timing resolution of the PMT and we take $<\sigma>= 2.5$ nsec. We choose t_0

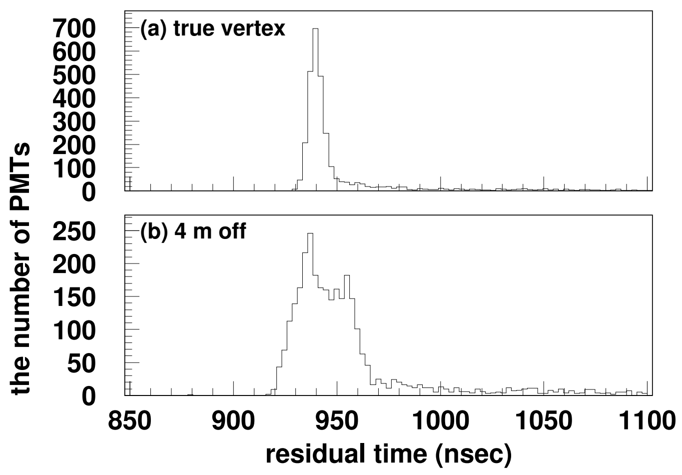

Figure A–1: The residual time distributions after TOF subtraction for a $p \to e^+\pi^0$ Monte Carlo event. The time of flight is calculated with (a) true vertex position and (b) 4 m off from the true vertex position. With the true vertex, the residual time distribution has a sharp peak.

so that G_p takes maximum value. We subtract TOF as

$$t'_i = t_i - \frac{n(q_i, l_i)}{c} \times |\vec{P_i} - \vec{O}| \tag{A-2}$$

where t_i is the timing of the i-th PMT and $\vec{P_i}$ and $\vec{O}$ are position of the i-th PMT and the estimated vertex position, respectively. Here, refractive index $n(q_i, l_i)$ is taken as a function of detected p.e. q_i and photon travel length $l_i(= |\vec{P_i} - \vec{O}|)$ in order to take into account the wavelength dependence of the light velocity in water (Figure 4–21). Because timing information of a PMT is determined only by a first detected photon, the timing information has dependence on the amount of detected p.e.s ($=q_i$). Moreover, because the spectrum of Cherenkov photons are distorted in propagating in water, the timing also has dependence on the traveling distance ($=l_i$). Figure A–2 shows the probable refractive index as a function of the detected p.e.s and the traveling distance which determines the light velocity in TOF subtraction.

By changing estimated vertex $\vec{O}$, the fitter searches for the vertex position with which G_p takes maximum value. The final estimated vertex $\vec{O_0}$ is the output of this step.

Using the estimated vertex position $\vec{O_0}$, ring direction is also roughly estimated by summing up the detected p.e. vector.

$$\vec{d_0} = \sum_i q_i \times \frac{\vec{P_i} - \vec{O_0}}{|\vec{P_i} - \vec{O_0}|} \tag{A-3}$$

With the $\vec{O_0}$ and $\vec{d_0}$, the ring edge search is performed in the next step.

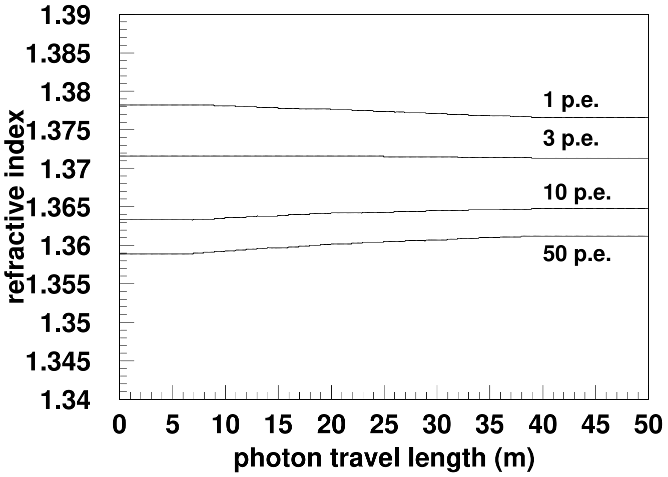

Figure A–2: The effective refractive index used in the vertex fitter. In the vertex fitter, the light velocity is taken as a function of detected p.e.s ($=q$) and travel length of photon ($=l$) and written as $v(q,l) = c/n(q,l)$.

A.1.2 Ring Edge Finding

In this step, edge position of the Cherenkov edge is determined and several PMTs close to the edge are tagged as edge PMTs. These tagged PMTs are used in the next step, precise vertex fitter, to determine the ring direction.

At first, each detected p.e. is filled in histogram as a function of Cherenkov opening angle θ. Here, detected p.e.s are corrected for light attenuation length and PMT acceptance. Figure A–3 shows a typical histogram of the corrected p.e. distribution ($\mathrm{PE}(\theta)$) for a single-ring event. In the histogram of $\mathrm{PE}(\theta)$, the edge position θ_{edge} is determined by the following two conditions.

(a) $\theta_{\mathrm{edge}} > \theta_{\mathrm{peak}}$ — θ_{peak} is opening angle where $\mathrm{PE}(\theta)$ takes maximum.

(b) $\left.\dfrac{d^2PE(\theta)}{d^2\theta}\right|_{\theta=\theta_{\mathrm{edge}}} = 0$ — second derivative should be zero at $\theta = \theta_{\mathrm{edge}}$.

If there are several θ_{edge} which satisfy the condition (a) and (b), the θ_{edge} nearest to θ_{peak} is selected.

To determine the ring direction, the estimator $Q(\theta_{\mathrm{edge}})$ is defined as

$$Q(\theta_{\mathrm{edge}}) = \frac{\int_0^{\theta_{\mathrm{edge}}} \mathrm{PE}(\theta)d\theta}{\sin\theta_{\mathrm{edge}}} \times \left(\left.\frac{d\mathrm{PE}(\theta)}{d\theta}\right|_{\theta=\theta_{\mathrm{edge}}}\right)^2 \times \exp\left(-\frac{(\theta_{\mathrm{edge}}-\theta_{\mathrm{exp}})^2}{2\sigma_\theta^2}\right) \qquad \text{(A-4)}$$

where θ_{exp} and σ_θ are expected opening angle of the Cherenkov ring and its resolution, respectively. $Q(\theta_{\mathrm{edge}})$ is defined so that it takes large value when large number of p.e.s

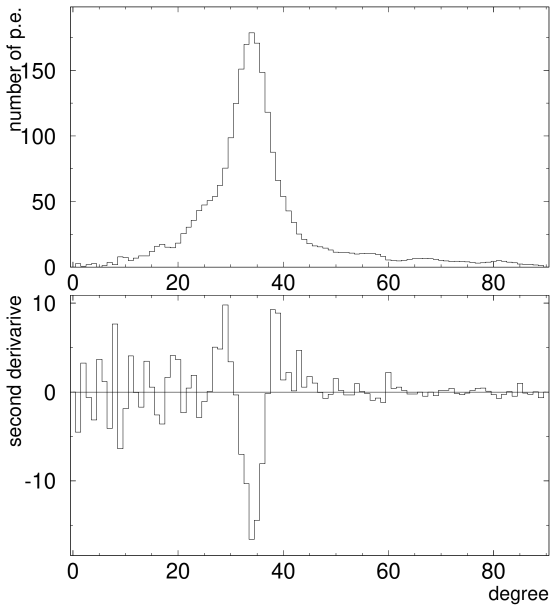

Figure A–3: The typical PE(θ) distribution for a single-ring event. Lower figure shows its second derivative.

is sitting inside of θ_{edge} and the first derivative of PE(θ) is large and θ_{edge} is close to the expected one. By changing the ring direction, best direction which gives maximum value of the estimator Q is searched for. In case of $\theta_{\text{edge}} > 43°$, Equation (A-4) is replaced in the final step by

$$Q(\theta_{\text{edge}}) = \frac{\int_0^{\theta_{\text{edge}}} \text{PE}(\theta) d\theta}{\sin\theta_{\text{edge}}} \times \exp\left(-\frac{(\theta_{\text{edge}} - \theta_{\text{exp}})^2}{2\sigma_\theta^2}\right) \tag{A-5}$$

to correct the ring direction.

Finally, using the determined ring direction and θ_{edge}, PMTs on the Cherenkov ring edge are tagged. These tagged PMTs are used in the next step, precise vertex fitter.

A.1.3 Precise Vertex Fitter

This precise vertex fitter consists of the following three steps.

- determine the ring direction.
- calculate the track length of the charged particle.
- search for the vertex position where fitting estimator takes a maximum value.

These steps are performed iteratively until better position is no longer found.

The differences between the point vertex fitter and the precise vertex fitter are that scattering Cherenkov light and track length of charged particles are carefully taken into account in the precise vertex fitter.

Ring Direction

Here, ring direction is determined using given vertex position. Moreover, tagged PMTs on the Cerenkov edge, which are selected in the ring edge finding step, are used. The ring direction which minimizes the following χ^2 is searched for:

$$\chi^2 = \sum_i \sqrt{q_i} \frac{(\theta_i - < \theta_i >)^2}{\sigma_{\theta_i}} \tag{A-6}$$

where q_i is the detected p.e.s in the i-th tagged PMT and θ_i is the opening angle of the i-th PMT along the estimated ring direction. $< \theta_i >$ is the opening angle averaged over all θ_i. The σ_θ is the resolution of the opening angle and taken to be 70cm$/|\vec{P_i} - \vec{O}|$ where $|\vec{P_i} - \vec{O}|$ is the distance between the vertex position and the i-th PMT. This 70 cm refers to the distance between inner detector PMTs. The summation in the equation is done for all tagged PMTs. With the direction which gives the minimum χ^2, the opening angle of the Cherenkov ring is determined as

$$\theta_c =< \theta_i > \tag{A-7}$$

Track Length

The track length of the charged particle is roughly estimated from the total amount of p.e.s assuming $dE/dx = 3$ MeV/cm. The assumption $dE/dx = 3$ MeV/cm is selected empirically to get best performance of the reconstruction.

Using the estimated total track length L_t, track length l'_i where the Cherenkov photons for the i-th PMT are emitted is determined. As shown in the Figure A–4, the detected p.e.s in i-th PMT are projected onto the particle track, at the position $\vec{X_i}$, where $|\vec{X_i} - \vec{O}|$ is l_i. Here, the opening angle between the ring direction $(\vec{X_i} - \vec{O})$ and projection line $(\vec{P_i} - \vec{X_i})$ is θ_c which is the reconstructed opening angle by Equation (A-6) and (A-7). This projection gives the p.e. distribution $Q(l)$ as a function of l. Using the projection function $Q(l)$, the track length l'_i where the Cherenkov photons for i-th PMT are emitted is estimated as

$$l'_i = \frac{\int_0^{l_i} Q(l)dl}{\int_0^{\infty} Q(l)dl} \times L_t \tag{A-8}$$

In case of $l'_i > l_i$, l'_i is replaced by l_i. This correction is important for electron ring, because the estimated track length L_t for the electron is too long due to electromagnetic showers.

Using the determined l'_i, the residual time of the i-th PMT can be calculated as

$$t'_i = \begin{cases} t_i - \frac{l'_i}{c} - \frac{n}{c} \times |\vec{P_i} - \vec{X'_i}|, & \text{PMTs inside of Cherenkov edge} \\ t_i - \frac{n}{c} \times |\vec{P_i} - \vec{O}|, & \text{PMTs outside of Cherenkov edge} \end{cases} \tag{A-9}$$

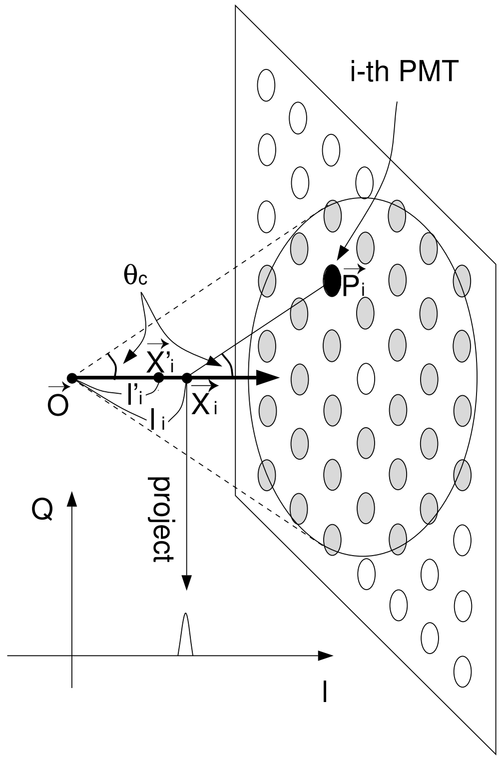

Figure A–4: The p.e. projection along the particle track. The p.e.s of i-th PMT is projected at l_i on the track in order to make charge histogram $Q(l)$. θ_c is reconstructed opening angle of the Cherenkov ring. $\vec{O}$, $\vec{P}_i$, and $\vec{X}_i$ are position vector of vertex, i-th PMT, and projection point for the i-th PMT, respectively. $\vec{E}_i$ is the estimated emit point by Equation (A-8).

where $\vec{X}_i'$ is estimated emitted position for the i-th PMT and $l_i' = |\vec{X}_i' - \vec{O}|$ (Figure A–4). n is the effective refractive index and shown in Figure A–2.

Vertex Position

For the fired PMTs inside of the Cherenkov ring edge, timing information is mainly determined by direct (non-scattered) photons. On the other hand, a significant fraction of the fired PMTs outside of the Cherenkov ring edge detects scattered lights and reflected light on the detector wall. Therefore, we should treat them with different estimators. For the fired PMTs inside of Cherenkov cone, fitting estimator G_I is defined as

$$G_I = \sum_i \frac{1}{\sigma_i^2} G_{\text{direct}}(t_i', t_0) \tag{A-10}$$

where

$$G_{\text{direct}}(t_i', t_0) = \exp\left(-\frac{(t_i' - t_0)^2}{2(<\sigma> \times 1.5)^2}\right) \tag{A-11}$$

Here, σ_i is the timing resolution of the i-th PMT (section 3.3.1) as a function of detected p.e.s (q_i) and $<\sigma>$ is timing resolution for the detected p.e.s averaged over the fired PMTs. t_i' is TOF subtracted timing information of the i-th PMT calculated by Equation (A-9).

For the PMTs outside of the Cherenkov edge, the t_0 is corrected in order to take into account the late arrival timing of light as

$$t_0' = t_0 + \sigma_i \times (1.5 \times R_q - 0.7)^2 \tag{A-12}$$

where R_q is the fractional p.e.s detected within the Cherenkov ring

$$R_q = \frac{\sum\limits_{\theta<\theta_c+3} q_i}{\sum\limits_{\theta<70^\circ} q_i} \tag{A-13}$$

For the PMTs outside of the Cherenkov edge with $t_i' \leq t_0'$, estimator is defined as

$$G_{O1} = \sum_i \frac{1}{\sigma_i^2}(G_{\text{direct}}(t_i', t_0') \times 2 - 1) \tag{A-14}$$

and for the PMTs outside of the Cherenkov edge with $t_i' \geq t_0'$,

$$G_{O2} = \sum_i \frac{1}{\sigma_i^2}(\max[G_{\text{direct}}(t_i', t_0'), G_{\text{scatter}}(t_i', t_0')] \times 2 - 1) \tag{A-15}$$

where

$$G_{\text{scatter}}(t_i', t_0') = \frac{R_q}{1.5^2} \times G_{\text{direct}}(t_i', t_0') + (1 - \frac{R_q}{1.5^2}) \times \exp(-\frac{t_i' - t_0'}{60\text{nsec}}) \tag{A-16}$$

By summing up the estimators, fitting estimator is defined as

$$G = \frac{G_I + G_{O1} + G_{O2}}{\sum_i \frac{1}{\sigma_i}} \tag{A-17}$$

Here $t_0(t'_0)$ is selected at each vertex position so that the estimator G takes maximum value. The vertex position which maximizes the estimator G is regarded as the reconstructed vertex position. Numerical factors in the estimators above are selected empirically to get best performance of the reconstruction.

A.2 Ring Fitter

After reconstruction of the vertex position and one dominant ring direction, other possible rings are looked for and probable rings are reconstructed in this ring fitter. Using the reconstructed ring(s), we can reconstruct the total momentum and total invariant mass of $p \to e^+\pi^0$ events and those of atmospheric neutrino events. Actually, this ring fitting algorithm consists of following two steps.

(a) Ring Candidate Selection — select possible ring candidates.

(b) Ring Candidate Test — check the ring candidates by a likelihood method. If there is a candidate which satisfies conditions, the ring is regarded as a true ring and go back to (a) to search for other rings.

Starting from one ring reconstructed by the vertex fitter, a second ring is looked for in the step (a) and (b). If a probable second ring is found and regarded as a true ring, the program goes back to step (a) to look for a third ring. This iteration is performed up to 4 times (fifth ring) until no more probable ring is found. The step (a) and (b) are explained below.

A.2.1 Ring Candidate Selection

We use a known technic for a pattern recognition, Hough transformation [77], to search for possible ring candidates. The essence of the Hough transformation is shown in Figure A–5. Suppose there are four fired PMTs on the unknown ring (radius r) and we want to find the center of the ring (left figure). By Hough transformation, the detected p.e.s are mapped to a circle with radius r centered on the PMT. All mapped circles cross at the center of the unknown ring. By accumulating the mapped circles, we can find the peak in the Hough space, giving the center of the unknown ring.

Before the mapping, the p.e. contributions from the rings which already have been regarded as true rings are subtracted in order to enhance the capability of the ring finding. In the ring fitter, the Hough space is made from 2-dimensional arrays divided by polar angle Θ (36 bins) and azimuthal angle Φ (72 bins), resulting in 36×72 pixels. These angles are measured from the reconstructed vertex. Detected p.e.s in each fired PMT, which are

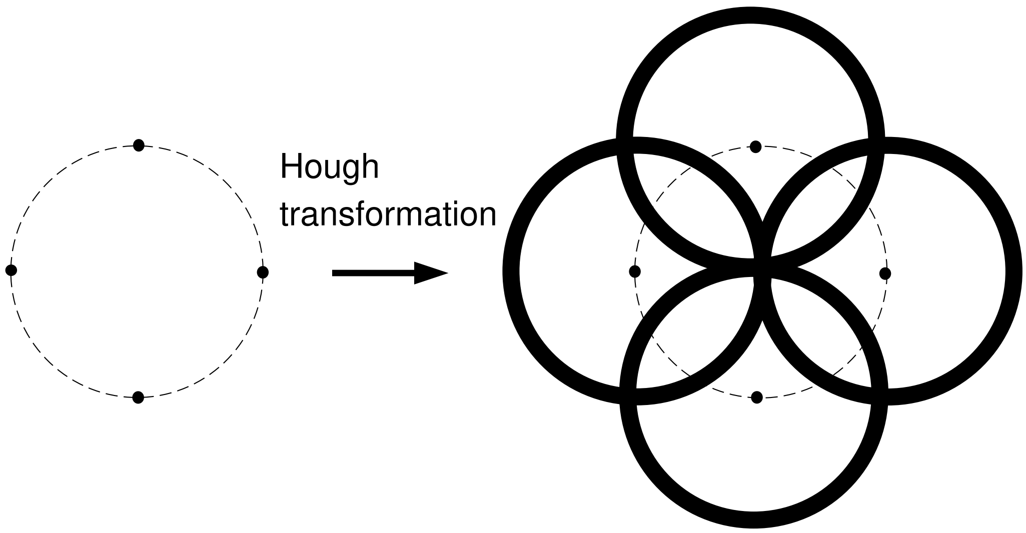

Figure A–5: The Hough transformation. Suppose there are four fired PMTs on the unknown ring (radius r) and we want to find the center of the ring (left figure). By Hough transformation, the detected p.e.s are mapped to a circle with radius r centered on the PMT. All mapped circles cross at the center of the unknown ring. By accumulating the mapped circles, we can find the peak in the Hough space, giving the center of the unknown ring.

corrected for acceptance and attenuation length, are mapped to pixels (Θ_i, Φ_i) for which the opening angle toward the PMT is 42°. In the actual case, a Cherenkov ring in the Super–Kamiokande detector has a broad p.e. distribution rather than an ideal thin circle. In order to take into account the actual p.e. distribution, the expected p.e. distribution for a 500 MeV/c electron as a function of opening angle θ is used as a weight in the p.e.s mapping. Namely, the corrected p.e.s of a fired PMT are mapped to pixels (Θ_i, Φ_i), for which the opening angles toward the PMT are θ, with weight of expected p.e.s $Q_e(\theta)$. The expected p.e. distribution $Q_e(\theta)$ is shown in Figure A–6.

Peaks found in the Hough space are identified as centers of possible ring candidates. However, ring candidate for which the direction is very close to one of the true ring directions (opening angle $< 15°$) is discarded as a fake candidate made by the true ring. In order to take into account different Cherenkov opening angles for non-electron particles and limited accuracy of the reconstructed vertex, the Hough transformation is performed with $Q_e(\theta)$ which peak position (Cherenkov ring edge) is slidden. The slidden peak position which makes most sharp peak in the Hough space is regarded as the opening angle of the candidate ring.

One example of p.e. distribution in the Hough space is shown in Figure A–7. In making the figure, p.e. subtraction for the true ring (first ring) is omitted. We can find a second clear peak which should be identified as a center of the second ring candidate.

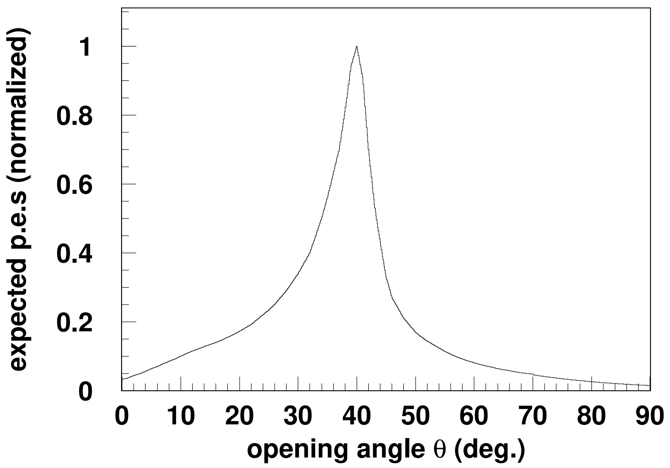

Figure A–6: The expected p.e. distribution for a 500 MeV/c electron.

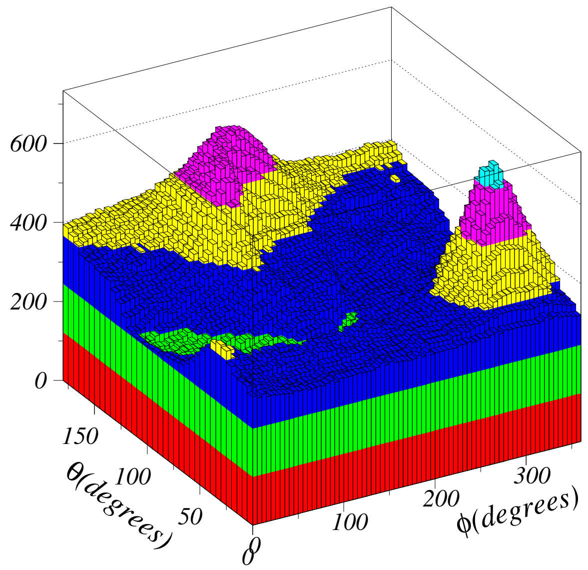

Figure A–7: The transformed p.e. distribution in the Hough space. In making the figure, p.e. subtraction for the true ring (first ring) is omitted. We can find a second clear peak which should be identified as a center of the second ring candidate.

A.2.2 Ring Candidate Test

The ring candidates selected by the Hough space are checked by a likelihood method to determine whether the ring is probable or not. The likelihood is defined to evaluate the probability to observe the p.e. distribution with expected p.e. distribution. To calculate the probability for multi-ring events, we need to understand the p.e. contribution from each ring. Because we only observe the total p.e.s of each PMT which comprise of contributions from several rings, we need to separate the total p.e.s of each PMT into contributions from each ring. This process, called as "ring separation", is explained in appendix A.4.1.

Given N already found rings and a $(N+1)$-th ring candidate, the ring fitter checks the likelihood value to determine whether the ring candidate is a true ring or not. The ring fitter calls the ring separation and utilizes the likelihood function similar to Equation (A-35). At first, assuming the existence of the $(N+1)$-th ring, the likelihood function L^{N+1} is calculated as

$$L^{N+1} = \sum_{i}^{\exists n \in (N+1),\ \theta_{i,n} < 1.2\theta_n^c} \log\left(prob(q_i, \sum_{n}^{N+1} \alpha_n \cdot q_{i,n}^{\exp}) \right) \tag{A-18}$$

where the summation of the likelihood is performed for the i-th PMT for which the opening angle towards at least one of $(N+1)$ ring directions is smaller than its opening angle times 1.2. The q_i is the observed number of p.e.s in the i-th PMT and $\alpha_n \cdot q_{i,n}^{\exp}$ is the expected p.e.s for the i-th PMT given by the n-th ring. The probability $prob$ is defined in Equation (A-36). For the calculation of the likelihood, the expected p.e.s given by the $(N+1)$-th ring is calculated using the electron distribution shown in Figure A–6. For other true rings, expected p.e.s are iteratively optimized using the observed p.e.s (see appendix A.4.1). By optimizing the α_n's, the program looks for the best α_n's which give the maximum value of L^{N+1}.

After that, the likelihood value is calculated again with N ring assumption. Namely, the expected p.e.s for $(N+1)$-th ring are not considered in the calculation as

$$L^{N} = \sum_{i}^{\exists n \in (N+1),\ \theta_{i,n} < 1.2\theta_n^c} \log\left(prob(q_i, \sum_{n}^{N} \alpha_n \cdot q_{i,n}^{\exp}) \right) \tag{A-19}$$

where the summation of the likelihood is performed again for the exactly same PMTs used in Equation (A-18). By optimizing only $\alpha_n (1 \leq n \leq N)$ and fixing all $q_{i,n}^{\exp} (1 \leq n \leq N)$, maximum value for the L^N is looked for.

In principle, we always obtain $L^{N+1} \geq L^N$ because we can make the L^{L+1} value to be $L^{N+1} = L^N$ by setting α_{N+1} to be zero. However, there is a constraint of a lower momentum limit for the $(N+1)$-th ring and it disables the α_{N+1} to be zero. Therefore, it enables us to obtain $L^{N+1} \leq L^N$ for some of ring candidates. In case of $L^{N+1} \leq L^N$, the ring candidate is rejected because the (N+1)-th ring candidate is less likely to be a real Cherenkov ring.

For the candidate ring which satisfies $L^{N+1} \geq L^N$, following evaluation functions are calculated.

F_1 — $(L^{N+1} - L^N)$ is corrected for the total p.e.s. When the difference $(L^{N+1} - L^N)$ is large, the candidate is probable.

F_2 For the PMTs around the edge of the candidate ring, the assigned p.e.s to the candidate ring are summed up. This summation is performed only for PMTs sitting at non-overlapping region of Cherenkov rings. When the averaged assigned p.e.s Q^{edge} is large, the candidate is probable.

F_3 For the PMTs outside of the candidate ring, the assigned p.e.s to the candidate ring are summed up. This summation is also performed only for PMTs sitting at non-overlapping region of Cherenkov rings. The averaged p.e.s Q^{out} should be smaller than the averaged p.e.s Q^{edge}, which is calculated for the F_2. The difference $(Q^{\mathrm{edge}} - Q^{\mathrm{out}})$ is corrected for total p.e.s and the opening angle towards other rings. When the difference is large, the candidate is probable.

F_4 By the ring separation with the N ring assumption, we calculate the residual p.e.s for each PMT as $q_i^{\mathrm{res}} = q_i - \sum_{n'} q_{i,n'}^{\mathrm{exp}}$. The total amount of residual p.e.s is calculated as $|\sum_i q_i^{\mathrm{res}}(\vec{P}_i - \vec{O})|$, where $\vec{P}_i$ and $\vec{O}$ are position vector of the i-th PMT and the vertex position, respectively. Correction for total p.e.s is performed. When the total amount of residual p.e.s is large, the candidate is probable.

By calculating the product of F_1, F_2, F_3, and F_4 with some optimizing weights, we get the final evaluate function F for the candidate ring. By the F, the ring fitter determines whether the candidate is true or not. If all candidate rings are regarded as false, ring fitter stops, giving the reconstructed N rings. If a candidate ring which satisfies the condition is found, the ring is regarded as a $(N+1)$-th true ring and the ring fitter goes back to the ring candidate selection (appendix A.2.1) in order to look for a $(N+2)$-th ring.

A.3 Particle Identification

The program "particle identification" determines the particle type of each ring using its Cherenkov ring pattern and opening angle. Each ring is classified as a showering particle $(e^{\pm}, \gamma)$ or a nonshowering particle $(\mu^{\pm}, \pi^{\pm})$. The showering (nonshowering) particles are sometimes called e-like (μ-like). To identify the particle type, we start from "ring separation" (appendix A.4.1) to get the observed p.e. distribution given by each ring and its expected p.e. distribution. The examples of the separated p.e. distributions are shown in Figure A–10 and A–11 for the $p \to e^+\pi^0$ event. After the ring separation, the observed p.e.s are compared with expected p.e. distributions of an electron particle and a muon particle. One of two particle types which better reproduces the observed p.e. distribution is selected as a reconstructed particle type.

A.3.1 Expected p.e. Distribution for Electrons

Using the Super–Kamiokande Monte Carlo simulation, we make the expected p.e. distribution for electron events. On hypothetical spherical surface with radius $R^{\mathrm{sph}} = 16.9\mathrm{m}$, the expected p.e. distribution is calculated as a function of opening angle θ towards the ring direction. Actually, the expected p.e.s $Q^{\text{exp}}(\theta, p)$'s are tabulated for electron momentum of $p = 100$ MeV/c, $p = 300$ MeV/c, and $p = 1000$ MeV/c. Necessary interpolation is performed in the particle identification to obtain the desired $Q^{\text{exp}}(\theta, p)$ for the observed total p.e.s of the ring.

Using the $Q^{\text{exp}}(\theta, p)$, expected p.e.s for the i-th PMT is calculated as

$$q_{i,n}^{\text{direct}}(e) = \alpha_n(e) \times Q_n^{\text{exp}}(\theta_{i,n}, p_n) \times (\frac{R^{\text{sph}}}{r_i})^{1.5} \times \frac{1}{\exp(r_i/L)} \times f(\Theta_i^{\text{PMT}}) \tag{A-20}$$

where

$q_{i,n}^{\text{direct}}(e)$	expected p.e.s for i-th PMT and n-th ring assuming the particle is an electron
$\alpha_n(e)$	normalization factor
$\theta_{i,n}$	opening angle of the i-th PMT towards the n-th ring direction
R^{sph}	radius of the hypothetical sphere, 16.9 m
L	attenuation length for the event sample (see section 3.3.5)
r_i	distance from the vertex to the i-th PMT
$f(\Theta_i^{\text{PMT}})$	effective cross section of a PMT as a function of the incident angle Θ^{PMT} (Figure 6–9)

The factor $(R^{\text{sph}}/r_i)^{1.5}$ corrects for the diffusion of Cherenkov light.

A.3.2 Expected p.e. Distribution for Muons

For muons, we can analytically calculate the expected p.e. distribution as

$$q_{i,n}^{\text{direct}}(\mu) = \left(\alpha_n(\mu) \times \left(r_i(\sin\theta_{x_{i,n}} + r_i \cdot \left.\frac{d\theta}{dx}\right|_{x=x_{i,n}}) \right)^{-1} \times \sin^2\theta_{x_{i,n}} + q_{i,n}^{\text{knock}} \right) \times \frac{1}{\exp(r_i/L)} \times f(\Theta_i^{\text{PMT}}) \tag{A-21}$$

where

$q_{i,n}^{\text{direct}}(\mu)$	expected p.e.s for the i-th PMT and n-th ring assuming the particle is a muon
$\alpha_n(\mu)$	normalization factor
x	distance between the vertex point and muon position along the muon trajectory
$x_{i,n}$	distance between the vertex point and Cherenkov emission point estimated for the i-th PMT and n-th ring

θ Cherenkov opening angle of the muon traversing at x. The energy loss of the muon is taken into account.

$\theta_{x_{i,n}}$ Cherenkov opening angle of the muon traversing at $x = x_{i,n}$.

In the equation, $\sin^2\theta$ comes from the Cherenkov angle dependence of the Cherenkov photon intensity (Equation (3-3)). The second term $r_i(\sin\theta + r_i(d\theta/dx))$ comes from the cross section of the area where Cherenkov photons are emitted to. As shown in Figure A–8, when a muon traverses dx with changing the Cherenkov opening angle θ due to the ionization loss, the Cherenkov photons are emitted to the area $2\pi r \sin\theta(dx\sin\theta + rd\theta)$. To correct the photon density, we use the term $r_i(\sin\theta + r_i(d\theta/dx))$. The $q_{i,n}^{\mathrm{knock}}$ is the expected number of p.e.s from knock-on electrons which is estimated using the Monte Carlo simulation.

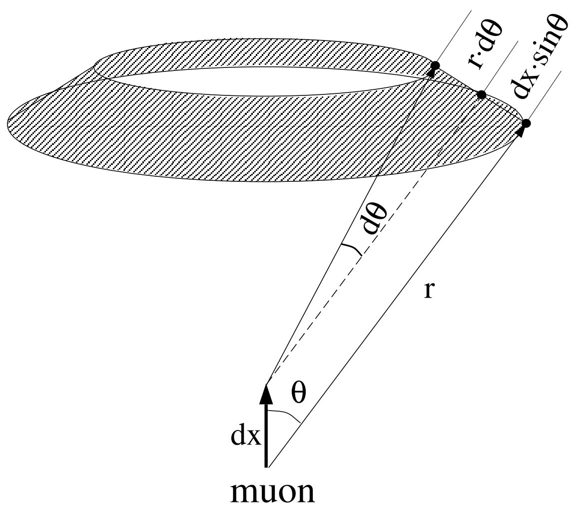

Figure A–8: The cross section of the area where Cherenkov photons are emitted to. When a muon traverses dx with changing the Cherenkov opening angle θ due to the ionization loss, the Cherenkov photons are emitted to the hatched area and its cross section is $2\pi r \sin\theta(dx\sin\theta + rd\theta)$.

A.3.3 Expected p.e. Distribution for Scattered Light

From the timing information of the observed p.e.s, we distinguish the PMTs fired with direct photons and scattered photons. Given the peak position t_0 in the TOF subtracted timing distribution, we identify the direct photons and scattered photons as

$$\begin{aligned} t_0 - 30\mathrm{nsec} < t_i < t_0 + 2\sigma_i + 5\mathrm{nsec} &\rightarrow \text{direct photons} \\ t_0 + 2\sigma_i + 5\mathrm{nsec} < t_i &\rightarrow \text{scattered photons} \end{aligned} \tag{A-22}$$

where t_i is the TOF subtracted timing of the i-th PMT and σ_i is the measured timing resolution as a function of observed p.e.s (Figure 3–14). Using the result of Equation (A-22), expected p.e.s from the scattered lights $q_{i,n}^{\text{scatter}}$ is estimated. Finally, expected p.e.s for an electron and a muon are calculated as

$$q_{i,n}^{\text{exp}}(e \text{ or } \mu) = q_{i,n}^{\text{direct}}(e \text{ or } \mu) + q_{i,n}^{\text{scatter}} \tag{A-23}$$

A.3.4 Estimator for Particle Identification

In general, we have N rings in a single event to be applied particle identification. At first, the particle identification determines the particle type of the first ring and next determines the second ring, the third ring, and so on until it terminates with N-th ring. When we determine the particle type of the n-th ring, the expected p.e. distributions for the n-th ring are calculated from Equation (A-20), (A-21), and (A-23). For other rings, expected p.e.s are calculated by "ring separation" (appendix A.4.1). In the ring separation, the expected p.e.s for these rings are calculated using the observed p.e. distribution. Therefore, we use

$q_{i,n}^{\text{exp}}(e),\ q_{i,n}^{\text{exp}}(\mu)$	calculated from Equation (A-20), (A-21), and (A-23) with an assumption of the particle type.
$q_{i,n'}^{\text{exp}}\ \ (n' \neq n)$	calculated by ring separation without any assumption of the particle type.

where n is the ring number for which program determines the particle type. The probability function is defined to evaluate the observed p.e. distribution as

$$PROB_{i,n}(e \text{ or } \mu) = \begin{cases} prob(q_i, q_{i,n}^{\text{exp}}(e \text{ or } \mu) + \sum\limits_{n' \neq n} q_{i,n'}^{\text{exp}}), & \text{direct photons} \\ prob(0, q_{i,n}^{\text{direct}}(e \text{ or } \mu) + \sum\limits_{n' \neq n} q_{i,n'}^{\text{exp}}) & \\ \qquad \times\, prob(q_i, q_{i,n}^{\text{scatter}} + q_i - q_{i,n}), & \text{scattered photons} \end{cases} \tag{A-24}$$

where $prob(q_{\text{obs}}, q_{\text{exp}})$ is defined in Equation (A-36) and $q_{i,n}$ is the separated p.e.s for the i-th PMT from the n-th ring calculated by the ring separation (see appendix A.4.1). Using the probability $PROB_{i,n}$ the following likelihood is calculated for the electron and muon assumptions.

$$L_n(e \text{ or } \mu) = \prod_{\theta_{i',n} < (1.5 \times \theta_n^c)} PROB_{i',n}(e \text{ or } \mu) \tag{A-25}$$

Here $L_n(e)$ is calculated using the electron expectation $q_{i,n}^{\text{exp}}(e)$ and $L_n(\mu)$ is calculated using the muon expectation $q_{i,n}^{\text{exp}}(\mu)$. The product in the equation is performed for the i-th PMTs whose opening angle $\theta_{i,n}$ is within 1.5 times the Cherenkov opening angle. Optimizations of $q_{i,n}^{\text{exp}}(e)$ and $q_{i,n}^{\text{exp}}(\mu)$ are performed by changing the direction and the Cherenkov opening angle in order to get maximum likelihood $L_n(e)$ and $L_n(\mu)$. The ring direction and Cherenkov opening angle which make the likelihood maximum are used for the proton decay analysis.

In order to combine the above likelihood with another estimator which uses the Cherenkov opening angle, the likelihood is transformed into the χ^2 distribution as

$$\chi^2_n(e \text{ or } \mu) = \frac{1}{\log_{10} e} \times (-\log_{10} L_n(e \text{ or } \mu)) - \text{constant} \tag{A-26}$$

Using the $\chi^2_n(e)$ and $\chi^2_n(\mu)$, probabilities from the Cherenkov pattern are calculated as

$$P_n^{\text{pattern}}(e \text{ or } \mu) = \exp\left(-\frac{1}{2}\left(\frac{\chi^2_n(e \text{ or } \mu) - \chi^2_{min}}{\sigma_{\chi^2_n}}\right)^2\right) \tag{A-27}$$

where $\chi^2_{min} = \min[\chi^2_n(e), \chi^2_n(\mu)]$ and $\sigma_{\chi^2_n}$ is calculated from the degree of freedom as $\sigma_{\chi^2_n} = \sqrt{2N_D}$ where N_D is the number of PMTs used in Equation (A-25).

Moreover, another probability is defined using only the Cherenkov opening angle. Given the reconstructed opening angle as $\theta^c_n \pm \delta\theta_n$, the probability is calculated as

$$P_n^{\text{angle}}(e \text{ or } \mu) = \text{constant} \times \exp\left(-\frac{1}{2}\left(\frac{\theta^c_n - \theta^{\text{exp}}_n(e \text{ or } \mu)}{\delta\theta_n}\right)^2\right) \tag{A-28}$$

where $\theta^{\text{exp}}_n(e)$ and $\theta^{\text{exp}}_n(\mu)$ are the expected Cherenkov opening angle for an electron and muon, respectively, calculated from estimated ring momentum using the detected p.e.s. Using the probability from the pattern and the probability from the angle, total probability is defined as

$$P_n(e) = P_n^{\text{pattern}}(e) \times P_n^{\text{angle}}(e) \tag{A-29}$$

$$P_n(\mu) = P_n^{\text{pattern}}(\mu) \times P_n^{\text{angle}}(\mu) \tag{A-30}$$

For a single-ring event, when $P_1(e) > P_1(\mu)$ ($P_1(e) < P_1(\mu)$), the ring is identified as showering (nonshowering) type. However, for a multi-ring event like a $p \to e^+\pi^0$, we don't use the angle probability P_n^{angle} in the particle type determination. That is because a γ from the decay of the π^0 sometimes penetrates in water (mean free path of ~ 55 cm) before causing the electromagnetic shower and this gives a small reconstructed opening angle of the Cherenkov ring. The small opening angle makes $P_n^{\text{angle}}(e)$ small, resulting in small $P_n(e)$. Therefore, for the multi-ring event, we decided to use only the pattern probability $P_n^{\text{pattern}}(e)$ and $P_n^{\text{pattern}}(\mu)$ to determine the particle type. Namely, when $P_n^{\text{pattern}}(e) > P_n^{\text{pattern}}(\mu)$ ($P_n^{\text{pattern}}(e) < P_n^{\text{pattern}}(\mu)$), the n-th ring is identified as showering (nonshowering) type.

A.4 Ring Separation

A.4.1 Ring Separation I

The "ring separation" program separates detected p.e.s in each PMT into contributions from each ring. As a result, this separation gives the observed p.e. distributions for individual rings. We need this separation for the ring fitting and the particle identification of each ring as well as the momentum reconstruction. The strategy of the separation is following. Given the vertex position and ring direction, the expected p.e. distribution for each ring as a function of opening angle θ is calculated according to the observed p.e. distribution assuming an uniform distribution in azimuthal angle ϕ. Using the expected p.e. distribution $q_{i,n}^{\mathrm{exp}}$, where i refers to a PMT number and n refers to a ring number, the observed p.e.s of the i-th PMT (q_i) are separated as

$$q_{i,n} = q_i \times \frac{q_{i,n}^{\mathrm{exp}}}{\sum_{n'} q_{i,n'}^{\mathrm{exp}}} \tag{A-31}$$

where $q_{i,n}$ is fractional p.e.s of the i-th PMT assigned to the n-th ring. With the assumption of the ϕ symmetry, the $q_{i,n}^{\mathrm{exp}}$ can be calculated from $Q_n^{\mathrm{exp}}(\theta_{i,n})$ which is the expected p.e. distribution as a function of opening angle θ. Therefore, calculation of the $Q_n^{\mathrm{exp}}(\theta)$ is essential in the ring separation.

In the first step, all $q_{i,n}^{\mathrm{exp}}$ are set assuming that all particles are electrons. Then, initial expected p.e. distributions are determined by minimizing the following χ^2:

$$\chi_n^2 = \sum_{\theta_{i',n}<70^\circ} \left(\frac{q_{i'} - \sum_{n'} q_{i',n'}^{\mathrm{exp}}}{\sqrt{q_{i'}}} \right)^2 \tag{A-32}$$

The summation is performed for all of i'-th PMT for which the opening angle towards the n-th ring direction $\theta_{i',n}$ is within 70°. Actual procedure is

(a-1) Modify only the first ring, $q_{i,1}^{\mathrm{exp}}$, to minimize the χ_1^2. The optimization is done by changing the momentum of the first ring.

(a-2) Modify only the second ring, $q_{i,2}^{\mathrm{exp}}$, to minimize the χ_2^2. The optimization is done by changing the momentum of the second ring.

⋮

⋮

(a-N) Modify only the N-th ring, $q_{i,N}^{\mathrm{exp}}$, to minimize the χ_N^2. The optimization is done by changing the momentum of the N-th ring.

(b) Go back to (a-1) until all χ_n^2's converge.

After iterating the procedure, we get the initial separated p.e.s $q_{i,n}$ using the converged $q_{i,n}^{\mathrm{exp}}$ and Equation (A-31).

Using the initial separated p.e.s $q_{i,n}$, we make the expected p.e. distribution $Q_n^{\mathrm{exp}}(\theta)$ as a function of opening angle θ towards the n-th ring direction. The $Q_n^{\mathrm{exp}}(\theta)$ is the expected p.e.s projected on hypothetical spherical surface centered at the reconstructed vertex. For making the $Q_n^{\mathrm{exp}}(\theta)$ from the $q_{i,n}$, we need to correct the number of p.e.s for the distance from the vertex, the attenuation length, and the PMT acceptance as

$$q'_{i,n} = q_{i,n} \times \exp(-\frac{R^{\mathrm{sph}}}{L^{\mathrm{abs}}}) \times \frac{1}{\exp(-r_i/L)} \times \frac{1}{f(\Theta_i^{\mathrm{PMT}})} \tag{A-33}$$

where

$q'_{i,n}$	projected p.e.s on the hypothetical sphere
$R^{\rm sph}$	radius of the hypothetical sphere, 16.9 m
$L^{\rm abs}$	absorption length parameter for Monte Carlo simulation, 55 m
L	attenuation length for the event sample (see section 3.3.5)
r_i	distance between the vertex and the i-th PMT
$f(\Theta_i^{\rm PMT})$	effective cross section of a PMT as a function of the incident angle $\Theta^{\rm PMT}$ (Figure 6–9)

By summing up the corrected p.e. $q'_{i,n}$ for the n-th ring within each opening angle bin, we get the $Q_n^{\rm exp}(\theta)$. Here, an optimization is done so that main contribution to the $Q_n^{\rm exp}(\theta)$ comes from non-overlapping region of the ring. Proper normalization and smoothing are also done for the $Q_n^{\rm exp}(\theta)$.

In the next step, we iteratively optimize the $Q_n^{\rm exp}(\theta)$ using the likelihood function. The expected p.e.s for the i-th PMT $q_{i,n}^{\rm exp}$ are recalculated from the $Q_n^{\rm exp}(\theta_{i,n})$ by the function which corresponds to the inverse function of Equation (A-33).

$$q_{i,n}^{\rm exp} = Q_n^{\rm exp}(\theta_{i,n}) \times \exp(\frac{R^{\rm sph}}{L^{\rm abs}}) \times \frac{1}{\exp(r_i/L)} \times f(\Theta_i^{\rm PMT}) \tag{A-34}$$

Using the new $q_{i,n}^{\rm exp}$, separation of the observed p.e.s is performed again by maximizing the following likelihood function L_n:

$$L_n = \sum_{\theta_{i',n}<70^\circ} \log\left(prob(q_{i'}, \sum_{n'} \alpha_{n'} \cdot q_{i',n'}^{\rm exp}) \right) \times \sqrt{Q_n^{\rm exp}(\theta_{i',n})} \times \min[1, \sqrt{\theta_n^c/\theta_{i',n}}] \tag{A-35}$$

where $\alpha_{n'}$ is a normalization parameter used for the optimization, θ_n^c is the reconstructed opening angle of the n-th Cherenkov ring, and the $prob(q_{i'}, \sum_{n'} \alpha_{n'} \cdot q_{i',n'}^{\rm exp})$ is the probability of observing $q_{i'}$ with expected p.e.s of $\sum_{n'} \alpha_{n'} \cdot q_{i',n'}^{\rm exp}$ and defined as

$$prob(q_{\rm obs}, q_{\rm exp}) = \begin{cases} \dfrac{1}{\sqrt{2\pi}\sigma} \exp\left(-\dfrac{(q_{\rm obs} - q_{\rm exp})^2}{2\sigma^2} \right), & \text{for } q_{\rm exp} > 20 \text{ p.e.} \\ \text{convolution of one p.e. distribution and a Poisson distribution (Figure A–9),} & \text{for } q_{\rm exp} < 20 \text{ p.e.} \end{cases} \tag{A-36}$$

where the σ is defined as $\sigma^2 = (1.2 \times \sqrt{q_{\rm exp}})^2 + (0.1 \times q_{\rm exp})^2$ in which the factor 1.2 takes into account the difference of the actual PMT resolution from the ideal one and the factor 0.1 corresponds to the uncertainty of the gain calibration. The probability function for $q_{\rm obs} < 20$ p.e. is calculated by convolution of the measured one p.e. distribution (Figure 3–7) and a Poisson distribution, and is shown in Figure A–9. The factor $\sqrt{Q_n^{\rm exp}(\theta_{i',n})}$ and

$\min[1, \sqrt{\theta_n^c/\theta_{i',n}}]$ in the Equation (A-35) enhance the contributions from PMTs around the Cherenkov edge and inside of the Cherenkov edge, respectively. By optimizing the factor α_n, the program looks for the best α_n which maximize the likelihood function L_n. At first, α_1 is optimized so that L_1 takes maximum. Same optimization is iteratively performed for the second ring, third ring, and so on until all α_n's converge.

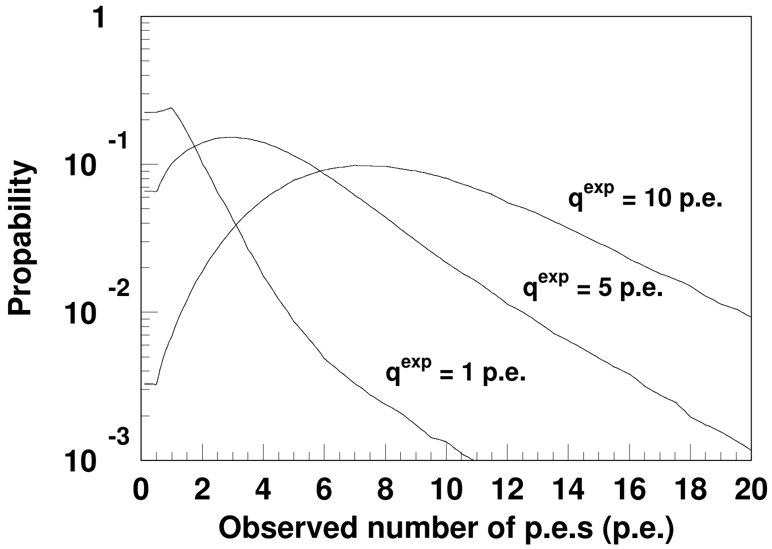

Figure A–9: The probability function for $q_{\text{exp}} < 20$ p.e..

Given the best α_n's, the observed p.e.s of the i-th PMT are separated again as

$$q_{i,n} = q_i \times \frac{\alpha_n \cdot q_{i,n}^{\text{exp}}}{\sum\limits_{n'} \alpha_{n'} \cdot q_{i,n'}^{\text{exp}}} \tag{A-37}$$

Finally, the procedure from Equation (A-33) to Equation (A-37) is repeated two more times (three times in total), to improve the separated p.e.s $q_{\text{i,n}}$. Here, the diffusion of Cherenkov light caused by electromagnetic shower is considered by adding the factor $(R^{\text{sph}}/r_i)^{-1.5}$ and $(R^{\text{sph}}/r_i)^{1.5}$ in Equation (A-33) and (A-34), respectively. In the third cycle, the finite size of the PMT is more carefully taken into account in the same equations. An example of the result of the ring separation is shown in Figure A–10 and A–11. In the figures, observed p.e.s in a three ring event of $p \to e^+\pi^0$ are separated and assigned to each ring. We can see the clearly three separated rings.

A.4.2 Ring Separation II

In the previous section, the "ring separation" algorithm is described. This algorithm, which doesn't assume the particle type, is used for the ring fitting (section 6.2 and appendix A.2) and the particle identification (section 6.3 and appendix A.3). However, for momentum

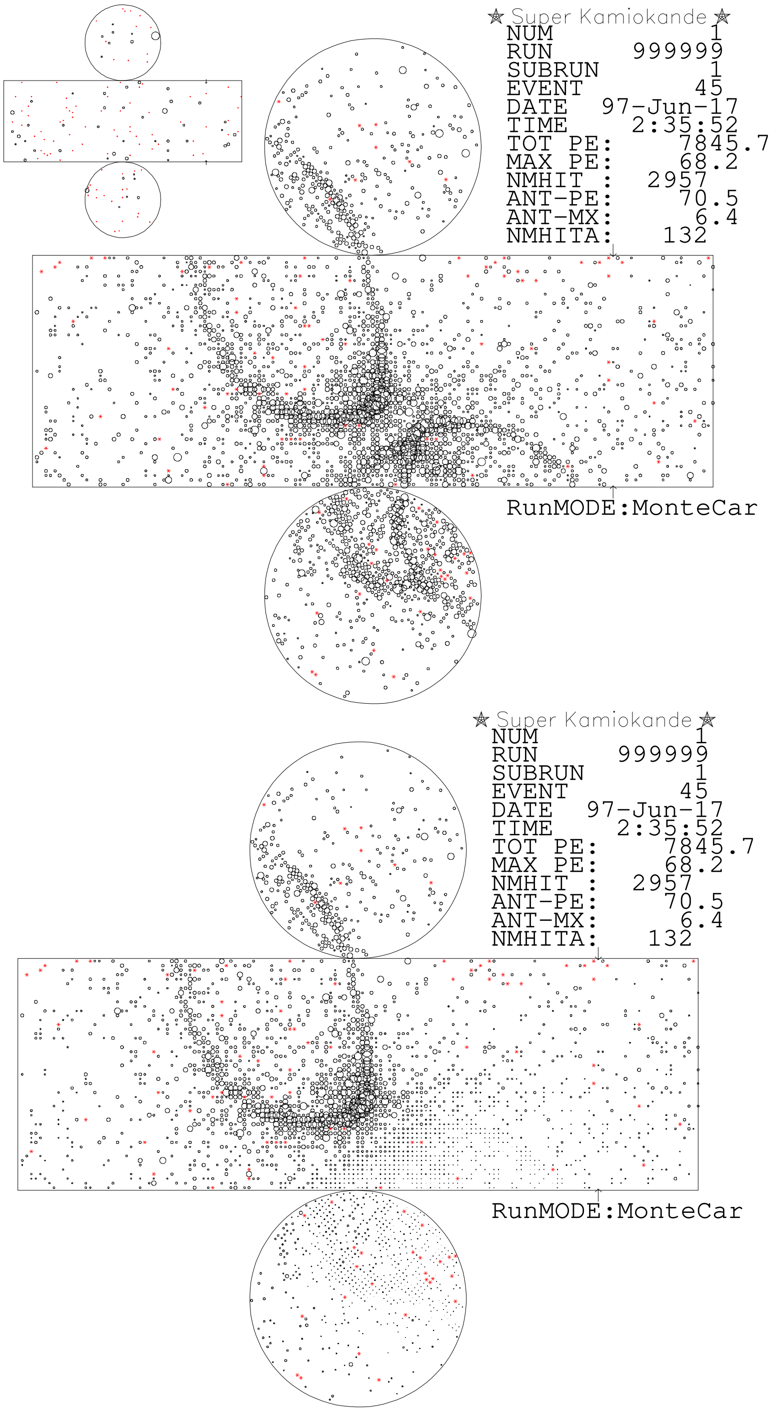

Figure A–10: An example of the result of the ring separation (I). The upper figure shows a $p \to e^+\pi^0$ Monte Carlo event in which three Cherenkov rings are clearly seen. The observed p.e.s in each PMT are separated by "ring separation". The separated p.e.s for each ring are shown in the lower figure and two figures in Figure A–11. The observed p.e.s are clearly separated and assigned to the three rings.

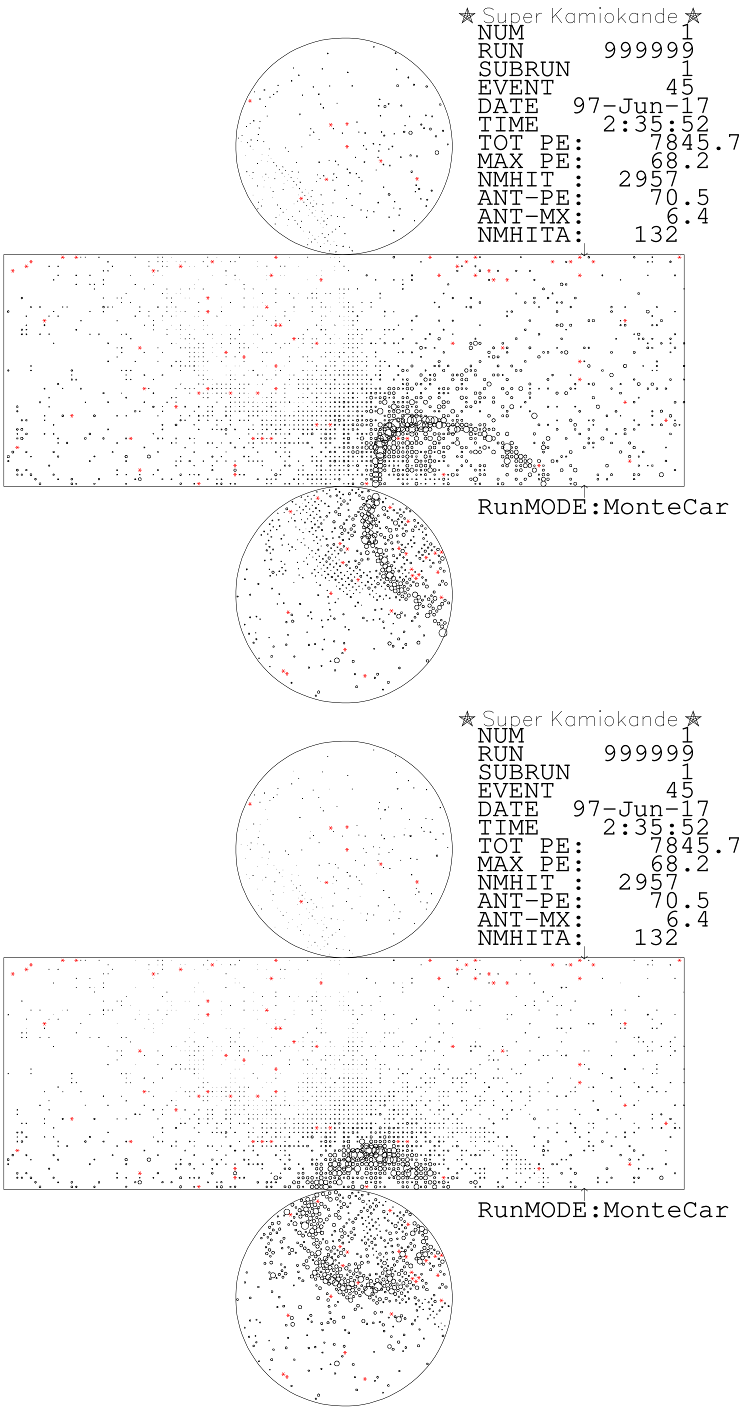

Figure A–11: An example of the result of the ring separation (II). The fractional p.e.s assigned to the second ring and the third ring are shown in the upper figure and lower figure, respectively. See also the Figure A–10 and its caption.

determination, we use the ring separation algorithm assuming the particle type which is determined by the particle identification program. Assuming the particle type of electrons or muons and roughly estimated ring momentum, the expected p.e.s ($\alpha_n \cdot q_{i,n}^{\text{exp}}$) are calculated for each PMT (suffix i) and each ring (suffix n). This expectation is calculated from the tabulated p.e. distribution obtained from Monte Carlo simulation. Scattered light and reflected light on the detector wall are taken into account in the calculation. Using the expectation, ring separation is performed again using the likelihood function similar to Equation (A-35):

$$L_n = \sum_{\theta_{i',n}<70^\circ} \log\left(prob(q_{i'}, \sum_{n'} \alpha_{n'} \cdot q_{i',n'}^{\text{exp}})\right) \tag{A-38}$$

Using the likelihood, α_n's are optimized and then, separated p.e.s are obtained from Equation (A-37). These separated p.e.s $q_{i,n}$ are used for the momentum reconstruction (section 6.5).

A.5 Decay Electron Finding

A.5.1 Detection Method

We identify decay electrons following the primary events to reject atmospheric neutrino background but accept proton decay signal. The energy spectrum of decay electrons are shown in Figure 7–8 and the mean energy is 37 MeV. Since the trigger threshold corresponds to 5.7 MeV electrons, most of decay electrons can be detected. There are experimentally three types of observed decay electrons.

(1) sub-event type ($\Delta t \gtrsim 0.9\mu$ sec)	Decay electrons observed as a separate event (sub-event) as is shown in Figure A–12.
(2) primary-event type ($\Delta t \lesssim 0.9\mu$ sec)	Decay electrons observed in the primary event as is shown in Figure A–13.
(3) split type ($\Delta t \sim 0.9\mu$ sec)	Decay electrons occurring around the boarder timing of event window. Fired PMTs are observed partially in the primary event and partially in the separate event (sub-event).

Here, Δt is the time difference between primary events and following decay electrons.

For sub-event type decays, we require that

(a) $\Delta t < 30\mu$sec

(b) NHIT > 50
NHIT is the number of hit PMTs

(c) the vertex position is well fitted

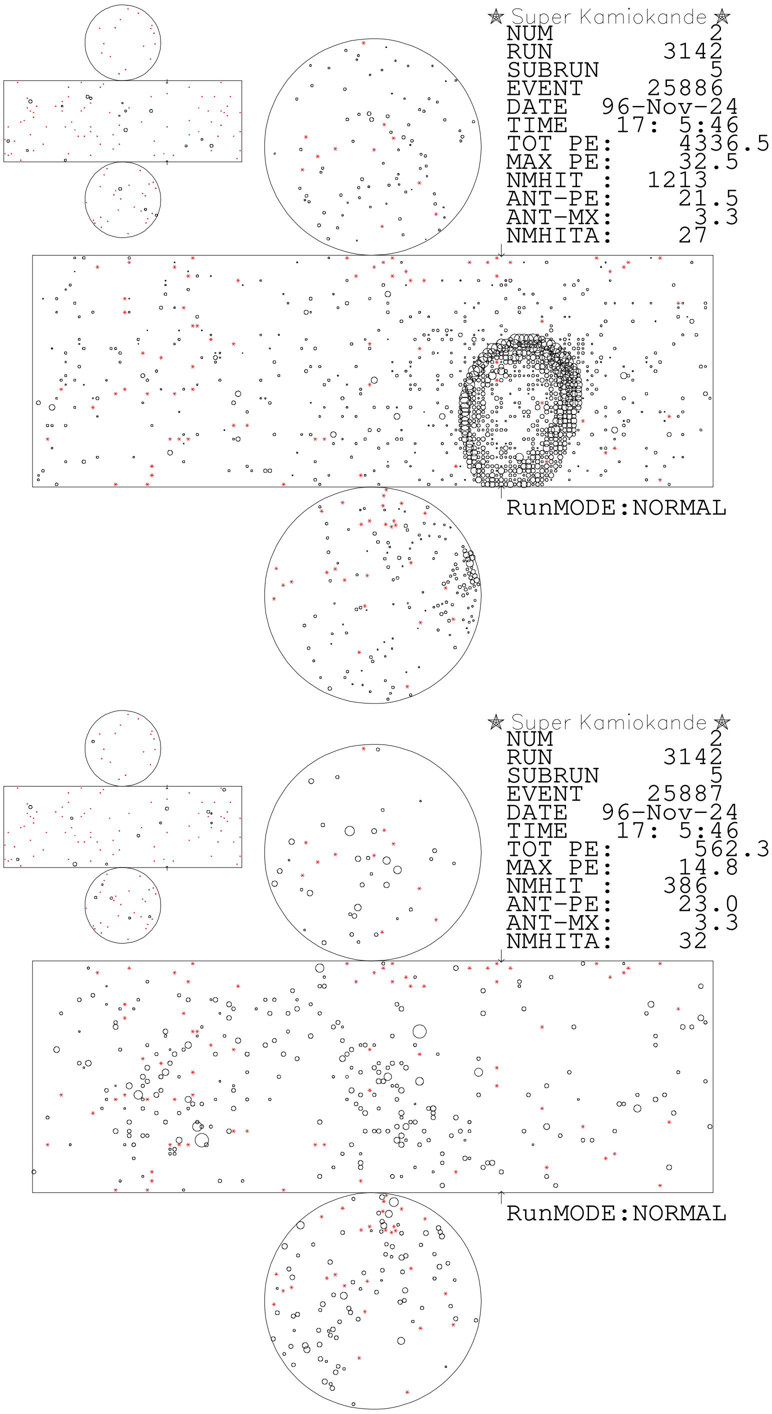

Figure A–12: An example of a sub-event type decay electron. Upper figure shows the primary contained event and lower one shows the following decay electron observed as a separate event. The time difference between two events is 3.2 μsec.

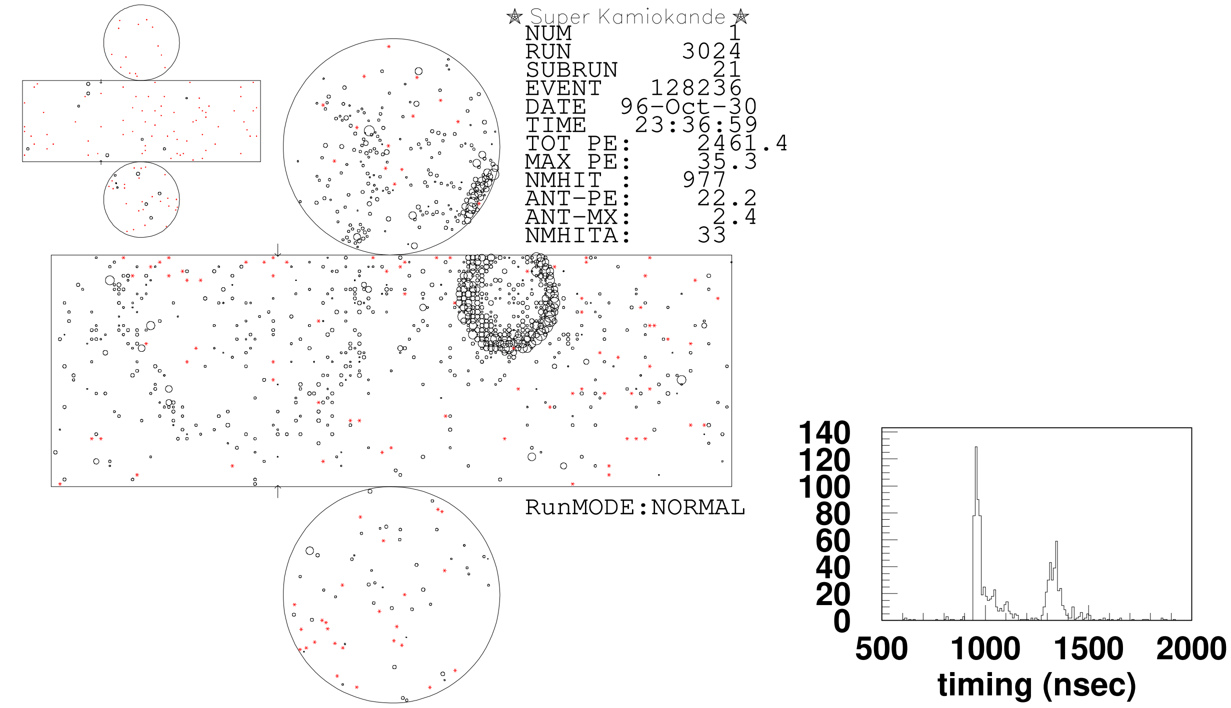

Figure A–13: An example of a primary-event type decay electron. Left figure shows that the primary contained ring (right Cherenkov ring) and the following decay electron (left larger ring) are observed in the same event. Right figure shows the timing distribution of the event in which second peak caused by the decay electron follows the primary peak.

(d) NHIT(50ns) $>$ 30 hit
NHIT(50ns) is the maximum number of hit PMTs in 50 nsec timing window after subtracting TOF.

(e) total number of p.e.s $<$ 2000

For primary-event type decays, other peak of fired PMTs is looked for after the peak of the primary event. We require more than 20 hits in 30 nsec window above the background level.

If one primary event has both primary-event type and sub-event type decays and the time difference between these two decays is less than 100 nsec, they are treated as single split type decay.

To study the background contamination for muon decay detection, we collect about 32000 cosmic ray stopping muons with total p.e.s below 10000 p.e. ($\sim$ 1.5 GeV/c). No event has more than one decay and therefore the contamination level is less than 10^{-4}.

A.5.2 Selection Criteria and Detection Efficiency

For the proton decay analysis, we require additional conditions for muon decays.

(A) NHIT(50ns) $>$ 60 (for sub-event type)

(B) NHIT(30ns) $>$ 40 (for primary-event type and split type)

(C) $0.1\mu\text{sec} < \Delta t < 0.8\mu\text{sec}$ or $1.2\mu\text{sec} < \Delta t < 30\mu\text{sec}$

The criterion (A) corresponds to about 11 MeV electron energy. The criteria (A) and (B) reject the gamma emission from μ^- captured on ^{16}O nuclei. Criterion (C) rejects the decays in the inefficient region around 1 μsec.

References

[1] G. 't Hooft, Phys. Rev. Lett. **37**, 8 (1976).

[2] A. D. Sakharov, Zh. Eksp. Teor. Fiz. Pis'ma **5**, 32 (1967) (JETP Lett. **5**, 24 (1967)).

[3] Jogesh C. Pati and Abdus Salam, Phys. Rev. Lett. **31**, 661 (1973).

[4] H. Georgi and S. L. Glashow, Phys. Rev. Lett. **32**, 438 (1974).

[5] P. Langacker, Phys. Rep. **72**, 185 (1981).

[6] G. G. Ross, *Grand Unified Theories* (ADDISON WESLEY, California, 1985).

[7] C. McGrew *et al.*, Phys. Rev. D **59**, 052004 (1999).

[8] T. J. Haines *et al.*, Phys. Rev. Lett. **57**, 1986 (1986).

[9] R. Becker-Szendy *et al.*, Phys. Rev. **D42**, 2974 (1990).

[10] K. S. Hirata *et al.*, Phys. Lett. **B220**, 308 (1989).

[11] C. Berger *et al.*, Z. Phys. **C50**, 385 (1991).

[12] C. Berger *et al.*, Nucl. Phys. **B313**, 509 (1989).

[13] J. Ellis *et al.*, Phys. Lett. **B252**, 53 (1990); J. Ellis *et al.*, Phys. Lett. **B371**, 65 (1996).

[14] N. T. Shaban and W. J. Stirling, Phys. Lett. **B291**, 281 (1992).

[15] D. Lee, R. N. Mohapatra, M. K. Parida and M. Rani, Phys. Rev. **D51**, 229, (1995)

[16] F. J. Hasert *et al.*, Phys. Lett. **B46**, 121 (1973); F. J. Hasert *et al.*, Phys. Lett. **B46**, 138 (1973).

[17] UA1 Collaboration:G. Arnison *et al.*, Phys. Lett. **B122**, 103 (1983); UA1 Collaboration:G. Arnison *et al.*, Phys. Lett. **B126**, 398 (1983); UA1 Collaboration:G. Arnison *et al.*, Phys. Lett. **B129**, 273 (1983); UA2 Collaboration:P. Bagnaia *et al.*, Phys. Lett. **B129**, 130 (1983).

[18] F. Abe *et al.*, Phys. Rev. **D50**, 2966 (1994); F. Abe *et al.*, Phys. Rev. Lett. **73**, 225 (1994).

[19] P. Langacker, *Ninth Workshop on Grand Unification*, Singapore, (1988).

[20] Particle Data Group, Phys. Rev. **D54**, 85 (1996).

[21] P. Langacker *et al.*, Phys. Rev. **D44**, 817 (1991).

[22] U. Amaldi *et al.*, Phys. Lett. **B260**, 447 (1991).

[23] D. Chang *et al.*, Phys. Rev. **D31**, 1718 (1985); J. Gipson *et al.*, Phys. Rev. **D31**, 1705 (1985).

[24] F. Buccella *et al.*, Phys. Lett. **B233**, 178 (1989); J. Gipson *et al.*, Phys. Rev. **D31**, 1705 (1985).

[25] T. Yanagida, *Proc. of the Workshop on the Unified Theory and Baryon Number in the Universe,* KEK report **79-18**, 95 (1979).

[26] The first uncertainty in the prediction arises from the proton decay matrix element evaluation, whereas the second and the third ones come from LEP data and threshold correction, respectively [15].

[27] J. Wess and B. Zumino, Phys. Lett. **B49**, 52 (1974); J. Iliopoulos and B. Zumino, Nucl. Phys. **B76**, 310 (1974); S. Ferrara and O. Piguet, Nucl. Phys. **B93**, 261 (1975); A. A. Slavnov, Nucl. Phys. **B97**, 155 (1975).

[28] J. Hisano *et al.*, Nucl. Phys. **B402**, 46 (1993).

[29] Paul Langacker and Nir Polonsky, Phys. Rev. **D47**, 4028 (1993).

[30] Pran Nath and R. Arnowitt, Phys. Atom. Nucl. **61**, 975 (1998).

[31] Y.Hayato *et al.*, Phys. Rev. Lett. **83**, 1529 (1999).

[32] I. Frank and I. Tamm, C. R. Acad. Sci. USSR 14, 109 (1937)

[33] A. Suzuki *et al.*, Nucl. Inst. and Meth. **A329**, 299 (1993).

[34] H. Ikeda *et al.*, Nucl. Inst. Meth. **A320**, 310 (1992).

[35] T.Tanimori *et al.*, IEEE Trans. Nucl. Sci. **NS-36**, 497 (1989).

[36] R. Claus *et al.*, Nucl. Inst. and Meth. **A261**, 540 (1987).

[37] KEK Data Acquisition Development Working Group, KEK Report 85-10, (1985).

[38] K. Nakamura *et al.*, Nucl. Phys. **A268**, 381 (1976).

[39] E. Oset *et al.*, Nucl. Phys. **A484**, 557 (1988).

[40] M. Nakahata *et al.*, J. Phys. Soc. Jpn. **55**, 3786 (1986).

[41] C. H. Q. Ingram *et al.*, Phys. Rev. **C27**, 1578 (1983).

[42] D. Ashery *et al.*, Phys. Rev. **C23**, 2173 (1981). T. Fujii *et al.*, Nucl. Phys. **B120**, 395 (1977).

[43] M. Honda *et al.*, Phys. Rev. **D52**, 4985 (1995).; M. Honda *et al.*, Phys. Lett. **B248**, 193 (1990).

[44] E. S. Seo *et al.*, *Proc. of the Twenty Second International Cosmic Ray Conference*, Dublin, Ireland, 1991, edited by M. Cawley *et al.* (Reprint Ltd., Dublin, Ireland, 1991), Vol. 2, p.627.

[45] T. K. Gaisser, T. Stanev, and G. Barr, Phys. Rev. **D38**, 85 (1988).; G. Barr, T. K. Gaisser, and T. Stanev, Phys. Rev. **D39**, 3532 (1989).

[46] E. V. Bugaev and V. A. Naumov, Phys. Lett. **B232**, 391 (1989).

[47] H. Lee and Y. Koh, Nuovo Cimento **B105**, 884 (1990).

[48] H. J. Grabosch *et al.*, Z. Phys. **C41**, 527 (1989).

[49] S. J. Barish *et al.*, Phys. Rev. **D16**, 3103 (1977).

[50] S. Bonetti *et al.*, Nuovo Cimento **A38**, 260 (1977).

[51] S. V. Belikov *et al.*, Z. Phys. **A320**, 625 (1985).

[52] N. Armenise *et al.*, Nucl. Phys. **B152**, 365 (1979).

[53] K. Abe *et al.*, Phys. Rev. Lett. **56**, 1107 (1986).; C. H. Albright *et al.*, Phys. Rev. **D14**, 1780 (1976).

[54] D. Rein and L. M. Sehgal, Ann. of Phys. **133**, 79 (1981).; D. Rein, Z. Phys. **C35**, 43 (1987).

[55] G. M. Radecky *et al.*, Phys. Rev. **D25**, 1161 (1982)

[56] *Proc. of the Int. Symp. on Lepton and Photon,* 1979

[57] T. Kitagaki *et al.*, Phys. Rev. **D34**, 2554 (1986).

[58] E. Oltman *et al.*, Z. Phys. **C53**, 51 (1992).

[59] S. J. Barish *et al.*, Phys. Rev. **D17**, 1 (1978).

[60] H. Sarikko, *Proc. of the NEUTRINO '79*, 507 (1979).

[61] S. Barlag *et al.*, Z. Phys. **C11**, 283 (1982).

[62] Paul Musset and Jean-Pierre Vialle, Phys. Rep. **C39**, 1 (1978).; J. E. Kim *et al*, Rev. Mod. Phys. **53**, 211 (1981).

[63] C. Bltay *et al.*, Phys. Rev. Lett. **44**, 916 (1980).

[64] N. I. Bker *et al.*, Phys. Rev. **D25**, 617 (1982).

[65] S. Ciampolillo *et al.*, Phys. Lett. **B84**, 281 (1979).

[66] J. G. Morfin *et al.*, Phys. Lett. **B104**, 235 (1981).

[67] D. S. Baranov *et al.*, Phys. Lett. **B81**, 255 (1979).

[68] A. S. Vovenko *et al.*, Yad. Fiz. **30**, 1014 (1979).

[69] V. N. Anikeev *et al.*, Z. Phys. **C70**, 39 (1996).

[70] D. C. Colley *et al.*, Z. Phys. **C2**, 187 (1979).

[71] S. J. Barish *et al.*, Phys. Rev. **D19**, 2521 (1979).

[72] O. Erriquez *et al.*, Phys. Lett. **B80**, 309 (1979).

[73] D. Rein and L. M. Sehgal, Nucl. Phys. **B223**, 29 (1983).; P. Marage *et al.*, Z. Phys. **C31**, 191 (1986).

[74] CERN Program Library W5013 (1994).

[75] T. A. Gabriel *et al.*, IEEE Trans. Nucl. Sci. **36**, 14 (1989).

[76] E. Bracci *et al.*, CERN/HERA 72-1, (1972).; A. S. Carrol *et al.*, Phys. Rev. **C14**, 635 (1976).; E. Eichler, JADE-Note 65, (1980).

[77] Davies and E. Roy, *Machine vision: theory, algorithms, practicalities* (Academic Press, San Diego, 1997).

[78] S. Kasuga *et al.*, Phys. Lett. **B374**, 238 (1996).

[79] P. Hanggi *et al.*, Phys. Lett. **B51**, 119 (1974).

[80] M. Yamada *et al.*, Phys. Rev. **D44**, 617 (1991).

[81] M. Nakahata *et al.*, Nucl. Inst. and Meth. **A421**, 113 (1999).

[82] C. McGrew, PhD thesis, University of California Irvine (1994).; private communication with B. Viren.

[83] A. Nishimura and K. Takahashi, J. Phys. Soc. Jap. **52**, 54 (1983).

[84] T.J. Loredo, in *Maximum Entropy and Bayesian Methods*, edited by P.F. Foug 'ere (Kluwer Academic, Dordrecht, The Netherlands, 1990).

[85] B. Viren, Super–Kamiokande Report No. 98-3, 1998, (unpublished but available from http://www-sk.icrr.u-tokyo.ac.jp/doc/sk/pub).

[86] R.M. Barnett *et al.* Phys. Rev. **D54**, 1 (1996).